Εθνικό Μετσόβιο Πολυτεχνείο
Σχολή Πολιτικών Μηχανικών
Τομέας Γεωτεχνικής

National Technical University of Athens
School of Civil Engineering
Geotechnical Department

Διπλωματική Εργασία της

ΚΑΡΑΓΕΩΡΓΟΥ-ΜΗΤΣΑΚΟΥ ΑΝΘΟΥΛΑΣ

Επιβλέπων

Νίκος Γερόλυμος

ΦΑΙΝΟΜΕΝΟΛΟΓΙΚΑ ΚΑΤΑΣΤΑΤΙΚΑ ΠΡΟΣΟΜΟΙΩΜΑΤΑ ΓΙΑ ΣΤΟΙΧΕΙΑ ΩΠΛΙΣΜΕΝΟΥ ΣΚΥΡΟΔΕΜΑΤΟΣ: ΕΦΑΡΜΟΓΗ ΣΕ ΠΑΣΣΑΛΟΥΣ

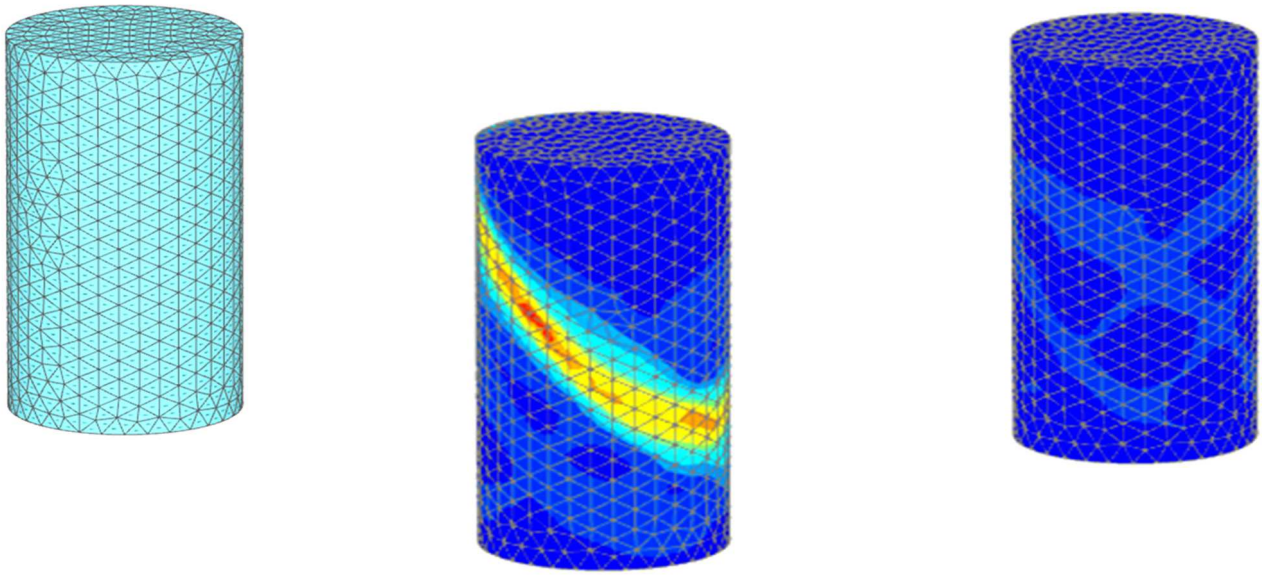

PHENOMENOLOGICAL CONSTITUTIVE MODELS FOR REINFORCED CONCRETE ELEMENTS: APPLICATION TO PILES

Diploma Thesis by

KARAGEORGOU-MITSAKOU ANTHOULA

Supervised by

Nikos Gerolymos

Αθήνα Νοέμβριος 2020

Preface

In this preface I would like to express my gratitude to all the people that have assisted me to complete this diploma thesis, that finalizes my studies in Civil Engineering at National Technical University of Athens.

Firstly, this thesis would not have been possible without the assistance of my supervisor, Professor Nikos Gerolymos. I would like to express my deepest appreciation and gratitude not only for the inspiration and invaluable knowledge provided, but also for his constant guidance, motivating words and support, as he helped me in critical moments to overcome obstacles that arised throughout this thesis.

Moreover I would like to thank Mr. Haris Lamaris and Efi Triantafilli, with whom I work with, for their support and patience during this challenging period.

Finally, above all, I feel the need to thank my friends and family and especially my parents, for their constant support and encouragement.

Special Acknowledgment

The contribution of Bentley Systems in supporting the educational and research activities of The Soil Mechanics laboratory by providing licenses for PLAXIS 2D and 3D is highly acknowledged by the Supervisor of the Diploma thesis. Special appreciation is given to Prof. Ronald Brinkgreve and to Mr. Erwin Beernink, Senior Director at Bentley Systems, for their invaluable efforts and support.

Abstract

Three phenomenological constitutive models are presented for the response of reinforced concrete elements. The first is a simple uniaxial stress-strain model, based on Mohr-Coulomb failure criterion, developed by Gerolymos et al (2014). This model possesses considerable flexibility to reproduce the macroscopic behavior of reinforced concrete circular sections. The second is a mathematically simple model, also formulated within the framework of classical elastoplasticity. Concrete material is described by Mohr-Coulomb failure criterion and it is combined with elastoplastic reinforcement elements. The third approach is a combination of elastoplastic reinforcement elements and an advanced model for concrete material, that employs Mohr-Coulomb failure criterion for deviatoric loading and Rankine for tension. Due to its formulation it accounts for strain hardening and softening. Nonlinear three-dimensional analysis is used to conduct a thorough investigation on the performance of the aforementioned models utilizing Plaxis 3D Finite Element Software. The models are first calibrated and then compared and validated against results from computer codes. After validation, the proposed models are implemented in pile-soil interaction cases and their performance is evaluated utilizing Broms theory (1964) of ultimate pile lateral capacity. Nonlinear behavior of the soil and the pile is considered, and pile-soil response is investigated through a detailed parametric study.

.

TABLE OF CONTENTS

1 Introduction

1.1 Layout

In chapter 1 the scope of this diploma thesis is presented, followed by the definition of the problem that triggered motivation for this study.

In chapter 2 the relevant theoretical background is given. The fundamentals of concrete material, as well as structural reinforcing steel are presented. Emphasis is given in the nonlinear behavior of concrete. To give more insight in the stress-strain relation, the main parameters affecting the softening behavior of concrete in tension and compression are outlined. Consequently, a brief description of the function of reinforced concrete elements follows, and some empirical methods for the estimation of the plastic hinge length of RC flexural members are outlined. The last part contains a short introduction to the use of pile foundations, focusing on the behavior of laterally loaded piles.

In chapter 3 a brief description of the Finite Element Method is presented, and the basic concepts of constitutive modeling are presented. Subsequently, Plaxis 3D Software utilized in the analysis, is introduced and the three constitutive models used to simulate the behavior of reinforced concrete elements, are described. Lastly, mesh dependency of key parameters is investigated, in order to avoid unobjective results in the analyses.

In chapter 4, a simple pushover analysis of a reinforced concrete circular column with the use of Plaxis 3D code is presented. The setup of 3 different models, in order to investigate the behavior of the RC column, is described. For each setup reinforced concrete material is simulated by the three suggested models. The first is an elastoplastic model based on Mohr-Coulomb failure criterion, simulating concrete material, combined with structural 3D elements for reinforcement. For the second approach, Plaxis Concrete constitutive model is applied. Again structural 3D elements are used for reinforcement. The basic aim is to capture the real behavior of structural reinforced concrete. For this reason calibration of the most affecting parameters is carried out. The third approach is based on the macroscopic Mohr-Coulomb simplified constitutive model proposed by Gerolymos et al (2014). In this approach no detailed reinforcement is required as it simulates in a uniform approach the elastoplastic response of circular reinforced concrete elements. Input parameters are

calibrated according to the results from the second model setup. Consequently results extracted from numerical analyses are compared with each other as well as with two computer codes. These codes are: USC_RC, which is a fiber analysis calculation tool, and Response-2000, used for the analysis of strength and ductility of reinforced concrete structures.

In chapter 5 the previous analyzed phenomenological constitutive models are applied to a volume pile, in order to evaluate their performance in soil structure interaction cases. A single pile subjected to lateral force and consequently to a combination of horizontal and axial force, is studied. Nonlinear behavior of the pile is considered and thorough parametric study is carried out considering full bond conditions between pile and soil, as well as sliding and gapping. Moreover the influence of vertical loads on lateral response is discussed. Results from numerical analyses for the three developed constitutive models are compared and evaluated.

In chapter 6 results derived from this study are discussed. Conclusions are presented regarding the capabilities of each constitutive model to simulate reinforced concrete elements. Lastly recommendations for further research are made.

1.2 Scope of work

The aim of this thesis is the presentation of phenomenological constitutive models for the nonlinear response of reinforced concrete elements. Three different constitutive relations are proposed to simulate reinforced concrete material in numerical analyses, utilizing Plaxis 3D Finite Element code. Key parameters are calibrated and the validity of each model is verified through comparison with results from computer codes based on Fiber analysis and Modified Compression Field Theory. The first approach considers a Mohr-Coulomb model for concrete material, based on the assumption of perfect elastoplasticity. It is combined with detailed reinforcement simulated by structural 3D elements whose behavior is described by von Mises yield criterion. The second approach combines the advanced Plaxis Concrete model with detailed reinforcement. Concrete is an elastoplastic material model that approaches the real behavior of concrete as a quasi-brittle material. It accounts for strain hardening and stiffness reduction due to cracking, while again, the behavior of reinforcement elements is described by von Mises yield criterion. The third model is based on the macroscopic Mohr-coulomb approach, as proposed by Gerolymos et al (2014). It is a

simplified model that combines well known constitutive relations, easy implementation and simple geometry, as no detailed reinforcement needs to be incorporated and reinforced concrete material is described uniformly.

1.3 Problem definition

In order to predict the behavior of reinforced concrete elements, many computational tools have been developed. These programs are mostly designed based on existing models in literature and standards. When it comes to sectional analysis these simple tools predict quite accurately the response of the reinforced concrete section, but when it comes to full member performance, deviations from reality are observed. These deviations are associated with the assumptions used to predict plastic hinge length. There are numerous simplified methods estimating plastic hinge length in literature, but they do not contain all factors affecting plastic hinge formation. As a result not in a few cases in experiments or in reality different failure or failure modes are observed from what expected. In numerical simulations, as they are a powerful tool for nonlinear analyses, the plastic hinge length is calculated more accurately, and more realistic failure mechanisms are obtained. A realistic solution for a structural problem involving concrete depends in large part on the choice of an appropriate constitutive model. In the past decades, intensive studies have led to a better understanding of the behavior of quasi-brittle media. Therefore many models have been developed for the simulation of concrete material in finite element methods. However these ‘exact' constitutive models exist in more sophisticated FE software packages. On account of this, in many cases, simplified stress-strain relations must be adopted, based on well-known failure criteria such as Tresca or Mohr-Coulomb. Furthermore when soil-structure interaction is studied in FEM simulations, the foundation system usually is considered to have an elastic response. However foundation inelasticity in many cases must be considered especially when there is risk of large deflections. For such cases the exact failure mechanism of the reinforced concrete foundation system must be inspected and factors that affect post-yielding deformability to be considered for a safer design.

2 Theoretical Background

2.1 Introduction

Concrete is one of the most widely used construction material. It is a composite material that is produced after the hardening of a mixture consisting of aggregates, cement and water. During the admixture other physical or chemical ingredients can be added to give desirable properties to the concrete material depending on the requirements of the structure. The main characteristic of concrete is its high compressive strength contrary to its limited tensile strength. Due to this fact, in most applications reinforcement is added to undertake the tensile stresses generated by applied loads. Reinforcement components usually are steel bars that can be produced in various diameters or fibers made of steel or polymers. In order to understand the response of reinforced concrete elements under different loading conditions, deep knowledge of the fundamentals of concrete material behavior is required, bringing the stress-strain relation into focus. In the following paragraphs concrete material behavior under compressive and tensile loading is described, as well as the characteristics of structural steel used as reinforcement. Lastly, the basic principles of designing reinforced concrete structures are outlined, followed by the features of plastic hinge length in flexural members.

2.2 Concrete under compression

The compressive strength governs the behavior of concrete as it is the basis to define many other of its properties . The characteristic compressive strength can be determined by executing uniaxial compression tests on cylindrical or prismatic specimens from the maximum load the specimen can receive until it fails. A typical stress strain diagram of normal strength concrete is illustrated in Figure 2.2.1, below.

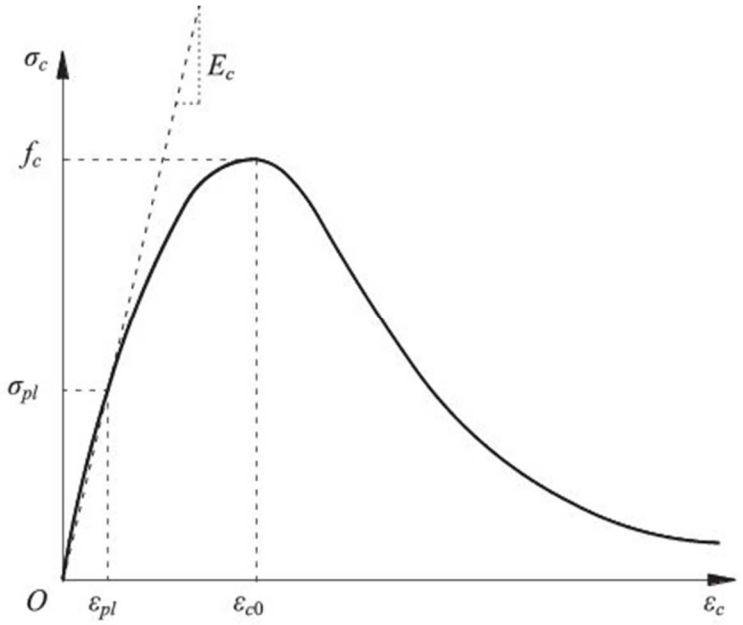

Figure 2.2.1. Stress-strain diagram of normal strength concrete

As shown in the figure, at first the material behaves linear elastically, until it reaches the yield stress (σ_{pl}). In this part of the curve the strains are reversible (elastic strains). When reaching the yield stress plastic strains are generated and the concrete hardens non linearly. At this point the first cracks are generated. These cracks are the result of the flow of the soft cement matrix around the stiffer aggregates due to loading. This movement leads to lateral tension and cracking, and stresses developed in front and behind aggregates create shear cones. As failure proceeds along the sides of these shear cones, the critical crack length is reached. At this point concrete has reached its peak strength the and the material starts to fail. After that moment, strain softening follows as the load that can be carried by concrete decreases with an increase in strain. Stain softening can be observed if the test is strain controlled. At last the sample completely fails due to the excessive crack propagation. The material's strength after failure is called residual strength.

Although rupture of concrete structures is closely related to compressive failure of concrete material in the crashing zone, few studies have been carried out. Researchers mostly concentrated on tensile fracture, due to the ease of cracking observation, as it is a local phenomenon. Compressive failure is much more complex, as many microcracks develop and connect, therefore volumetric observation is needed. For many years compressive stain softening was neglected, whereas research carried out by Van Mier (1984) showed that compressive softening can be analyzed in a similar way to tensile softening. According to Nakamura & Higai (2001) concrete under uniaxial compression has a definite size of fracture zone that depends mostly on maximum aggregate size, distance between aggregates and compressive strength.

2.3 Concrete under tension

Generally, concrete has relatively limited tensile strength which is only 5-10 % of its compressive strength. The tensile strength can in principle be derived directly from uniaxial tension tests, although due to the experimental difficulties of these tests, indirect methods like the 4-point bend beam are currently used. The different response of concrete in tension and compression is depicted in Figure 2.3.1.

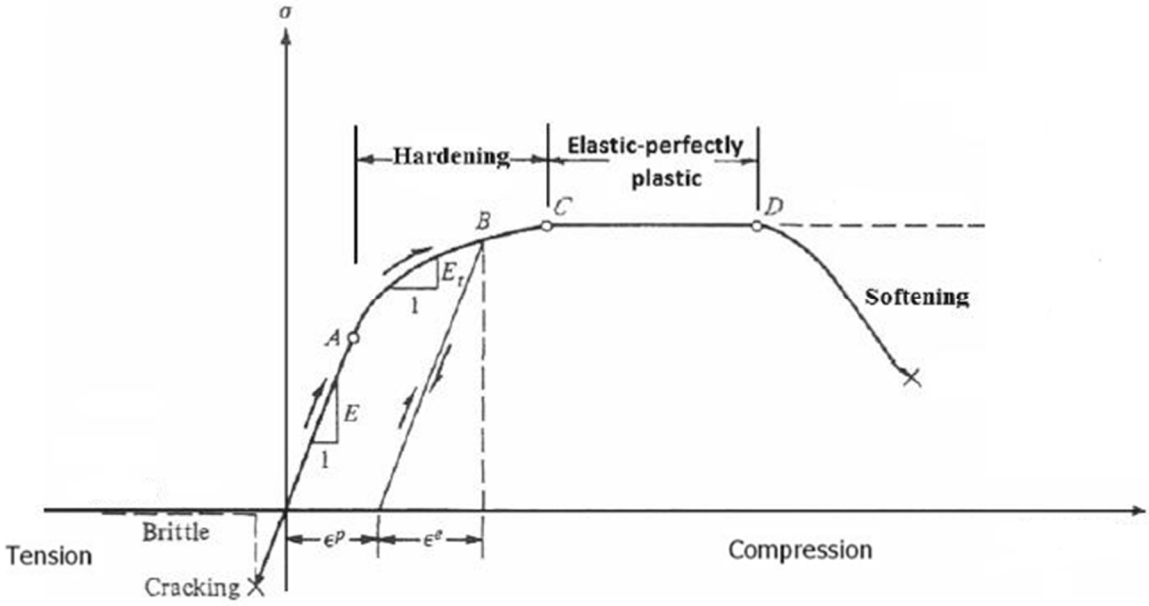

Figure 2.3.1. Uniaxial behavior of concrete (Chen and Han, 1982)

As shown in the diagram above, failure under tensile loading is more brittle and no residual strength is observed. While attention is paid in tensile loading, a more detailed stress - deformation response is illustrated in Figure 2.3.2 below:

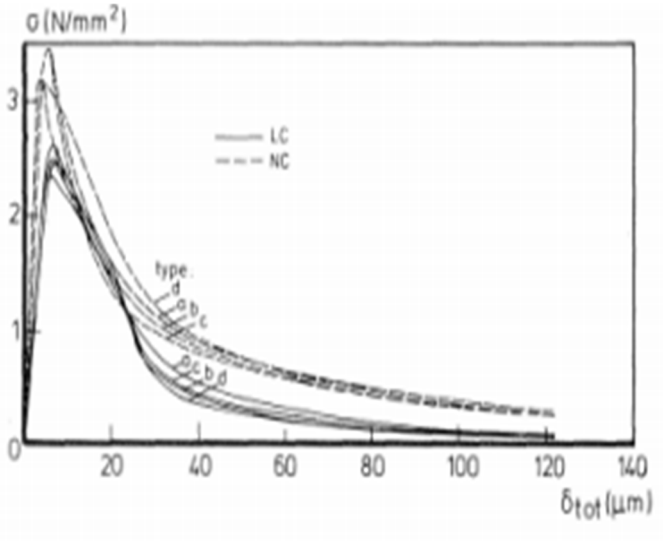

Figure 2.3.2. Stress-deformation results from experiments by Cornelissen et al., (1962)

As one can see, the stress-deformation relationship before reaching the peak tensile strength is linear. This domain describes the un-cracked concrete under tensile loading. When the tensile stress reaches the 90% of the tensile strength cracks start to develop. These cracks grow mostly perpendicular to the loading axis. If these cracks prevent the transfer of forces through the material significant softening takes place. Generally as soon as cracking occurs it is assumed that the material loses its tensile strength.

In this case reinforcement should be able to receive all the tensile forces, before the crack propagates and leads to failure. In principle, the response of concrete under tensile loading is described by a stress strain relation for the linear part before cracking and a stress-crack opening relation for the part till rupture. In this domain tensile stress and crack width are related by the fracture energy G_F.

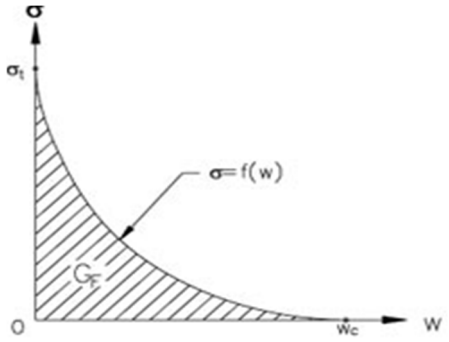

Figure 2.3.3. Softening curve under tensile loading (Bazant and Planas,1998)

2.4 Structural steel reinforcement

The behavior of structural reinforcing steel can be described by stress-strain relations obtained from coupon tests of bars loaded monotonically in tension. It is assumed that reinforcing steel behaves in compression, as in tension, which is a reasonable simplification for reinforced concrete elements. A typical stress-strain curve is visualized in Figure 2.4.1.

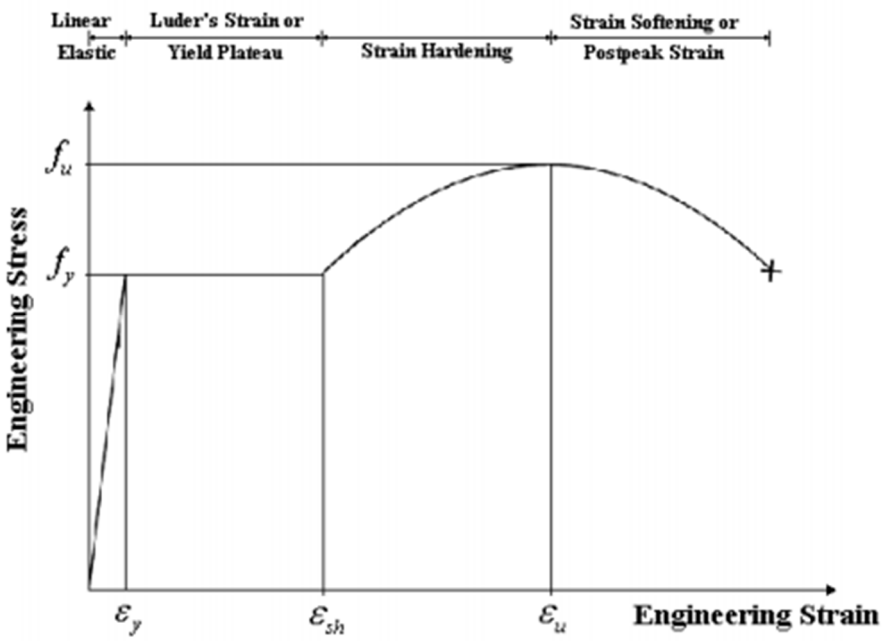

Figure 2.4.1 Experimental stress-strain curve of reinforcing steel

At the initial part of the curve steel behaves linear elastically until the yield stress is reached. After reaching the yield stress, a yield plateau follows and then a strain hardening range in which stress increases with strain. At the last range of the diagram stress drops until fracture occurs. For simplicity and calculation purposes the stress-strain relation of steel reinforcement can be replaced by an idealized diagram (Figure 2.4.2). Two different idealizations are commonly used in literature depending on the desired level of accuracy (ASCE 1982).

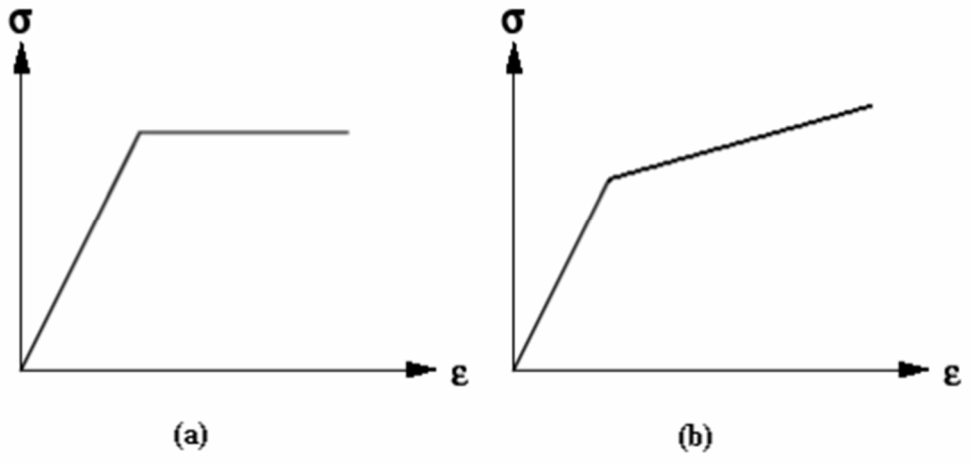

Figure 2.4.2. Simplified stress-strain curves for steel: (a) linear elastic-perfectly plastic response, (b) linear strain hardening after yielding

In the first approach (Figure 2.4.2(a)) the behavior of steel is considered linear-elastic perfectly plastic, as strain hardening after yielding is neglected. In the second idealization (Figure 2.4.2(b)) yielding is followed by linear strain hardening. This approach is preferable when ductility of a member plays a major role, as it is necessary to evaluate the steel stress at strains higher than yield to more accurately assess the strength of members at large deformations, e.g. in seismic design.

For design purposes the following stress-strain diagram can be applied.

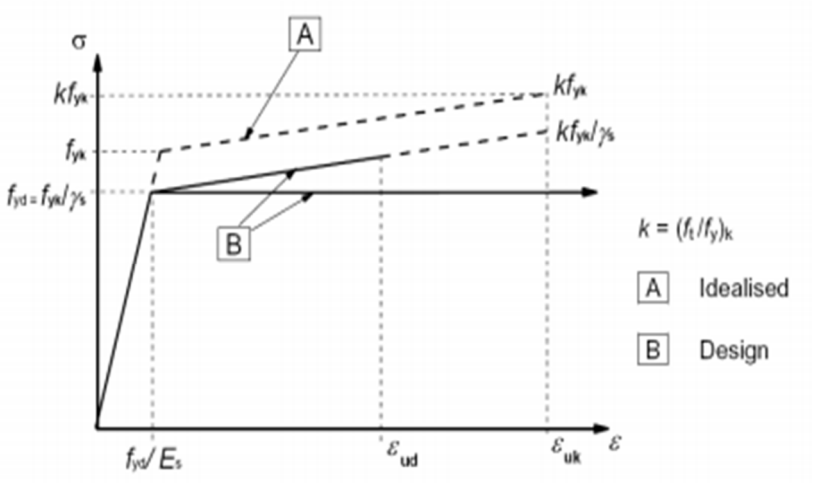

Figure 2.4.3. Stress-strain diagram of steel for design purposes, according to EN 1992-1-1

Branch A is the schematized behavior dependent on characteristic values, while branch B on design values (characteristic values divided by a factor of safety γ_s.). As illustrated, despite the modulus of elasticity E_s and the characteristic yield strength f_{yk}, ductility parameters need to be defined. These are strain at maximum stress, ε_{uk} and the ratio between tensile and yield strength, $f_{tk}\ /f_{yk}$. According to EN-1992 - 1-1 the stiffness of the initial linear part can be assumed to be equal to 200 GPa and the characteristic yield strength to 500 MPa.

2.5 Reinforced concrete elements

Generally all concrete structures are reinforced with some type of reinforcement. Non reinforced concrete members are assumed to carry only small gravity loads or perform a non-life-threatening function. In all other applications concrete has to be reinforced. Adding reinforcement to a structure element subjected to bending (from loads perpendicular to element's axis) increases its strength, due to the fact that failure does not occur at the moment when concrete fails in tension . After cracking due to tensile loading, it is considered that concrete loses its tensile strength. At this point reinforcement has to take up tensile forces, in order to limit the crack and stop propagation. Therefore at least the tensile zone of a structure has to be reinforced. The main objective in the design process of RC elements is yielding of reinforcement to come first of failure of concrete in compression. The overall performance of RC members depends on the response of a small zone called plastic hinge. In this zone plastic deformation occurs after yielding.

2.5.1 Methods of estimating plastic hinge length of RC flexural members

Generally a plastic hinge is the region of a RC element with the most severe damages, due to large plastic deformations. In this area wide cracking, crashing, or spalling of concrete and yielding of longitudinal reinforcement, depending on type of failure, are observed. When it comes to full member response, when the ultimate bending moment and curvature are reached in critical section, the region of plastic curvature is spread over a length of element. The ultimate curvature distribution over the length of the member can be idealized into elastic and plastic region. Plastic region represents the plastic hinge zone.

The behavior of plastic hinges is a very complex matter basically due to the nonlinear behavior of materials. Plastic hinge zone depends on various factors such as the magnitude of axial load, longitudinal reinforcement ratio, level of confinement, yield penetration, shear span ratio, concrete compressive strength and load type (static or dynamic). Only with many assumptions and simplifications it can be calculated analytically. Typically for this region, an equivalent length is estimated, where plastic curvature is assumed to be constant or to have a linear distribution. Indicatively some different methods for curvature distribution in the plastic hinge zone are depicted in Figure 2.5.1. For Priestley & Park plastic hinge length depends on column height, longitudinal steel yield strength and rebar diameter. Curvature distribution is considered to be uniform along the plastic hinge length and the effect of axial force is neglected. According to Rohleder (2017), for Esmaeily's first method (2002) a linear distribution of curvature along plastic hinge length is considered, taking into account the effect of axial force, followed by Esmaeily's second method (2002) that divides the transition zone in two parts one of linear increased curvature distribution and one of constant. The length of constant curvature is considered equal to the section depth for columns with height to depth ratio of less than 12.5 or otherwise, equal to 0.08×L, where L is the column height. Curvature distribution along the second part is assumed to be linear and its length depends on axial and lateral loading (Rohleder, 2017).

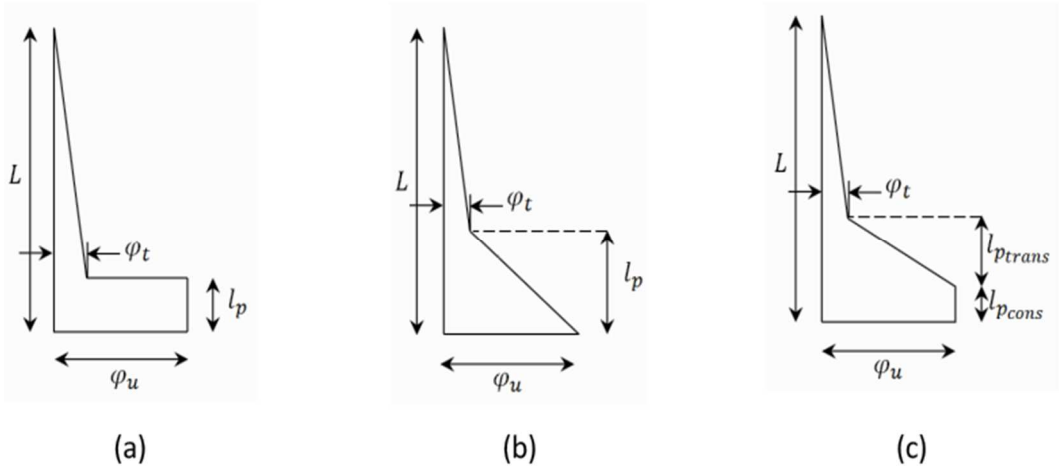

Figure 2.5.1. Curvature distribution along column height according to (a) Priestley & Park, (b) Esmaeily's first method and (c) Esmaeily's second method by Rohleder (2017)

However the physical plastic hinge length may be quite deferent. Due to the uncertainties involved in the determination of plastic hinge length, Finite Element Method is becoming more and more popular to obtain nonlinear structural response. Three regions develop in the plastic hinge zone, which are:

- Rebar yielding zone
- Concrete crashing zone
- Curvature localization zone

Some of the many empirical equations that have been proposed for the prediction of the equivalent plastic hinge length, are outlined in Table 2.1 below:

Table 2.1: Proposed expressions of estimating plastic hinge length

Priestley and Park (1987)	$L_\rho = 0.08L_v + 6d_{bl}$ (for RC columns)
Paulay and Priestley (1992)	$L_P = 0.08L_v + 0.022d_{bl}\ f_y$ (for RC beams and columns)
Coleman and Spacone (2001)	$G_f^c / \lfloor 0.6f_c(\varepsilon_{20} - \varepsilon_c + f_c/E_c)\rfloor$
Panagiotakos and Fardis (2001)	$0.18z + 0.021A_s d_b f_y$
Bae and Bayrak (2008)	$L_p / h = \left[0.3p / p_0 + 3A_s / A_g - 0.1\right](z/h) + 0.25 \geq 0.25$

where:

A_g: gross area of concrete section,

A_s: area of tension reinforcement,

d_b: diameter of longitundinal reinforcement,

E_S: Young modulus of concrete,

f_c: concrete compressive strength,

f_y: yield strength of reinforcement,

G_f^c : concrete compressive fracture energy,

h: height of the member,

Po: 0,85 $f_c\left(A_{g-}A_s\right) + f_y A_s$,

z: distance from critical section to point of contraflexure,

ε_c : peak compressive strain,

ε_{20} : strain at 20% of the compressive strength

2.6 Pile foundations

Piling is the most common method of deep foundation. Piles are usually columnar slender elements that transfer loads from the superstructure through weak compressible soils onto stiffer soils or rock formations (Tomlinson, 1994). They can be subjected to compressive, uplift or lateral loads, as well as to combined vertical and horizontal loads when are used in retaining structures or bridge piers. Piles are distinguished from other foundation types due to their higher slenderness ratio. Figure 2.6.1 presents a rough categorization of foundation types.

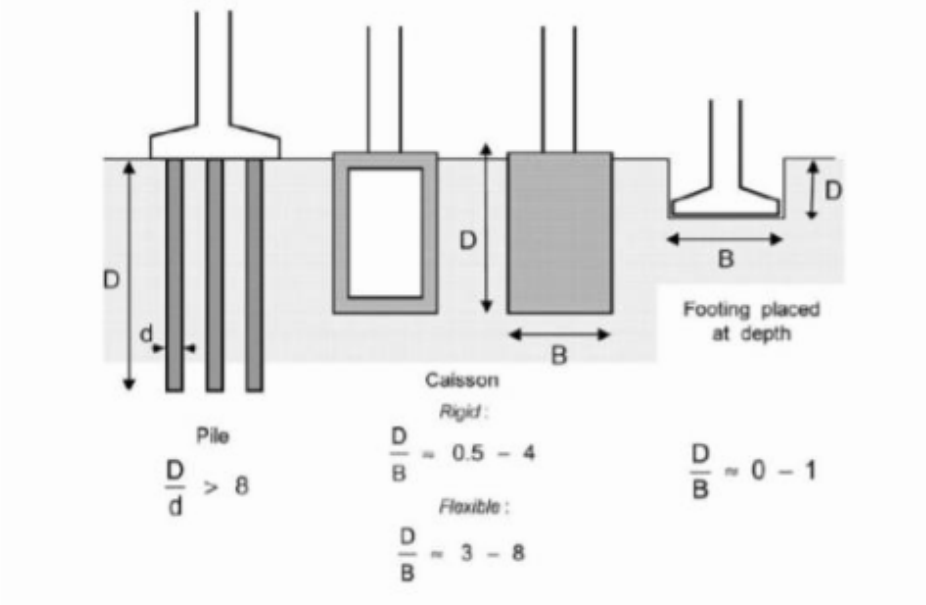

Figure 2.6.1. Different foundation types that are used in structural systems (Gerolymos & Gazetas, 2006)

The first piles were made of timber. Due to its strength combined with lightness and ease of cutting and handling, it remained the only material used for piling for centuries. Timber was gradually replaced by concrete and steel because of the significantly increased compressive, bending and tensile capacity that these materials provided compared to timber. Reinforced concrete which was developed in the late nineteenth and early twentieth century, largely replaced timber. At first mostly precast concrete piles were used. However with the improvement of drilling machines precast driven piles were partially replaced by numerous forms of cast in situ piles. Nowadays, highly efficient machines for drilling pile boreholes

of large diameters and great depth have been developed, capable to drill stiff soils or soft rock formations. The estimation of the load carrying capacity of piles is a complex matter, based on theoretical concepts from sciences of rock and soil mechanics and on empirical experience. The basis of pile bearing capacity is that the total resistance of the pile to compression loads is the sum of two components, namely skin friction and tip resistance. If skin friction is the main parameter that resists loads from the superstructure the pile is called friction pile, and if on the other hand resistance is obtained from the stiff bearing layer the pile is called end-bearing pile, as illustrated in Figure 2.6.2. Most piles use some end bearing and some friction, in order to resist the action of loads.

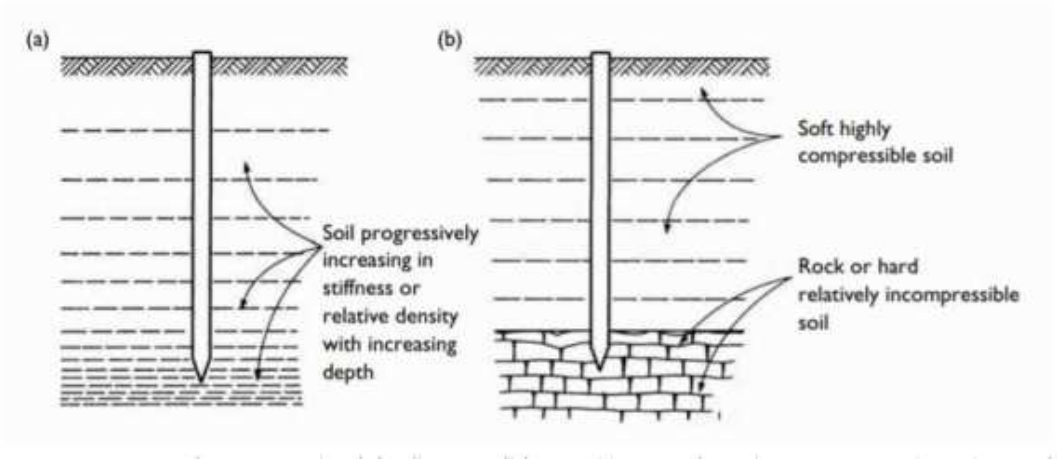

Figure 2.6.2. Types of bearing pile (Tomlinson, 1994)

However the function of a pile is a much more complex matter depending on various parameters, such as installation method, soil conditions, loading type etc.The selection of the proper pile type is very important and depends mostly on the location and type of structure, ground conditions, durability and cost (Tomlinson, 1994). According to the British Standard Code of Practice and Foundations there are three pile categories as follows:

- Large displacement piles, which are driven or jacked into the ground and displace the soil
- Small-displacement piles, which are also driven but they include rolled steel H, U or I sections and pipe or box sections driven in open end such the soil enters the hollow section

- Replacement piles (bored-and-cast-in-place piles), which are formed by first removing the soil by boring and afterwards placing steel reinforcement and concrete.

Driven piles are useful in offshore applications, or in very loose soils. Bored piles are more popular, especially in urban areas as there is minimal vibration and noise and can be used in cases of limited space available without risk of heave.

2.6.1 Piles under lateral loading

In the case of foundations of bridges, transmission towers, wind turbines, offshore structures and for other type of megastructures, piles are also subjected to lateral loads. The lateral load resistance, as well as the maximum deflection of the pile is critically important in the design of structures.

In pile foundations lateral loading could be:

- Static or dynamic forces on the pile head, e.g. due to wind, earthquakes, traction of braking vehicles, waves etc.
- Horizontal forces caused by soil displacement and act over the whole length of the pile, in piled walls, bridge pier foundations or piles for soil improvement, for example.

The behavior of the piles in horizontal loads depends on many factors as the relative stiffness of the pile soil system, the stress-strain relation describing the behavior of the soil as well as its strength properties and the fixity conditions of the pile head.

If we consider the case of an unrestrained pile at the head subjected to horizontal force, initially the load is carried by the surrounding soil close to the head of the pile. At low loading stages the soil behaves elastically but pressure is also transferred at greater depths. A rigid pile tends to rotate when passive resistance of the soil is exceeded if it is free headed, or translates horizontally if it is restrained. Flexible piles behave differently. The passive resistance at the lower part of the pile is infinite and rotation cannot occur. The lower part of the pile remains vertical and a plastic hinge is developed, as the pile fails in bending, at the maximum bending moment. If the pile is fixed headed, high bending stresses develop at the point of restraint and another plastic hinge may be created at that point. Failure mechanisms of piles are depicted in Figure 2.6.3.

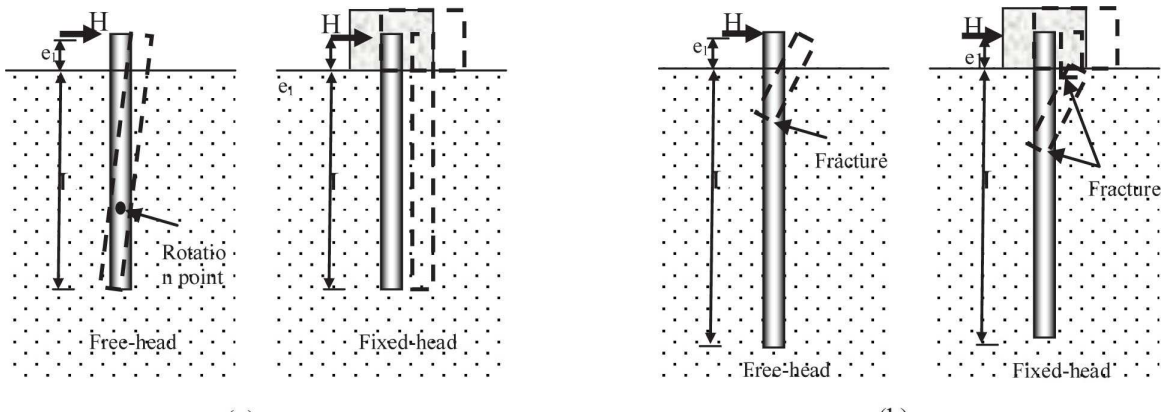

Figure 2.6.3. Failure mechanisms of rigid and flexible piles (Broms 1964)

The behavior of piles under lateral loads, as mentioned above is a complex matter as many factors interact. Dominant role plays the relative stiffness between the pile and the soil which defines the failure mechanism. Loading type plays a crucial factor for the degree of yielding of the soil. For solving lateral loaded piles some empirical methods have been developed with many simplifications and assumptions in order to provide simple solutions to such a complex matter. Such simple solutions have been provided by Broms (1964). Broms has established graphical relationships for the prediction of ultimate lateral resistance, examining separately rigid and flexible piles in cohesive and non-cohesive soils. Broms theory is an ultimate capacity method and both pile and soil develop their full inelastic response. The basic assumption is that pile movements are adequate to fully mobilize plastic capacities everywhere and elastic deflections are ignored. For long flexible piles in cohesive soils, which is the case to be examined later in this report, Broms (1964) assumed that as the passive resistance of the soil is infinite, the maximum horizontal load that a pile can carry is determined from the ultimate moment resistance of the pile material. In Figure 2.6.4 soil reactions and bending moments along the pile and the graph used to predict ultimate lateral resistance according to ultimate bending resistance, are illustrated.

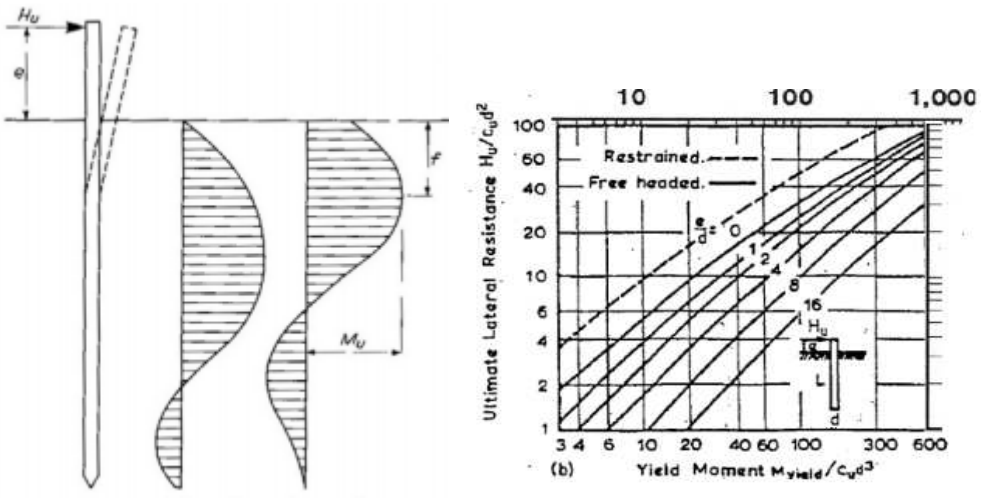

Figure 2.6.4. (a) Soil reactions and bending moments, (b) Ultimate lateral resistance, for free headed long piles in cohesive soils (Broms 1964)

The piles can be categorized also in respect to the ratio L/D (L=length, D=diameter). A short pile behaves and rotates as a rigid body under lateral loads and has a ratio L/D<10. A long pile has a high slenderness ratio (L/D >10) and after a certain length (active length lc) the rest of the pile remains inactive under lateral loading. Under vertical loading the forces are received by the friction of the pile walls at full length. The active length lc is the minimum length after which the displacement at the pile head under a certain lateral load remains unaffected.

According to Gazetas (1991) the equations that determine the active length in an elastic half-space, are dependent of the relative pile-soil stiffness and the soil elastic modulus distribution:

$$l_c \approx 1.5\, d \left(\frac{E_p}{E_s}\right)^{0.25}, \quad \text{for uniform distribution of Es} \qquad (2.6.1.1)$$

$$l_c \approx 1.5\, d \left(\frac{E_p}{\bar{E}_s}\right)^{0.22}, \quad \text{for linear increase of Es with depth} \qquad (2.6.1.2)$$

The maximum force a pile can undertake at any depth, is the sum of passive soil resistance, that bears movement of the pile and friction resistance at the sides, less active earth pressure

behind the pile. Lateral soil resistance along the pile, at first was calculated using force equilibrium on the developed passive soil wedge (Matlock 1970; Reese et al. 1975), or a "strain wedge" mode of soil failure (Ashour & Norris, 2000). These methods assumed that failure is related with the creation of a soil wedge near ground surface and lateral flow below the wedge. However this type of failure is not observed for all pile types e.g. batter or capped piles and therefore other solutions had to be found, independent of soil failure modes. A simplified approach for solving piles under lateral loading is to consider the pile as a beam and the soil instead of an elastic half-space, a medium consisted of discrete springs. When considering elastic behavior there are some analytical expressions to calculate pile head displacement and rotation, while for non-linear unelastic behavior the artifice of 'p-y' curves is employed. The p−y approach has been widely used to design piles subjected to lateral loading. Based on the Winkler foundation theory, the method models the lateral soil-structure interaction with empirically derived nonlinear springs. The 'p-y' curves represent the deformation of the soil at any given depth below the surface, caused by horizontally applied pressures until yielding of the soil. After yielding the deformation increases with constant pressure. The key to this method is that each discrete vertical area of soil has its only p-y curve which is independent of the stiffness of the pile as well as loading conditions below and above.

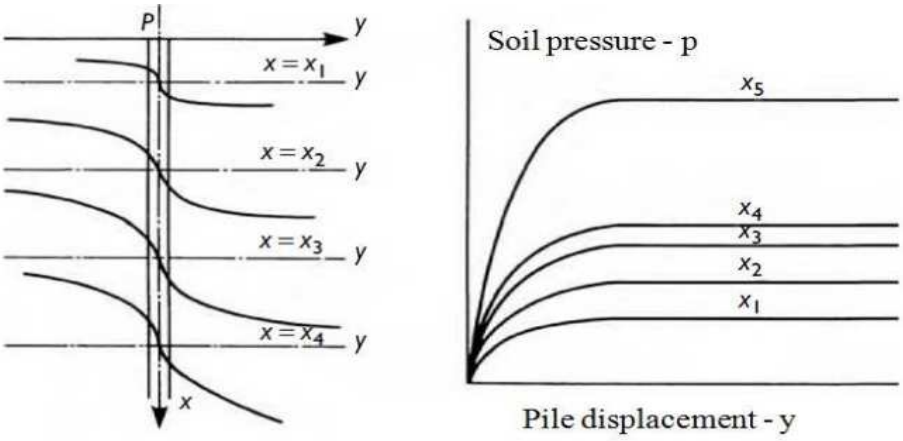

Figure 2.6.5. P-y curves (Matlock 1970)

3 Finite Element Analysis and constitutive models

3.1 Introduction

Finite element analysis is a numerical method used for solving complex mathematical or engineering problems by utilizing mathematical techniques. Numerical methods are the most suitable for solving problems that require representative simulations for the complex nonlinear behavior of materials in order to satisfy all the theoretical requirements. Finite Element Method Analysis is an extremely useful tool for evaluating a design, inspection of the performance of a product in real life, optimizing parameters and making comparisons between alternative solutions.

In this chapter the fundamentals of Finite Element Analysis are presented, emphasizing on constitutive modeling and elastoplastic material models. Consequently follows a brief presentation of PLAXIS Software which is utilized in the three dimensional analysis in this thesis.

3.2 Basic principles of Finite Element Analysis

In general FEM is an approximate method, that is utilized to solve complex problems that other methods are unable to. When the boundaries of the examined medium are complex most methods analytical solutions cannot be found, or lots of computer time is required. With FEM analysis a compatible field of functions defined throughout the material, which meet certain boundary conditions, is determined. With this approach, if we consider for example the problem of the displacement of a material, the initial problem of the determination of the field of displacements at each point of the material is transformed in the problem of determining a finite number of unknown coefficients. This is feasible with the division of the material into a number of distinguished elements. The functions used through these elements are simple and usually have polynomial form. This division of the continuum in individual small parts is the basis of FEA. This parts are called ‘finite elements’. The word finite is used to describe the limited number of degrees of freedom for each element. Each element consists of a number of nodes and each node has a number of degrees of freedom that correspond to the discrete values of the unknowns of the problem to

be solved. The whole, divided into elements, geometry is known as mesh, and the process of creating a mesh is called discretization.

The stages of FEM analysis to problems of elasticity (or generally deformation of materials) in two or three dimensions (Desai, 1979) are outlined below:

• Division of the examined field, in finite elements.

• Selecting appropriate functions for the distribution of unknown variables in each element

• Determining the functions linking the open deformation with the strain - displacement and the functions that connect the tension with stress-strain to connect the cause (tension, force) with the result (displacement) that is the unknown value.

• Construct the fundamental equations for each element (element equations).

• Aggregate by node of the element equations for definition of the final system and introduction of boundary conditions.

• Calculating the intensive state of each element as a function of the displacements at the nodes of the element.

• Calculation of the secondary values resulting from the solution (i.e. open deformations, tensions, etc.).

• Evaluation of the results.

Today a large number programs have been developed that solve composite engineering problems with the finite element method. By analyzing the system in its elements, individual behavior is more easily understood, and then the ability to synthesize and view the entire system allows the study of its total behavior (Valalas, 1981). The user should only define the appropriate geometry, construction process, material parameters and boundary conditions. However attention must be paid, as FEM is an approximate method. Accuracy and validity of the solutions need to be assessed with great care after the deep comprehension of the basic characteristics of the system being modeled and the expected response. Moreover the user should have a very good understanding of the limitations of the software used for the analysis .If a model is correctly set up, highly complicated problems can be solved, providing accurate results.

3.2.1 Discretization

As mentioned above the process of dividing the medium examined into smaller elements or segments is called discretization. The finite elements are interconnected at specific points called nodes, with straight or curved segments, creating a mesh, as shown in Figure 3.2.1. On each node correspond the physical quantities describing the cause and effect.

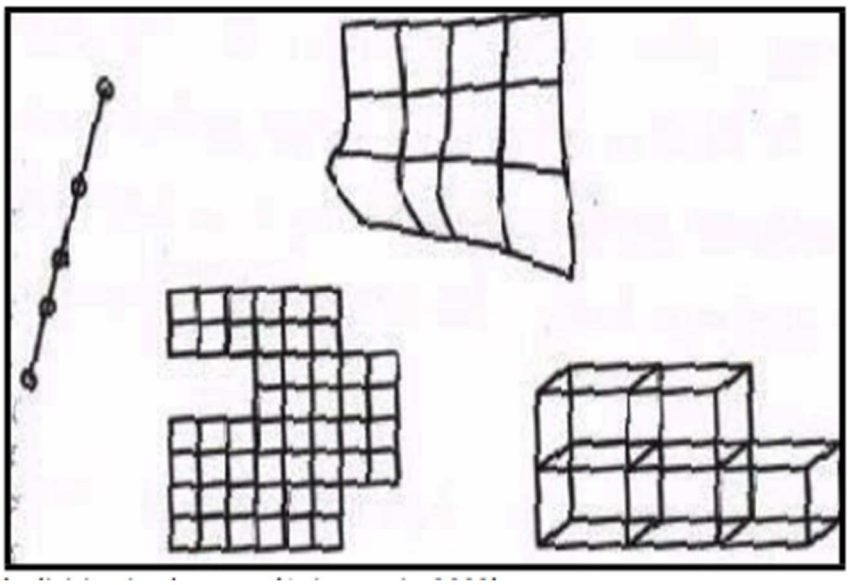

Figure 3.2.1. Body division in elements (Agioutantis 2002)

Creating a suitable mesh for an analysis is one of the keys for accurate results. If a mesh is too coarse the distribution of the variable investigated may be not resoluted adequately and if it is extremely fine, large calculation time will be needed and it is possible not to end up to a solution. Typical element shapes are triangular and rectangular for one dimensional analysis, quadrilateral for two dimensions, and pyramidal or prismatic for three-dimensions, respectively. The simplest forms of elements are those in which the number of the element nodes is equal to the number of sides. For linear functions in 2D and 3D the most common elements are illustrated in Figure 3.2.2 below.

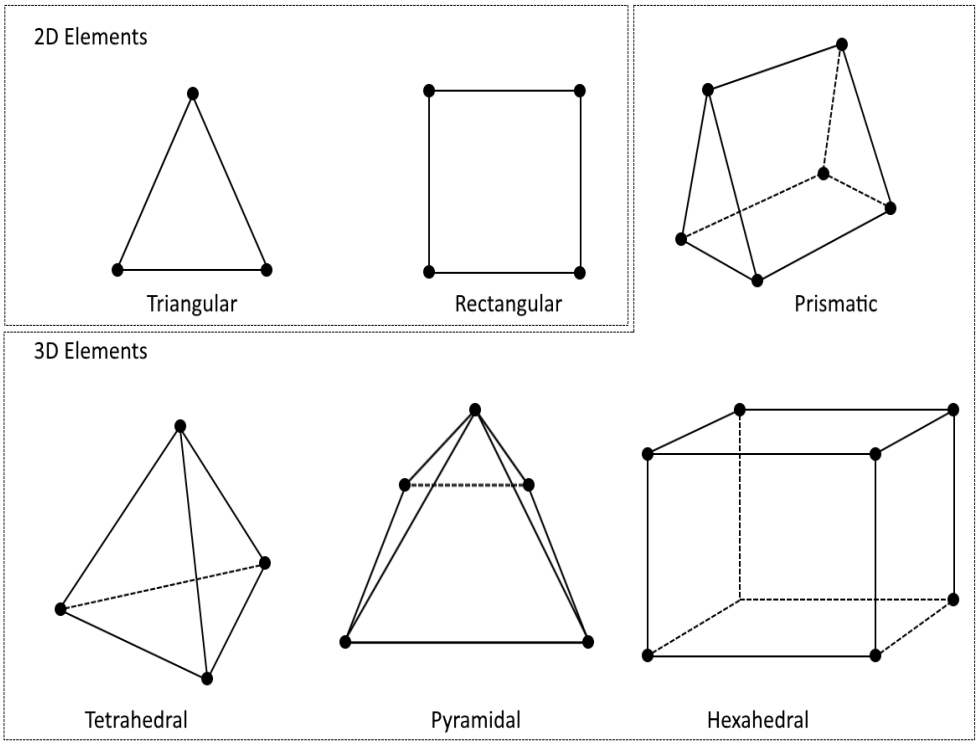

Figure 3.2.2. Node placement and geometry for 2D and 3D linear elements

The number of degrees of freedom of an element is the set of unknown variables that correspond to each element. An element may have two or more nodes and 1, 2, 3 or more degrees of freedom in each node, depending on the problem to be solved. In the usual cases of engineering problems, each node has two or three degrees of freedom that correspond to the vector components of the node displacement. For the successful simulation of the behavior of a medium with the FEM the proper discetization is essential. This process includes the following stages (Agioutantis, 2002):

• Selection of the geometry of the element

• Selection of the number of nodes and by extension the degrees of freedom of each element

• Selection of the form functions of each element

• Selection of the density of the grid

A common practice for selecting the geometry of an element is the use of smaller elements where large values or high deviations of the calculated variables are expected. It is possible, depending on the requirements of the problem, to increase the degrees of freedom of an element by adding more nodes, such as the use of a quadrilateral element with eight nodes.

The selection of functions that express the distribution of the unknown variables (e.g., displacements) to each element as a function of the values of the variables in the nodes is directly related to the desired precision in the calculations but also with the time for resolving the problem. These functions are called shape functions (Agioutantis, 2002)

3.2.2 Shape functions

The equations that define the approximate distribution of variables across the elements of a created mesh, are called shape functions. Shape functions can have any mathematical form, with most common the polynomial, as they are quite simple to differentiate and to integrate. In addition, the accuracy of the analysis can be improved by increasing the grade of the polynomial equations. High grade polynomial functions provide more accurate results. However, by increasing the grade of polynomial, calculation time is increased also.

In the general case, the displacement at each node of an element is expressed as a function of the generalized coordinates. For an element with two nodes the displacement is expressed as follows:

$$u=a1+a2y \tag{3.2.2.1}$$

where a1 and a2 contain the displacements, as well as the coordinates of nodes 1,2.

If in the above relation the vectors u are replaced with the individual components, it gives:

$$u1=a1+a1y1 \tag{3.2.2.2}$$

$$u2=a1+a2y2 \tag{3.2.2.3}$$

$$\{q\}=[A]\{a\} \tag{3.2.2.4}$$

where {q} is the vector of unknown displacements, [A] is the array with the coordinates of the element and {a} the unknown coefficients. Resolving we get:

$$u = \sum uiNi \quad (3.2.2.5)$$

Regarding to two-dimensional elements, the actions taken to connect cause-effect are summarized below, while for three-dimensional elements the actions are similar:

The displacement at each point of an element is expressed as a function of displacements at the nodes {ui} from the relationship:

$$u = N1u1 + N2u2 + N3u3 + N4u4 \quad (3.2.2.6)$$

The constitutive equations of behavior represented by relationships of the form:

$$\sigma ij = f(\varepsilon ij) \quad (3.2.2.7)$$

which can be written in the form of tables as follows:

$$\{\sigma\} = [E]\ \{\varepsilon\} \quad (3.2.2.8)$$

where table [E] represents a generalized record of the elastic properties of the material. The dynamic energy of each element arises as a sum of the internal energy as well as the work of the external forces that affect the element according to the relation:

Dynamic Energy = Internal Energy – External Forces Work

The External Forces belong to three categories:

- Field Forces (e.g. gravitational)
- Tensions (e..g hydrostatic)
- Point forces

The relationship that connects the force {F} that each node receives and the displacement {Q} is:

$$\{F\} = [K]\ \{Q\} \quad (3.2.2.9)$$

The dimension of the vector {F} for each element depends on the number of nodes of the element and on the degree of freedom of each node. For two-dimensional quadrilaterals,

there is a total of eight degrees of freedom. The physical significance of the matrix [K] may be given by an example of a pair of nodes, with a single degree of freedom connected by a virtual spring, where the coefficient of the matrix Kij represents the constant of the spring that connect the nodes (degrees of freedom) of the element (Agioutantis, 2002). It is obvious that the solution of the above equation over the vector of displacements will give the values of the unknown variables. However, in order to solve the individual equations, the boundary conditions applied to the solid must be defined and then the inversion of the global stiffness matrix [K] to be made.

3.2.3 Boundary conditions

After creating and correlating the individual equations of the elements, the definition of the boundary conditions follows. Without defining the boundary conditions is the system of equations cannot be solved because the global stiffness matrix cannot be reversed. In order to prevent uncontrolled movement in the form of a rigid body, restrictions called boundary conditions must be applied in order to keep the model in equilibrium.

There are three types of boundary conditions (Agiouantis, 2002):

• Determining the requested parameter (displacement). These conditions are called geometric and are also known as Dirichlet conditions.

• Determining the change of the requested parameter (derivative of the displacement). These conditions are called natural border conditions and are known as the Neumann conditions.

• Determining both of the above parameters or mixed conditions. These are known as the mixed boundary conditions. In a mixed boundary value problem, the solution is required to satisfy a Dirichlet or a Neumann boundary condition in a mutually exclusive way on disjoint parts of the boundary.

3.2.4 Material behavior models

The choice of the appropriate model of a material (e.g., soil, concrete, steel) and the values of parameters that define it is one of the most important factors for the successful numerical simulation of its behavior. These models are called constitutive models and basically they are stress-strain relations that represent the unique features of a real material in finite element analysis.

The simplest model that can be used is the linear elastic model. The material is assumed to be deformed linearly and isotropically, as given by the following relation:

$$\sigma_{ij} = \frac{E}{1+v} * \left[\varepsilon_{ij} + \frac{v}{1-2v} * \varepsilon_{\kappa\kappa} * \delta_{ij}\right] \quad (3.2.4.1)$$

where: σ_{ij} : the stress tensor indicating the intense condition in the body[MPa],

E : the modulus of elasticity of the material [MPa]

ν: the Poisson ratio of the material

ε_{ij} : the tensor of strain

δ_{ij} : the unit tensor (Kronecker delta).

For the case of deformation in one dimension, the relation turns into:

σ = Eε, where:

σ: the stress applied to the material [MPa],

E: modulus of elasticity [MPa].

There are many other, more complex, constitutive models that can describe the nonlinear behavior of materials. Such models approach the behavior of concrete. From a macroscopic point of view, the classical elastoplasticity can simulate the behavior of concrete particularly in the pre-peak regime. The basic concepts of elastoplastic material behavior models are described in the following paragraph.

3.2.5 Elastoplastic constitutive models

The fundamentals of the theory of elastoplastic constitutive models will be given with the example of the rheological model, shown in Figure 3.2.3 below.

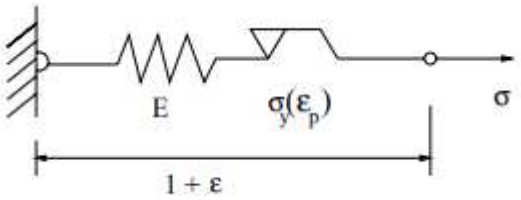

Figure 3.2.3. Elastoplastic serial model of spring and friction element (Willam, 2003)

$$\dot{\varepsilon} = \dot{\varepsilon}^e + \dot{\varepsilon}^p \qquad (3.2.5.1)$$

The basic concept of elastoplasticity is the division of strain rate into elastic and inelastic components.

The state of stress in the elastic spring shown in figure 3.2.3 is limited by the slip conditions of the friction element. The behavior in the elastic regime, where $\sigma \leq \sigma_y$ is described by Hooke's law,

$$\dot{\varepsilon}_e = \frac{\dot{\sigma}}{E} \qquad (3.2.5.2)$$

While the plastic response is activated when stress reaches the yield condition $\sigma = \sigma_y$. In that case,

$$\dot{\varepsilon}_p = \frac{\dot{\sigma}}{E_p} \qquad (3.2.5.3)$$

Consequently,

$$\dot{\varepsilon} = \frac{\dot{\sigma}}{E} + \frac{\dot{\sigma}}{E_p} = \frac{\dot{\sigma}}{E_{ep}} \qquad (3.2.5.4)$$

With the elastoplastic tangent stiffness,

$$E_{ep} = \frac{E\,E_P}{E + E_P} \qquad (3.2.5.5)$$

According to the value of the elastoplastic tangent stiffness the response of the material can be described as:

- Hardening when $E_{ep} > 0$
- Softening when $E_{ep} < 0$
- Perfectly plastic when $E_{ep} = 0$

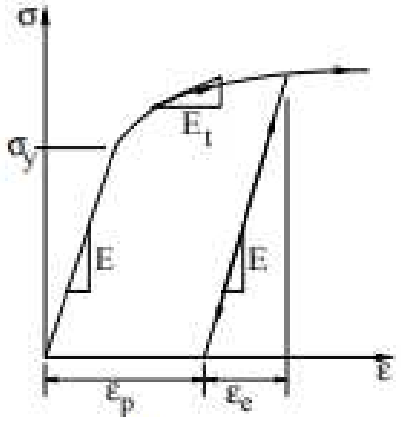

Figure 3.2.4. Load-Unload-Reload response of an elastoplastic material (Willam 2003)

Moreover a yield condition must be defined in the form of a yield function as:

$$F(\sigma) = |\sigma| - \sigma_y = 0 \tag{3.2.5.6}$$

which acts as a threshold condition when stress demand reaches the yield capacity if the material. Therefore plastic loading requires: (i) the stress path to reach the yield strength and (ii) under persistent plastic action the criterion $\dot{\varepsilon}\,\varepsilon > 0$ to be satisfied as $\dot{\varepsilon}_p = \frac{E}{E+E_p}\,\dot{\varepsilon}$. After the definition of the yield surface, which defines whether the material behaves elastically or plastically, the plastic flow rule needs to be determined. It is roughly the relationship between the plastic strain and stress, as follows:

$$d\varepsilon_{ip}^{p} = d\lambda \frac{df}{d\sigma_{ij}}, \quad \text{where } f \text{ is the yield surface} \tag{3.2.5.7}$$

$$d\varepsilon_{ip}^{p} = d\lambda \frac{dg}{d\sigma_{ij}}, \quad \text{where g is the plastic potential function} \tag{3.2.5.8}$$

Lastly a Hardening rule describes the evolution of the yield surface sand other internal variables with plastic strain,

$$f(\sigma) = k\,(\,\varepsilon^{p}\,) \tag{3.2.5.9}$$

Two basic types can be distinguished: Isotropic hardening and kinematic hardening

3.3 Plaxis Finite Element Software

PLAXIS is a finite element program, developed for the analysis of deformation, stability and groundwater flow for various types of geotechnical applications. Initially a 2D finite element code was created for the analysis of river embankments on the soft soils of Holland. Gradually, PLAXIS was extended to cover most areas of geotechnical engineering and in 1998 the first Plaxis 2D for windows was released. The need for 3D modeling in order to realistically describe an engineering problem and improve the accuracy of results led to the development of PLAXIS 3D program. Plaxis 3D is a full three-dimensional finite element program that uses a convenient graphical user interface that enables users to easily generate a geometry and a finite element mesh. Structures and foundations can be modeled by structural elements. These elements are fixed end or node to node anchors, geogrids for soil reinforcement, plates, beams and embedded beams, which are beam elements used as piles, rock bolts or grout bodies, including interface elements to model soil-structure interaction. Volume elements can also be used in the design. These volume elements are used to model soil materials, or structures such as piles. Specific material models are included to describe the behavior of these soil (layers) and structures realistically. Those material models use constitutive laws to capture the behavior of real materials. Depending on the problem to be solved different types of analysis are available, e.g., plastic, dynamic consolidation etc. Also, different construction stages to represent real construction sequence can be added. The main advantage of PLAXIS 3D program is that it can be used by engineers that are not experts in FE analysis. However the users need to be able to evaluate the output results and before modeling to have fully understood the problem under investigation to select proper parameters, boundary conditions etc. It is also important to compare results with other solutions such as empirical formulas, analytical solutions or even hand calculations. As mentioned above Plaxis provides a big number of different constitutive models to describe the actual behavior of material. The constitutive models in this thesis are described in the following chapters.

3.4 Constitutive models used in numerical simulation

3.4.1 Mohr-Coulomb model

The Mohr-Coulomb model is a linear elastic - perfectly plastic model.

The basic principle of elastoplasticity, as mentioned above, is that total strain or strain rate is divided in two components , an elastic part and a plastic part :

$$\underline{\varepsilon} = \underline{\varepsilon}^e + \underline{\varepsilon}^p \qquad \dot{\underline{\varepsilon}} = \dot{\underline{\varepsilon}}^e + \dot{\underline{\varepsilon}}^p \qquad (3.4.1.1)$$

The first part contains elastic reversible on unloading strains, while the second irreversible, plastic strains.

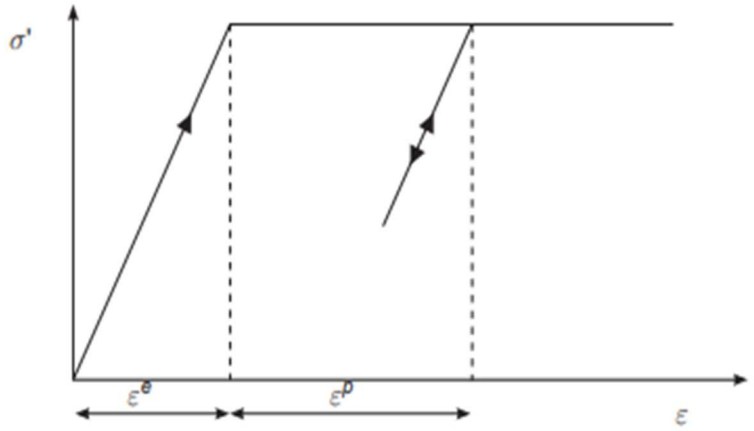

Figure 3.4.1. Basic idea of an elastic- perfectly plastic model (PLAXIS 3D,2018)

The linear part of the above diagram is based on Hooke's law and the perfectly plastic on the Mohr-Coulomb failure criterion.

Generally in order to evaluate whether yielding occurs or not a yield function f is introduced. When the condition $f = 0$ is satisfied plastic yielding occurs. This condition can be presented as a surface in principal stress space. For perfectly plastic models this surface is fixed and not affected by straining. Hooke's law is used to relate the stress rates to the elastic strain rates. Substitution of Eq.(3.4.1.1) into Hooke's law leads to:

$$\dot{\underline{\sigma}}' = \underline{\underline{D}}^e \dot{\underline{\varepsilon}}^e = \underline{\underline{D}}^e \left(\dot{\underline{\varepsilon}} - \dot{\underline{\varepsilon}}^p\right) \qquad (3.4.1.2)$$

For Mohr-Coulomb failure criterion, except the yield function f a plastic potential function g is introduced. In general, the plastic strain rates are written as:

$$\underline{\dot{\varepsilon}}^{p} = \lambda \frac{\partial g}{\partial \underline{\sigma}'} \tag{3.4.1.3}$$

In which λ is the plastic multiplier. For purely elastic behavior λ is zero, where as in the case of plastic behavior λ is positive:

$$\lambda = 0 \quad \text{for:} \quad f < 0 \quad \text{or:} \quad \frac{\partial f^{T}}{\partial \underline{\sigma}'} \underline{\underline{D}}^{e} \underline{\dot{\varepsilon}} \leq 0 \quad \text{(Elasticity)} \tag{3.4.1.4a}$$

$$\lambda > 0 \quad \text{for:} \quad f = 0 \quad \text{and:} \quad \frac{\partial f^{T}}{\partial \underline{\sigma}'} \underline{\underline{D}}^{e} \underline{\dot{\varepsilon}} > 0 \quad \text{(Plasticity)} \tag{3.4.1.4b}$$

These equations may be used to obtain the following relationship between the effective stress rates and strain rates strain rates for elastic perfectly-plastic behavior:

$$\underline{\dot{\sigma}}' = \left(\underline{\underline{D}}^{e} - \frac{a}{d} \underline{\underline{D}}^{e} \frac{\partial g}{\partial \underline{\sigma}'} \frac{\partial f^{T}}{\partial \underline{\sigma}'} \underline{\underline{D}}^{e} \right) \underline{\dot{\varepsilon}} \tag{3.4.1.5}$$

$$d = \frac{\partial f^{T}}{\partial \underline{\sigma}'} \underline{\underline{D}}^{e} \frac{\partial g}{\partial \underline{\sigma}'} \tag{3.4.1.6}$$

If the material behavior is elastic, as defined by Eq. (3.4.1.4a), the value of α is equal to zero, whilst for plasticity, α is equal to unity.

3.4.1.1 Formulation and input parameters of the Mohr-Coulomb model

The Mohr Coulomb yield condition is an extension of Coulomb's friction law. The full Mohr-Coulomb yield condition consists of six yield functions when formulated in terms of principle stresses (Smith & Griffith 1982). The condition $f = 0$ for all yield functions represent a fixed hexagonal cone, as illustrated in Figure 3.4.2.

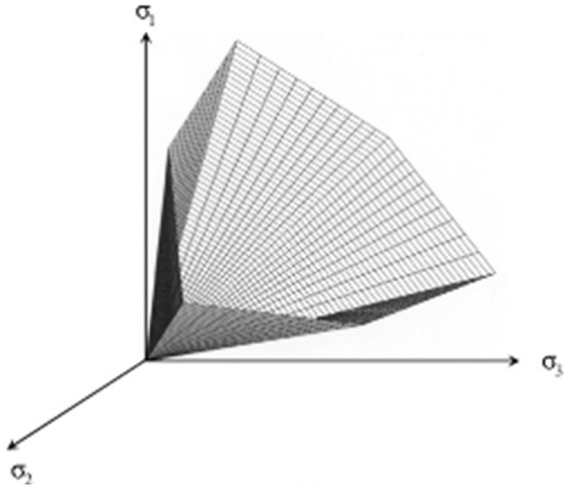

Figure 3.4.2. Mohr-Coulomb yield surface in principal stress space (PLAXIS 3D, 2018)

In addition to the yield functions, six plastic potential functions are defined.

The Mohr-Coulomb yield and plastic potential functions in p'-q space are defined in terms of principle stresses as follows:

$$f_{2b} = \frac{1}{2}(\sigma'_1 - \sigma'_3) + \frac{1}{2}(\sigma'_1 + \sigma'_3) - c\cos\varphi \leq 0 \quad (3.4.1.7)$$

$$g_{2b} = \frac{1}{2}(\sigma'_1 - \sigma'_3) + \frac{1}{2}(\sigma'_1 + \sigma'_3)\sin\psi \quad (3.4.1.8)$$

The above yield function contains two plastic model parameters, friction angle φ and cohesion c, while a third plasticity parameter is included in the plastic potential function, the dilatancy angle ψ. For c >0 the criterion allows for tension.

When tensile strength needs to be taken into account tension cut-off must be defined. In this case Mohr circles with positive principle stresses are allowed. The tension cut off introduces an additional yield surface, defined in p'-q space as:

$$f_4 = \sigma'_1 - \sigma_t \leq 0 \quad (3.4.1.9a)$$

$$f_6 = \sigma'_3 - \sigma_t \leq 0 \quad (3.4.1.9b)$$

From the above condition, another parameter needs to be defined, which is the allowable tensile stress σ_t . Besides the aforementioned parameters accounting for plasticity and tensile strength, two elastic parameters are required, the elastic Young modulus E and Poisson's ratio v. The input parameters required for the Mohr-Coulomb model, are listed in Table 3.1.

Table 3.1: Input parameters for Mohr-Coulomb model

Parameter	Description	Unit
E	Young's modulus	kN/m^2
v	Poisson's ratio	-
c	Cohesion	kN/m^2
φ	Friction angle	^{o}
ψ	Dilatancy angle	^{o}
σ_t	Tension cut-off / tensile strength	kN/m^2

3.4.2 Macroscopic model

3.4.2.1 Introduction

In this chapter a macroscopic Mohr-Coulomb based approach for the behavior of reinforced concrete circular elements, as developed by Gerolymos et al., (2014) is described.

This approach gives a realistic constitutive law for the behavior of circular RC elements in numerical simulations. It was first introduced to describe the elastoplastic response of piles. Until the development of this approach, pile failure was ignored and no installation effects were taken into account.

With this phenomenological approach, the following were succeeded:

- Inclusion of the pile material behavior into the soil-foundation system
- Incorporation of the effect of load combination to the alteration of pile material properties
- Simulation in a uniform approach the elastoplastic pile response
- Realistic representation of pile soil interaction

3.4.2.2 Analytical solution

If we consider a circular reinforced concrete pile subjected to combined bending moment and axial force, and isolate a cross-section, there is the following stress distribution.

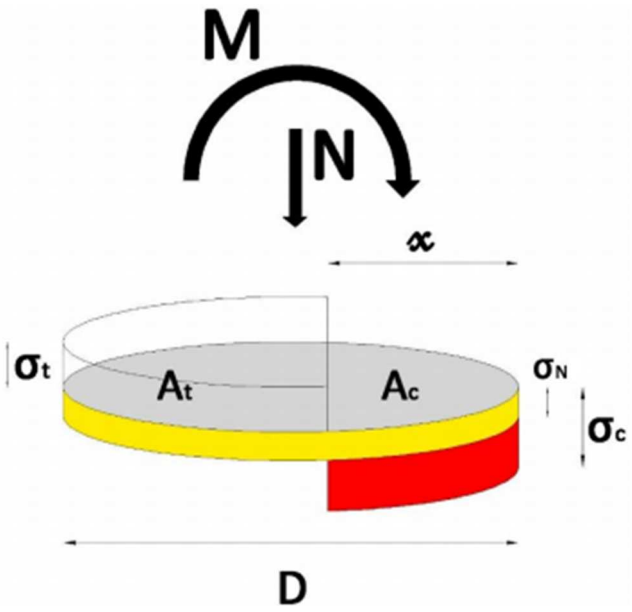

Figure 3.4.3 Stress distribution on a random pile section under moment and axial load in full plasticity (Papakyriakopoulos , 2013).

By applying force equilibrium in the axial direction, of a pile section subjected to moment and axial load in full plasticity one obtains:

$$(\sigma_c - \frac{4N}{\pi D^2})\, A_c = (\sigma_t + \frac{4N}{\pi D^2})\, A_t \qquad (3.4.2.1)$$

In which σ_c and σ_t are the compressive and tensile strength of the composite section, respectively:

$$\sigma_c = \frac{2c\cos(\varphi)}{1-\sin(\varphi)}, \quad \sigma_t = \frac{2c\cos(\varphi)}{1+\sin(\varphi)} \qquad (3.4.2.2)$$

In the equations above two plastic parameters of the Mohr-Coulomb model are included, cohesion c and internal friction angle φ. In Eq. (3.4.2.1), A_c and A_t are the pile section areas under compression and tension respectively, defined as:

$$A_c = \int_0^{x_0} 2\sqrt{x(D-x)}\, dx, \quad A_t = \int_{x_0}^{D} 2\sqrt{x(D-x)}\, dx \qquad (3.4.2.3)$$

in which D is the pile diameter and x_0 is abscissa of the neutral axis. By applying moment limit equilibrium with respect to the center of the pile section, the following equation is derived:

$$M = \sigma_c \int_0^{x_0} 2\sqrt{x(D-x)}\ (x_0 - x)dx + \sigma_t \int_{x_0}^{D} 2\sqrt{x(D-x)}\ (x_0 - x)dx + \left(\frac{D}{2} - x_0\right) N \quad (3.4.2.4)$$

Eqs (3.4.2.1) and (3.4.2.4) form a non-linear algebraic system. For a known pile diameter and combination of bending moment-axial force at failure conditions there are three unknowns: c , φ and x_0 . This system can be solved with the use of a genetic-algorithm based optimization procedure, utilizing MATLAB. For a predefined M-N failure envelope is best fit is targeted by minimizing the relative root mean squared error (rRMSE) of the bending moment at failure:

$$\mathrm{rRMSE(M)} = \sqrt{\frac{1}{n}\sum_{i=1}^{n}\left(\frac{M_i - M_{T,i}}{M_{T,i}}\right)^2} \quad (3.4.2.5)$$

In which M_i is the bending moment computed by Eq. (3.4.2.4) , $M_{T,i}$ is the target bending moment, and n, the number of pairs that define the failure envelope.

This simplified Mohr-Coulomb based constitutive law can be reduced to a Tresca with tension cut-off, by simply equating the compressive strength in Eq. (3.4.2.1) with $\sigma_c = 2c$, and σ_t with the tension cut-off.

3.4.3 Concrete model

3.4.3.1 Introduction

As mentioned in Chapter 1, generally when modeling concrete elements in geotechnical applications, linear elastic approach is adopted due to their high stiffness compared to the one of the soil. However, in not a few cases, the real behavior of structural concrete as a composite nonlinear material must be represented for a correct design.

For this reason the concrete material model was introduced, as an advancement of Shotcrete material model. Shotcrete was first implemented in the finite element software PLAXIS 2D 2012 (Brinkgreve et al. 2012) in cooperation with Graz University of Technology, to model shotcrete linings in a more realistic way. As Shotcrete linings are subjected in high loads almost immediately after their application, the influence of time dependent properties on the deformations and bearing capacity is significant. The models used before Shotcrete assumed linear elastic material behavior, with a stepwise increase of the modulus of elasticity (Schädlich & Schweiger, 2014). This approach resulted in higher bending moments than in reality, due to the fact that the reduction of stiffness due to cracking of concrete was not considered leading to over-dimensioning of the structure.

The real complex nonlinear behavior of concrete needs to be taken into account, not only in tunneling, but also in other geotechnical applications. These could be soil reinforcement, soil improvements, concrete structures such as piles, beams or retaining walls etc. While Shotcrete model was mainly developed to model the behavior of shotcrete, it has also proven useful in applications related to soil improvements, for example jet grout columns. Since 2017 Shotcrete material was almost exclusively used in Plaxis 2D modeling, as it was not so adequately tested in Plaxis 3D and in cases suffered from mesh dependency.

The concrete model, at is present formulation is a part of Plaxis standard material library since the release of PLAXIS 2D 2018 and PLAXIS 3D 2018 and it is considered the best standard model in Plaxis for modeling concrete elements.

3.4.3.2 Formulation of the concrete model

As mentioned above, concrete model is an elastoplastic model for simulating the strain hardening-softening behavior, time dependent strength as well as creep and shrinkage (Schädlich & Schweiger, 2014). Hence the total strain in the model is determined not only by an elastic term and a plastic term, as LEPP model, but also a creep term and a shrinkage term

$$\underline{\varepsilon} = \underline{\varepsilon}^{e} + \underline{\varepsilon}^{p} + \underline{\varepsilon}^{cr} + \underline{\varepsilon}^{shr} \qquad (3.4.3.1)$$

The concrete model employs a composite yield surface. To account for plasticity a Mohr-Coulomb yield surface for deviatoric loading and a Rankine yield surface for tensile loading is adopted (Figure 3.4.4).

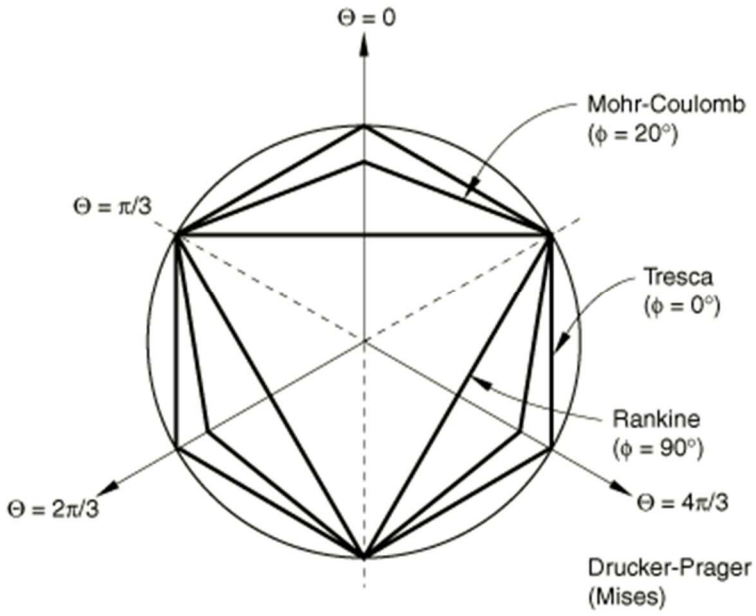

Figure 3.4.4. Mohr-Coulomb and Rankine yield surfaces in deviatoric plane (Hibbit, Karlsson & Sorensen, 2014)

The adoption of separate yield functions for compression and tension gives the user the ability, according to the problem under investigation (i.e. compression or tension), to calibrate the proper strength parameters. The yield functions of the model are given below:

$$Fc = \frac{\sigma_1 - \sigma_3}{2} + \frac{\sigma_1 + \sigma_3 - 2\sigma_{rot}}{2} \quad \frac{f_{cy}}{2\sigma_{rot} + f_{cy}} \tag{3.4.3.2}$$

$$Ft = \sigma_1 - f_t \tag{3.4.3.3}$$

Where f_{cy} and f_t are the uniaxial compressive and tensile yield stresses and σ_{rot} is the intersection of the Mohr-Coulomb failure envelope and the isotropic axis. For a given maximum angle of friction φ_{max} , σ_{rot} can be written as:

$$\sigma_{rot} = \frac{f_c}{2}\left(\frac{1}{\sin\varphi_{max}} - 1\right) \tag{3.4.3.4}$$

3.4.3.3 Strain hardening and softening behavior

Compression

Schütz, Potts and Zdravkovic (2011), proposed the division of stress-strain curve in four parts to describe the behavior of concrete in compression. These parts are:

- Part I - quadratic strain hardening
- Part II - linear strain softening
- Part III - linear strain softening
- Part IV - constant residual strength

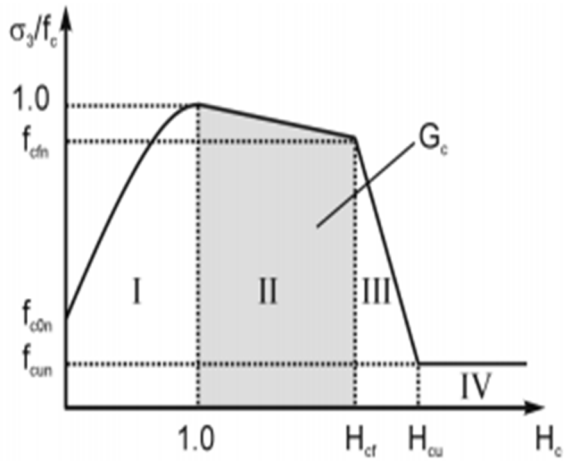

Figure 3.4.5. Normalized stress-strain curve in compression (PLAXIS 3D, 2018)

As shown in Figure 3.4.5 normalized values are used for both axes. On the horizontal axis a normalized strain hardening/softening parameter (H_c= ε_3^p / ε_{cp}^p) is plotted against the ratio between the principal stress σ_3 and the concrete strength f_c , on the vertical axis. On the horizontal axis, ε_3^p represents the compessive principal plastic strain and ε_{cp}^p represents the plastic peak strain in uniaxial compression. On the vertical axis several normalized stress values are distinguished. For each part of the curve the stress-strain relation is further described (PLAXIS 3D, 2018)

Part I describes the behavior of cracked concrete before it reaches its peak strength.
The uniaxial yield stress f_{cy} is mobilized with H_c according to a quadratic function:

$$f_{cy,I} = f_c \left(f_{c0n} + (1 - f_{c0n})\left(2H_c - {H_c}^2\right)\right) \quad (3.4.3.5)$$

where f_{c0n} represents the point at which yielding starts, called "Normalized initially mobilised strength" (Schädlich & Schweiger, 2014).

Part II describes the linear softening branch until failure strength is reached. Full mobilization of f_c coincides with H_u=1, where linear softening starts until the failure strength $f_c = f_{cfn} f_c$ is reached at $H_{cf} = \varepsilon_{cf}^p / \varepsilon_{cp}^p$:

$$f_{cy,II} = f_c \left(1 + \left(f_{cfn} - 1\right)\left(\frac{H_c - 1}{H_{cf} - 1}\right)\right) \quad (3.4.3.6)$$

Plastic failure strength ε_{cf}^p is calculated from the fracture energy in compression G_c, and the characteristic length of the finite element *Leq*, as follows

$$\varepsilon_{cf}^p = \varepsilon_{cp}^p - \frac{2G_c}{\left(1 + f_{cfn}\right) f_c L_{eq}} \quad (3.4.3.7)$$

The characteristic length of the average element size is calculated from the average element size A_{el}, of the created mesh.

In part III of the curve linear softening takes place and the plastic ultimate strain ε_{cu}^{p} is calculated as follows:

$$\varepsilon_{cu}^{p} = \varepsilon_{cf}^{p} - \frac{2f_c(f_{cfn} - f_{cun})}{E} \quad (3.4.3.8)$$

where f_{cun} is the normalized residual strength and E Young's modulus of elasticity.

The yield stress f_{cy} for this part of the curve is :

$$f_{cy,III} = f_c\left(f_{cfn} + (f_{cun} - f_{cfn})\left(\frac{H_c - H_{cf}}{H_{cf} - H_{cu}}\right)\right) \quad (3.4.3.9)$$

where $H_{cu} = \varepsilon_{cu}^{p}/\varepsilon_{cp}^{p}$.

In the last part IV the residual strength remains constant with increasing strain:

$$f_{cy,IV} = f_c f_{cun} \quad (3.4.3.10)$$

Tension

The response of concrete material under tension is characterized by a linear elastic hardening behavior until the peak tensile strength f_t is reached, and a linear softening behavior until the ultimate tensile strength (Figure 3.4.6)

On the horizontal axis a normalized strain softening parameter H_t is plotted against the ratio between the principal stress σ_1 and the concrete tensile strength f_t , on the vertical axis, where :

$H_t = \varepsilon_1^p / \varepsilon_{tu}^p$ with ε_1^p = major principal plastic strain and ε_{tu}^p = plastic ultimate strain in uniaxial tension as:

$$f_{ty} = f_t\,(1 + (f_{tun} - 1)H_t) \qquad (3.4.3.11)$$

Similar to compression ultimate peak strain is tension is derived from the fracture energy in tension G_t, as follows:

$$\varepsilon_{tu}^p = \frac{2G_t}{(1 + f_{tun})f_t L_{eq}} \qquad (3.4.3.12)$$

Once the residual strength is reached, $f_{tu} = f_{tun}\ f_t$ no further softening occurs.

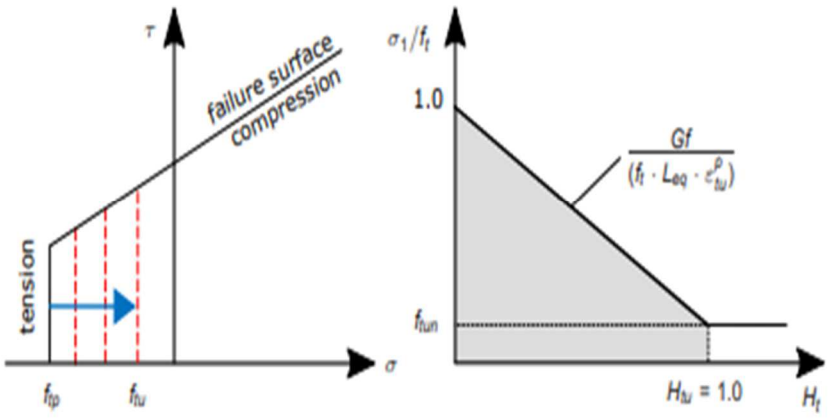

Figure 3.4.6. Tension softening (Schädlich & Schweiger, 2014b)

3.4.3.4 Input parameters

In order to describe the real behavior of structural concrete, including strain hardening and softening, creep and shrinkage Plaxis requires the input of 25 parameters. In this thesis, time dependent behavior of concrete is not investigated. All related to this study parameters are listed together with their range of recommender values, in Table 3.2 below and explained in detail.

Table 3.2: Input parameters of concrete model with recommended values

Parameter	**Description**	**Recommended values**	**Unit**
E_{28}	Young's modulus of cured concete at t_{hydr}	[25, 30]	GPa
v	Poisson's ratio	-	-
$f_{c,28}$	Uniaxial compressive strength of cured concrete at t_{hydr}	Depending on strength class	kN/m^2
f_{c0n}	Normalized initially mobilized strength	[0.10, 0.25]	-
f_{cfn}	Normalized failure strength	[0.1]	-
f_{cun}	Normalized residual strength	[0.1]	-
$G_{c,28}$	Compressive fracture energy of cured concrete at t_{hydr}	[30,70]	kN/m
φ_{max}	Maximum friction angle	[35,43]	^{o}
ψ	Dilatancy angle	[0,10]	^{o}
$f_{t,28}$	Uniaxial tensile strength of cured concrete at t_{hydr}	Depending on strength class	kN/m^2
f_{tun}	Ratio of residual vs.peak tensile strength	[0]	-
$G_{t,28}$	Tensile fracture energy of cured concrete at t_{hydr}	[0.05, 0.15] for plain Shotcrete	kN/m
ε_{cp}^{p}	Uniaxial plastic failure strain	[-0.0007,-0.0012]	-
a	Increase of ε_{cp} with increase of confining pressure	[16,20]	-

In this thesis concrete of class C30/37 is considered. Compressive strength 30 MPa is derived from uniaxial compression tests in cylindrical specimens and 37 MPa from cubic specimens. Concrete strength and stiffness parameters are listed in Table 3.3.

Table 3.3 Concrete strength and stiffness properties

Parameter	**Value**	**Unit**
f_{ck}	30	MPa
f_{cm}	38	MPa
f_{ctk}	2	MPa
E_{cm}	33	GPa
E_c	30	GPa

Firstly, the modulus of elasticity, $E_{28,}$ and the Poisson's ratio, v, need to be defined. The modulus of elasticity depend on concrete class, therefore it is taken equal to 30 GPa. For the Poisson's ratio, a value of 0.2 can be assumed.

Concrete compressive and tensile strengths are both defined from concrete class, as mentioned above (Table 3.3). The next parameters to be defined are the normalized values of concrete compressive and tensile strength. These are expressed as ratios of the compressive peak strength.

First the normalized yield strength parameter, f_{c0n} , needs to be given. Usually this value is considered to be the 1/3 of the uniaxial compressive strength. The next parameter to be defined is the normalized failure strength, f_{cfn}. Results from uniaxial compression tests carried out by Van Mier (1984), indicate that failure occurs at a stress level equal to 84% - 85% of peak strength. The last normalized parameter regarding the compressive behavior of concrete is the residual compressive strength, f_{cun} . According to Reinhardt & Xu (1999) it is estimated that residual strength in compression is around 10% of the peak strength. The last parameter related to compression, is fracture energy $G_{c,28}$. The compressive fracture energy Gc is equal to the area between peak and failure strength/strain. It describes the energy needed before the concrete starts to fail after reaching peak strength and is an determining factor for describing the concrete stress-strain behavior. When using the concrete material model the fracture energy has to be chosen such that the right values of strain are obtained at the different stresses, as it defines plastic failure strain, ε_{cf}^{p} and plastic ultimate strain, ε_{cu}^{p} , according to Eq. (3.4.3.7) and (3.4.3.8).

For the tensile behavior of concrete , the normalized residual strength, f_{tun} , and tensile fracture energy $G_{t,28}$ need to be defined. According to Dai & Gao (2014) the residual tensile strength is around 5% of the peak tensile strength, although in most cases zero tensile residual strength is considered. $G_{t,28}$ represents the area under the normalized stress-strain curve and it is the energy dissipated due to cracking in tensile loading. Strain at failure, ε_{tu}^{p} , is determined by this parameter, according to Eq. (3.4.3.12).

A strain parameter that needs to be imputed, is the plastic peak strain, ε_{cp}^{p}, which represents the strain at peak strength. It marks the beginning of the post - peak, softening behavior, in a uniaxial compression test. Peak strain according to experimental results is around 2 ‰. As a result the appropriate value for the plastic peak strain ε_{cp}^{p} is 1‰, as for concrete with f_{ck}= 30 MPa and E = 30 GPa , the elastic strain is 1‰, respectively.

For the definition of the parameters φ_{max}, ψ and *a* triaxial tests need to be held. φ_{max} is the angle of internal friction and ψ the dilatancy angle of concrete material. The angle of friction according to Vermeer & de Borst (1984) is 35°, while according to Candappa et al. (2001) is 43°. In this thesis an angle of friction equal to 40° is considered. The dilatancy angle of structural concrete is around 13° (Vermeer & de Borst, 1984) under normal conditions. In this study Plaxis proposed values 0-10 degrees will be adopted.

Parameter α quantifies the impact of confinement. To account for increasing ductility with confining pressure in a triaxial compression test parameter a is used to describe the increase of plastic strain of confined concrete, according to the following relation:

$$\varepsilon_{cp} = \varepsilon_{cp,UC}\left(1 + \alpha\frac{\sigma_1}{-f_c}\right) \qquad (3.4.3.13)$$

In the subject under investigation the impact of these parameters $(\alpha, \varphi_{max}, \psi)$ is rather small, and as a result proposed values are taken into account without deeper investigation. Moreover only unconfined concrete is modeled in this thesis, so parameter a is taken equal to 0.

3.4.4 On the parameters G_c , G_t

Introduction

Fracture energy parameters describe the softening behavior of concrete in tension and compression. Cracking is the cause of failure of concrete both for compression and tension. In compression, extensive cracking leads to crashing. The evolution of cracks until maximum compressive strength is illustrated in Figure 3.4.7 below.

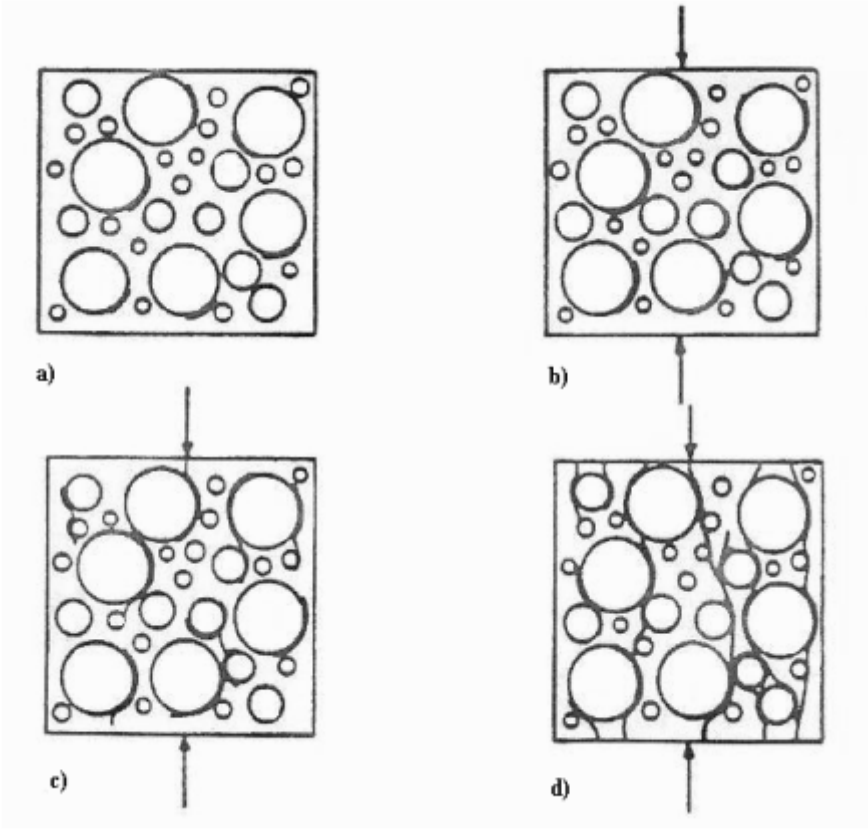

Figure 3.4.7. Evolution of cracks until peak compressive strength, (a) prior to loading, (b) 65% of ultimate load (c) 85% of ultimate load (d) peak strength (Kotsovos and Newman, 1977)

When concrete reaches the peak strength the critical crack length is reached. After that, follows severe crack propagation and the load that can be carried out decreases. In tension, cracking is a more discrete phenomenon. In contrast to compression failure under tensile loading is local, as areas of concrete may remain intact.

In finite element analysis of cracking, a general problem that researchers faced is mesh dependency of results. Especially when strain softening was introduced it was discovered

that the convergence properties were incorrect and the calculation results were not objective with regard to the analyst's choice of the mesh, i.e., the results significantly change if the mesh is refined (Bazant and Cedolin, 1979, 1980, 1983). The effect of mesh size can be illustrated by a rectangular panel subjected to a prescribed vertical displacement. Two panels with different mesh sizes are loaded and the load-deflection diagram is extracted (Figure 3.4.8).

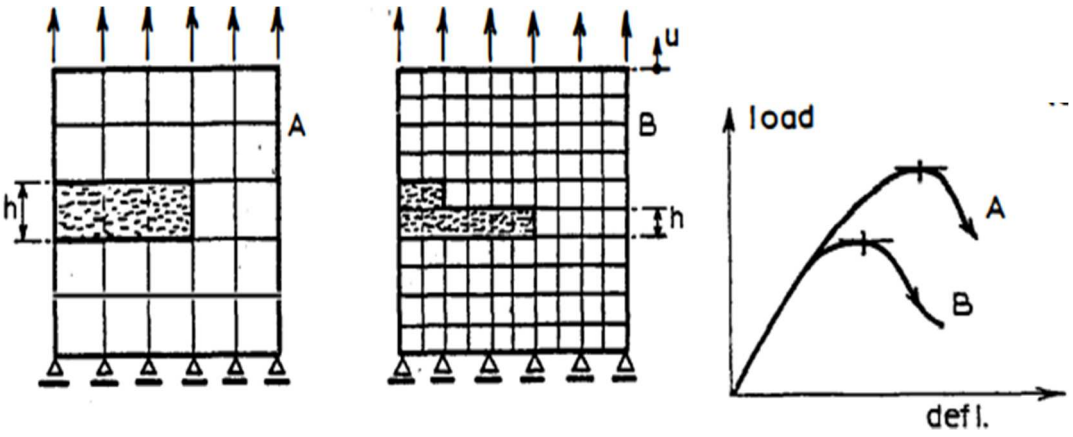

Figure 3.4.8. (a) Panels of different mesh size, (b) load-deflection diagrams (Bazant, 1992)

As illustrated, the peak load, as well as the post peak softening are strongly dependent on the element size h. Therefore, as h tends to zero the energy dissipated due cracking converges to zero too. In order to solve this setback, it was found that fracture energy must localize into a band of a single element width, in order energy dissipation to be independent from element subdivision. In Plaxis FE software, the smeared crack concept is adopted. Therefore, it uses normalization with respect to equivalent length of the finite element, *Leq*, in order to avoid mesh dependent numerical results.

Fracture energy in tension is described by the parameter $G_{t,28}$. This parameter governs the linear softening regime in the stress-strain diagram, from the peak tensile strength to the residual (Figure 3.4.6). The value of $G_{t,28}$ can be estimated from stress-strain curves of uniaxial tests. However, these tests are difficult to produce accurate results, as stress concentration associated with testing procedure, is usually inevitable. Usually indirect tests are used, like 4 point bend beam test. Barros & Figueiras (1999) carried out such tests on

notched beams of steel fibre reinforcement and proposed a correlation between fracture energy and fibre content for plain concrete:

$$G_t = (1 + 13.195{W_f}^{1.827})G_{t0} \quad (3.4.4.1)$$

Where G_{t0} is the fracture energy of plain concrete (~0.1 kN/m) and W_f is the fibre percentage in weight.

The compressive fracture energy is described by the parameter $G_{c,28}$. It is the area under the stress-strain diagram, between the peak strain and failure strain (Figure 3.4.5). This parameter describes the capability of concrete to plastically deform before it fails. Large values of G_c mean ductile behavior, while small values lead to a more brittle failure, in smaller strain. In order to realistically define compressive fracture energy, uniaxial compression test results from literature, as well as proposed values from EN-1992-1-1 are taken into account. According to EN-1992-1-1, a value of 3.5 ‰ is proposed for the failure strain. Moreover uniaxial compression lab test results from Van Mier (1984) are taken into account. As illustrated in Figure 3.4.9, failure strain which is assumed to be 84~85% of peak strength corresponds to a strain of ~ 3.5 ‰, which agrees with the failure criterion described by EN-1992-1-1 (2011).

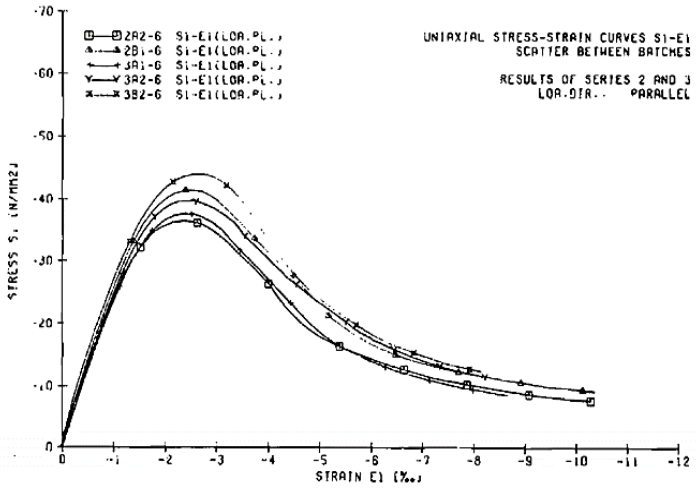

Figure 3.4.9. Stress strain uniaxial compression tests results by Van Mier (1984)

Lastly, taking into account experimental data, Hognestad (1951) developed a numerical expression, which treats the ascending part of the stress-strain diagram as a parabola and the descending as a straight line. This numerical expression is given as:

For $0 < \varepsilon < \varepsilon_0$, $\frac{\sigma}{\sigma_{cu}} = 2\frac{\varepsilon}{\varepsilon_0}\left(1 - \frac{2}{2\varepsilon_0}\right)$ (3.4.4.2a)

For $\varepsilon_0 < \varepsilon < \varepsilon_{cu}$, $\frac{\sigma}{\sigma_{cu}} = 1 - 0.15\left(\frac{\varepsilon - \varepsilon_0}{\varepsilon_{cu} - \varepsilon_0}\right)$ (3.4.4.2b)

Considering all the above, compressive facture energy G_c is fitted such that the stress-strain behavior of the model after peak stress corresponds to lab test results and the aforementioned relations by Hognestad. Taking proposed values for parameters described in the previous paragraph (Table 3.4), the idealized stress strain diagram utilizing the Plaxis element test facility, is illustrated below, together with stress-strain relation proposed by Hognestad (Figures 3.4.10 (a), (b)).

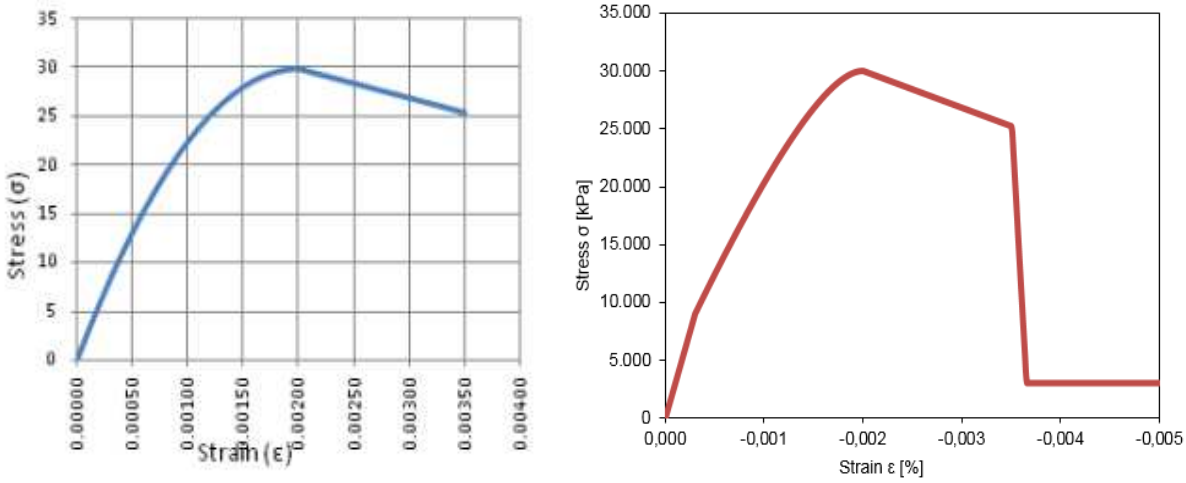

(a) (b)

Figure 3.4.10. (a) Stress-strain diagram as proposed by Hognestad, (b) Idealized stress-strain diagram for Concrete model

Table 3.4: List of initial input parameters

E_{28}	ν	$f_{c,28}$	f_{c0n}	f_{cfn}	f_{cun}	$G_{c,28}$	φ_{max}	ψ	$f_{t,28}$	f_{tun}	$G_{t,28}$	ε_{cp}^{p}
[GPa]	[-]	[MPa]	[-]	[-]	[-]	[kN/m]	[°]	[°]]	[MPa]	[-]	[kN/m]	[-]
30	0.2	30	0.3	0.84	0.1	46	40	5	2	0	0.1	-1‰

3.4.5 Mesh sensitivity of fracture energy parameters

3.4.5.1 Introduction

As mentioned previously, a common problem in numerical simulations is mesh dependency of cracking. In the present study, inspection of mesh dependency of fracture parameters is performed, to avoid unobjective results.

3.4.5.2 Modeling of uniaxial compression tests

In order to inspect the relation between discretization and compressive fracture energy, uniaxial tests in cylindrical and cubic specimens are simulated. For cylindrical specimens the test sample is modeled as a cylindrical volume with slenderness ratio h/d = 2:1. For prismatic specimens the test sample is simulated as a solid cube, of dimensions 100 x 100 x100 mm. Due to symmetry, only one quartile of the cube is modeled. It has to be pointed out that the objective of the numerical simulation of uniaxial compression tests is to investigate whether compressive fracture energy G_c is mesh dependent and not to represent actual conditions of laboratory tests. After modeling the sample, mesh is created. Two meshes with significant difference in coarseness are created for cylindrical and cubic specimens, respectively. Results of stress-strain response are compared for a constant value of G_c, equal to 46 kN/m, as arised from the fitting described in the previous paragraph. Concrete properties are the same as listed in Table 3.4. As compressive fracture energy is related to the ductility of concrete, tests are strain controlled in order to consider softening behavior after reaching peak stress. The prescribed displacement is applied gradually until strength of specimen is exhausted, which can be determined from the descending branch of the stress-strain graph. Figure 3.4.2 shows the stages of the numerical simulation.

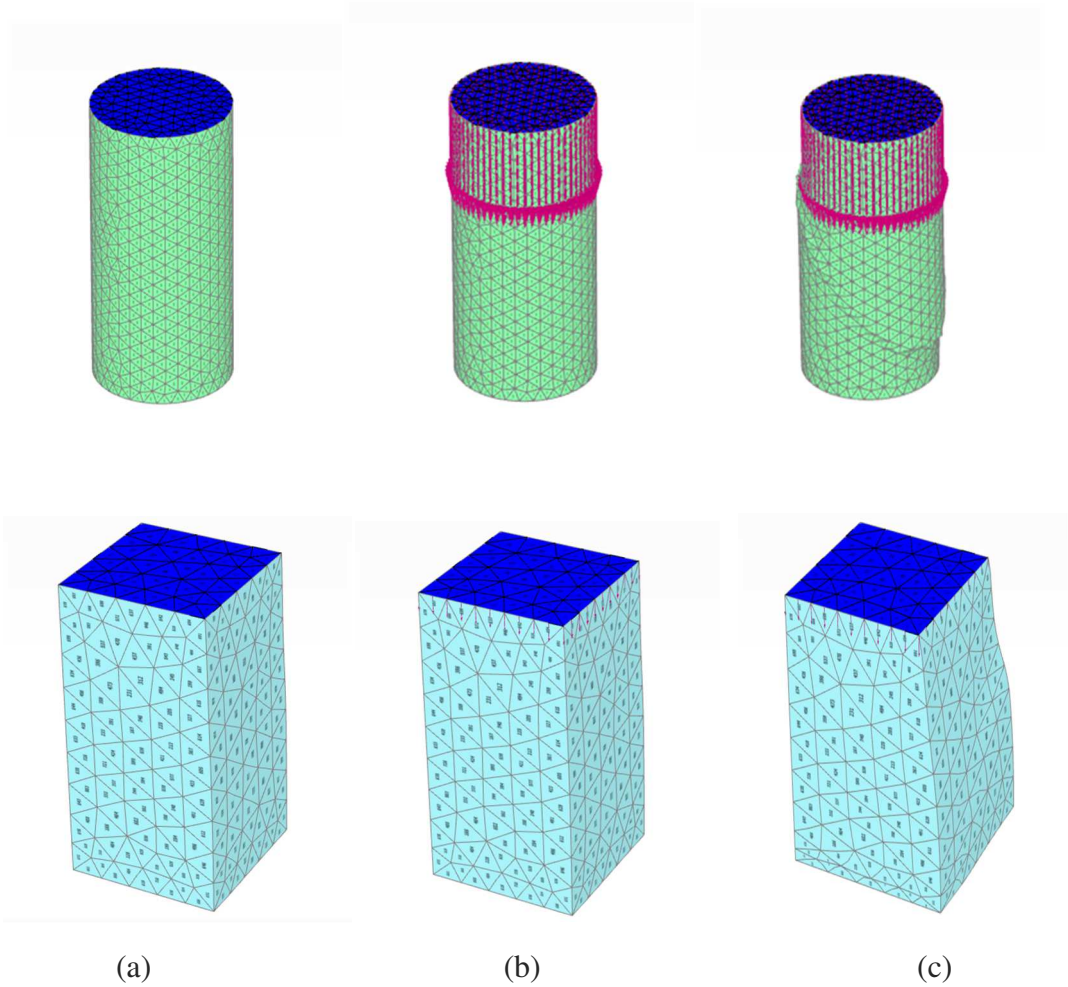

(a) (b) (c)

Figure 3.4.11. (a) Geometry and discretization of the concrete sample, (b) loading of the sample by applying prescribed displacement, (c) deformed mesh at the moment of failure

Results

Results with G_c value kept constant indicate that coarser meshes present a more brittle response. Therefore higher values of compressive fracture energy are required to capture the expected behavior of concrete under uniaxial compression. In Tables 3.5 & 3.6 information about mesh coarseness is given together with the failure strain obtained from the analyses. Figure 3.4.12 presents a comparison of the results for cylindrical and prismatic specimens. From both diagrams one can observe that the pre-peak stress-strain response is independent of average element size. On the contrary the post-peak 'cracked' response is highly dependent on mesh. Furthermore, in Figure 3.4.13 the idealized stress-strain response as fitted to experimental results by Van Mier and relations by Hognestad, is plotted together with stress strain results from simulated uniaxial tests, to show schematically the

independency of mesh coarseness in the pre-peak branch, and the deviations from expected response in the post-peak domain.

Table 3.5: Results for cylindrical specimens

Mesh type	**Nr of Elements**	**Failure strain**
Coarse	822	~ 3.6‰
Very Fine	20396	~ 5.5‰

Table 3.6: Results for cubic specimens

Mesh type	**Nr of Elements**	**Failure strain**
Coarse	858	~3.7 ‰
Very Fine	39205	~ 4.25‰

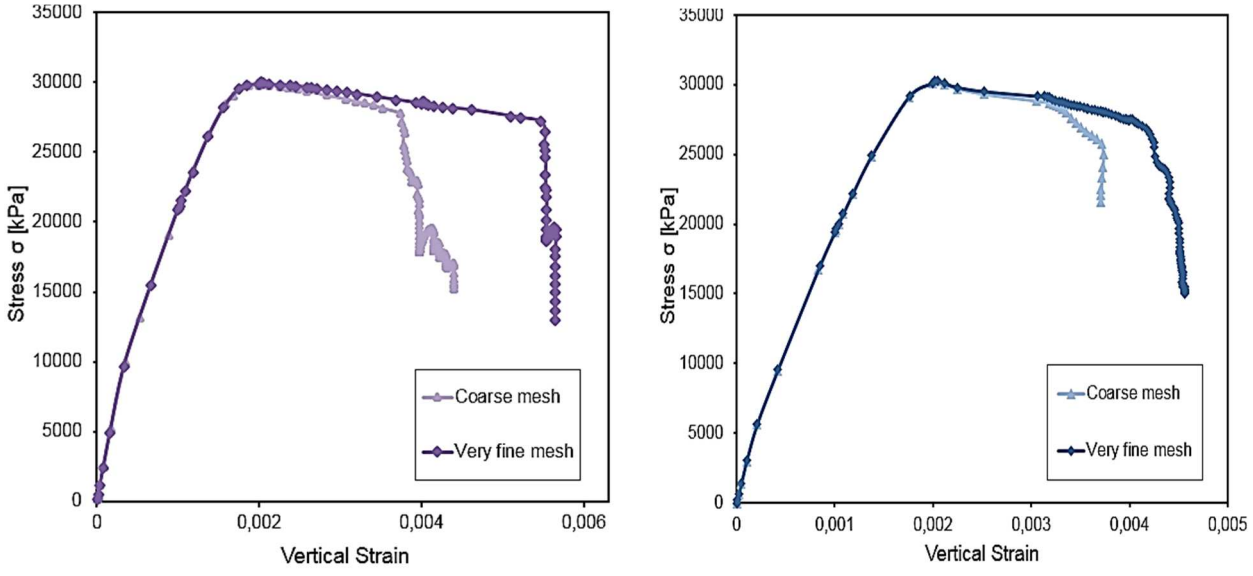

(a) (b)

Figure 3.4.12. Comparison of stress-strain response from uniaxial tests (a) in cylinders, (b) in cubic samples

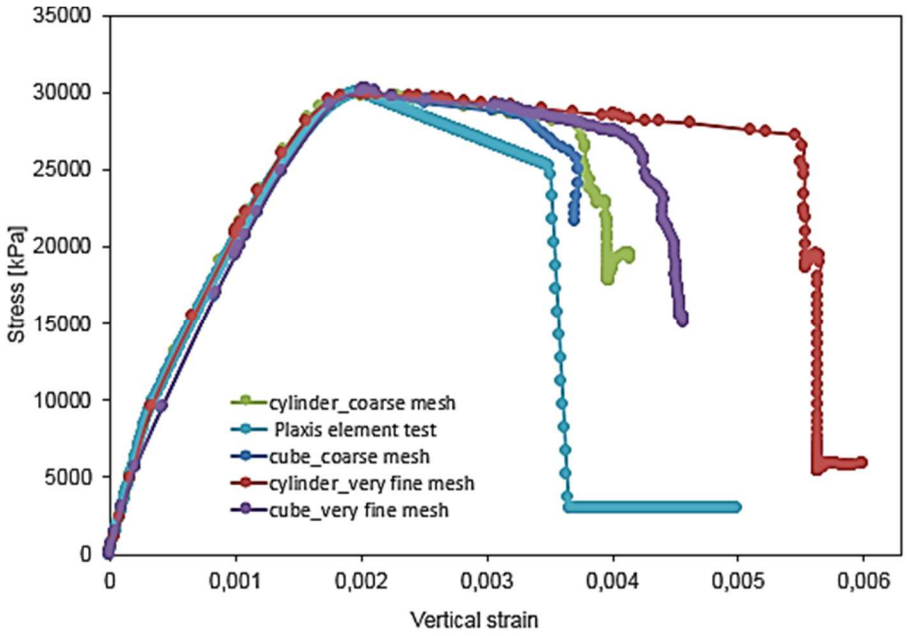

Figure 3.4.13. Comparison between response from modeled uniaxial compressive tests in cubic and cylindrical samples, and idealized stress-strain curve from Plaxis element test

Additionally, not only quantitative difference in failure conditions is observed, but also qualitative. In coarse meshes failure surfaces are vague and wider than fine meshes. For the cylindrical samples modeled, different types of failure correspond to different mesh sizes, as illustrated in Figure 3.4.14. Therefore in cases where cracking pattern and failure type really matters, values of compressive fracture energy should be optimized.

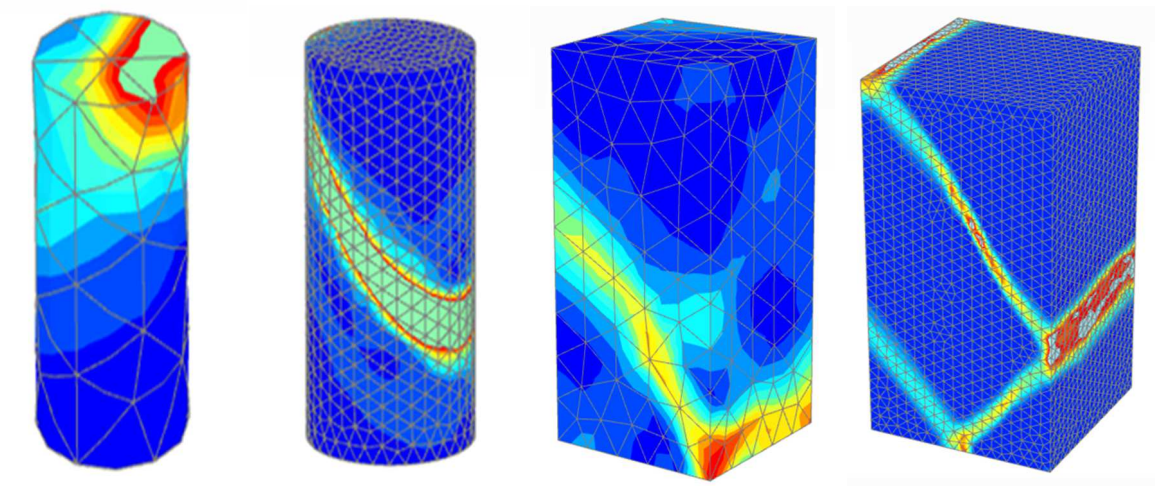

(a) (b) (c) (d)

Figure 3.4.14. Comparison of failure modes (a) coarse mesh, side fractures , (b) fine mesh-diagonal fracture (c) coarse mesh, wide and vague failure surface, (d) fine mesh discrete failure surface

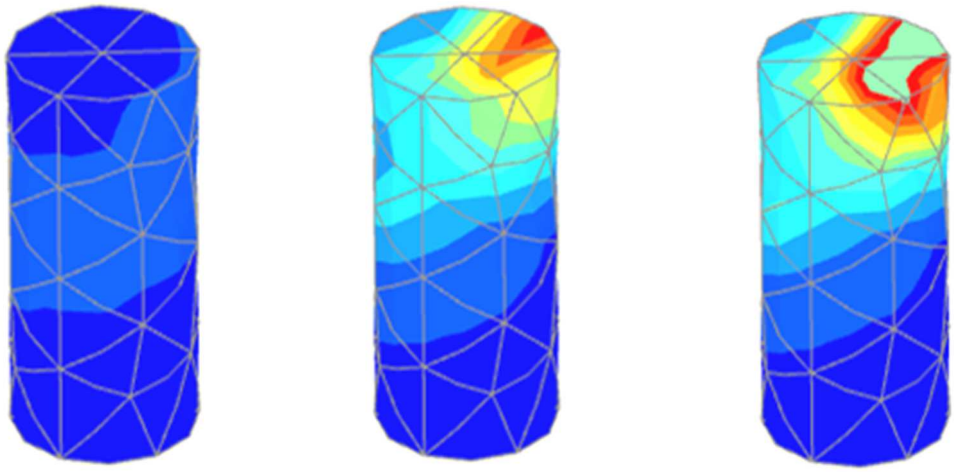

(a)

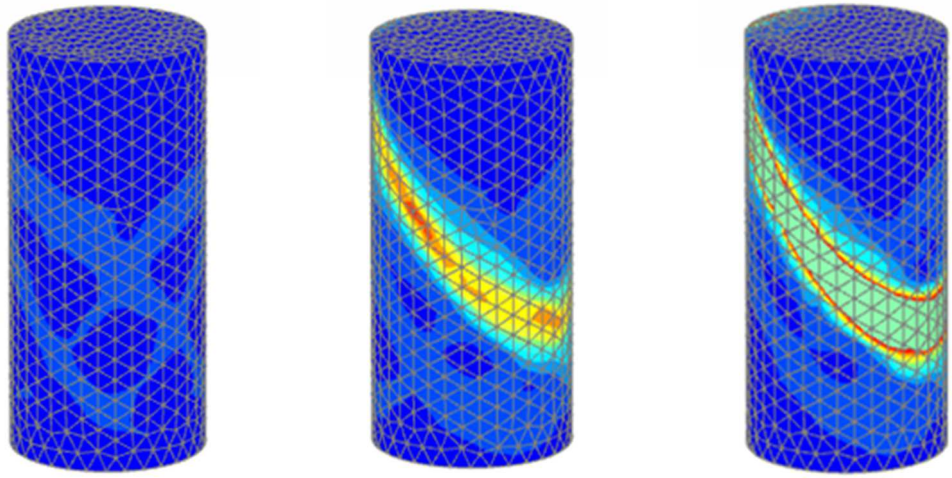

(b)

Figure 3.4.15 Evolution of failure mechanism for cylindrical samples (a) coarse mesh, (b) fine mesh

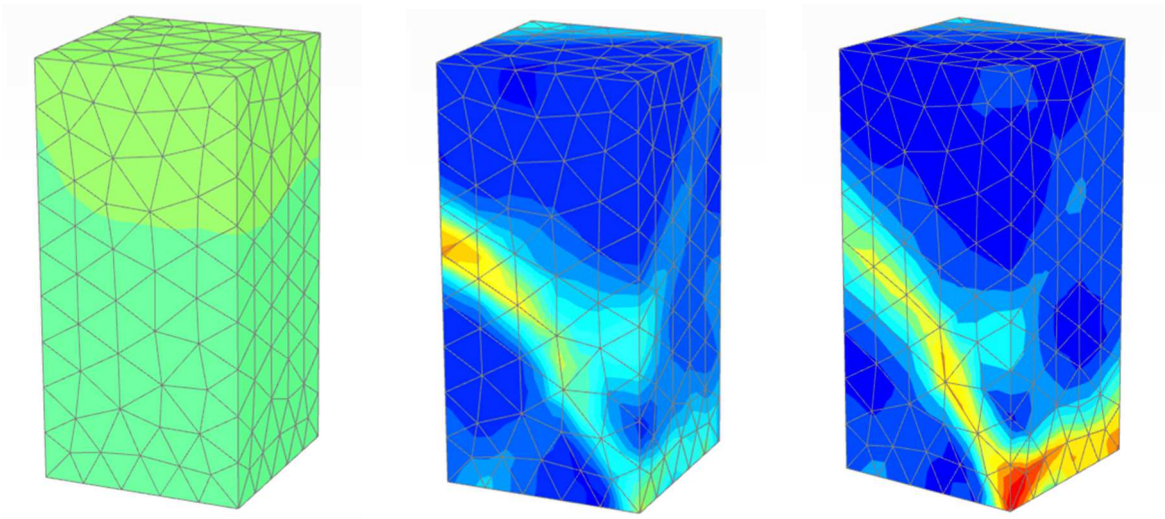

(a)

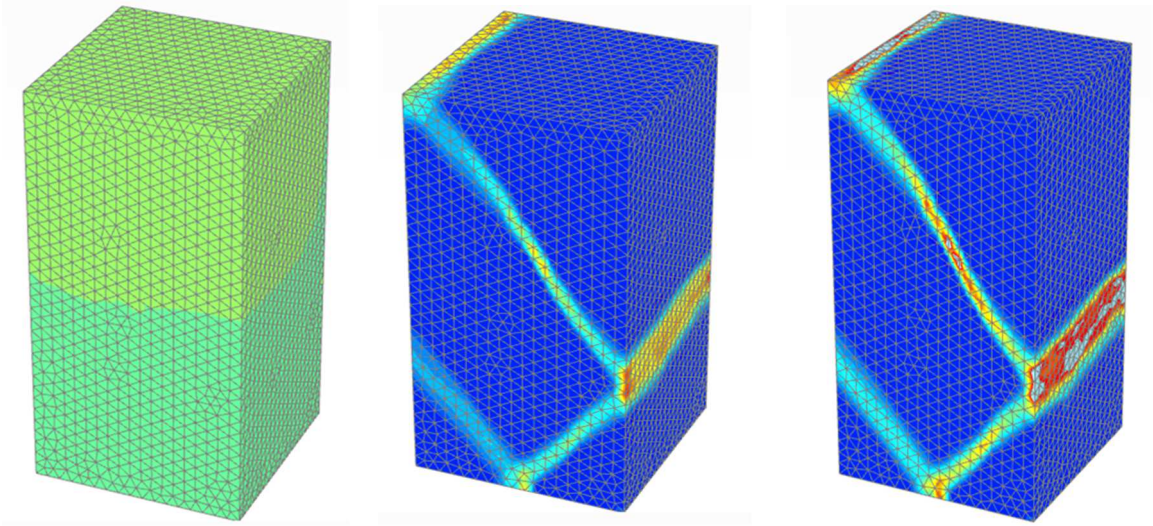

(b)

Figure 3.4.16. Evolution of failure mechanism for prisms (a) coarse mesh, (b) fine mesh

3.4.5.3 Modeling of simple uniaxial tensile tests

In order to investigate whether tensile fracture energy G_t is mesh dependent or not, a rough numerical simulation of a direct tensile test is modeled. Again, the objective is only to understand the relation between element size and tensile fracture energy and not to represent actual procedures and laboratory conditions. Cylindrical specimens, as in uniaxial compression tests, of slenderness ratio h/d = 2:1 are modeled. Two meshes with significant difference in coarseness are created and results of load-deformation response are compared for a constant value of G_t , equal to 0.1 kN/m. All input values of concrete properties are listed in Table 3.7 below. As tensile fracture energy represents the area below the softening branch of load-deformation response, tests are displacement controlled. The prescribed displacement is applied gradually until failure of the specimen. The stages of the simulation are illustrated in Figure 3.4.17, below.

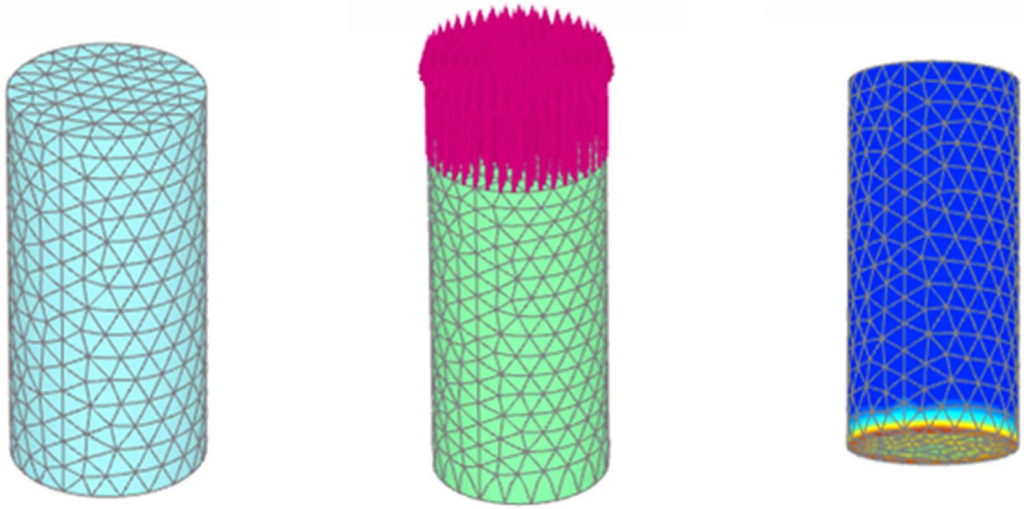

(a) (b) (c)

Figure 3.4.mier17. (a) Finite element model of the concrete sample, (b) loading of the sample by applying prescribed displacement, (c) failure state

Table 3.7: Concrete material parameters

E_{28}	ν	$f_{c,28}$	f_{c0n}	f_{cfn}	f_{cun}	$G_{c,28}$	φ_{max}	ψ	$f_{t,28}$	f_{tun}	$G_{t,28}$	ε_{cp}^{p}
[GPa]	[-]	[MPa]	[-]	[-]	[-]	[kN/m]	[°]	[°]	[MPa]	[-]	[kN/m]	[-]
30	0.2	30	0.3	0.84	0.1	46	40	5	3	0	0.1	-1‰

Results

Results from analyses for the two meshes are given in Figure 3.4.19 and Table 3.8. As indicated on the load-deformation diagram below, the peak load, as well as the post peak response are significantly affected by the element size, while the pre-peak branch is the same for both meshes. The shape of the diagram resembles remarkably the diagram from the example of the loaded panel (see Fig. 3.4.8). As average element size decreases, energy dissipated due cracking decreases too. Therefore, it seems that tensile fracture energy G_t is affected by mesh coarseness too.

Table 3.8: Comparison of results for different mesh sizes

Mesh type	Nr of Elements	Deformation at failure [mm]	Maximum Load [kN]
Coarse	822	0.252	2988
Very Fine	12449	0.188	2215

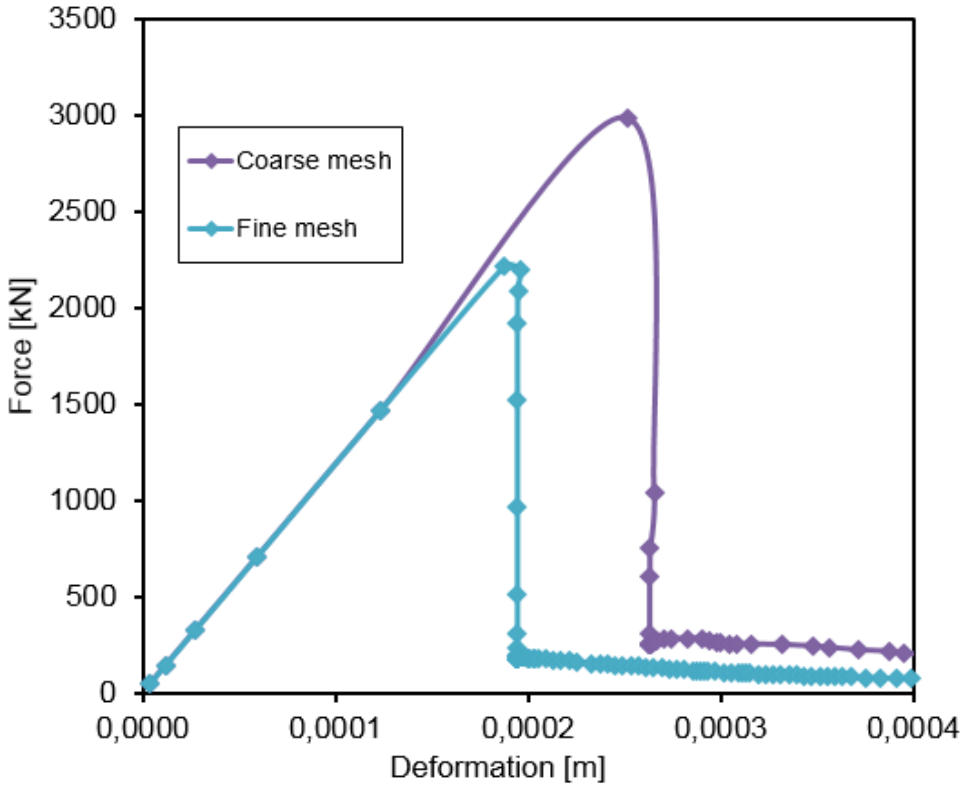

Figure 3.4.18 Comparison of force-deformation response from uniaxial tensile tests at constant $G_t = 0.1kN/m$

4 Pushover analysis of a reinforced concrete column

4.1 General model setup

The three phenomenological constitutive relations described in the previous chapter are implemented in numerical simulations to model reinforced concrete material. Their performance is investigated though nonlinear pushover analyses of a circular reinforced concrete column. The column is modeled as a 3D soil volume element of 16 m length and 1 m diameter. A total displacement fixity is placed at the bottom and a stress distribution or a uniform prescribed displacement, depending on the constitutive model, is applied on top. Moreover a plate element of high rigity is placed to act as a diaphragm. Afterwards the model is divided into a finite element mesh and incrementally increased lateral load is applied until failure of the system. For each approach, a further description of the model, input values, calibration procedure of critical parameters and computed results, are given in the next paragraphs.

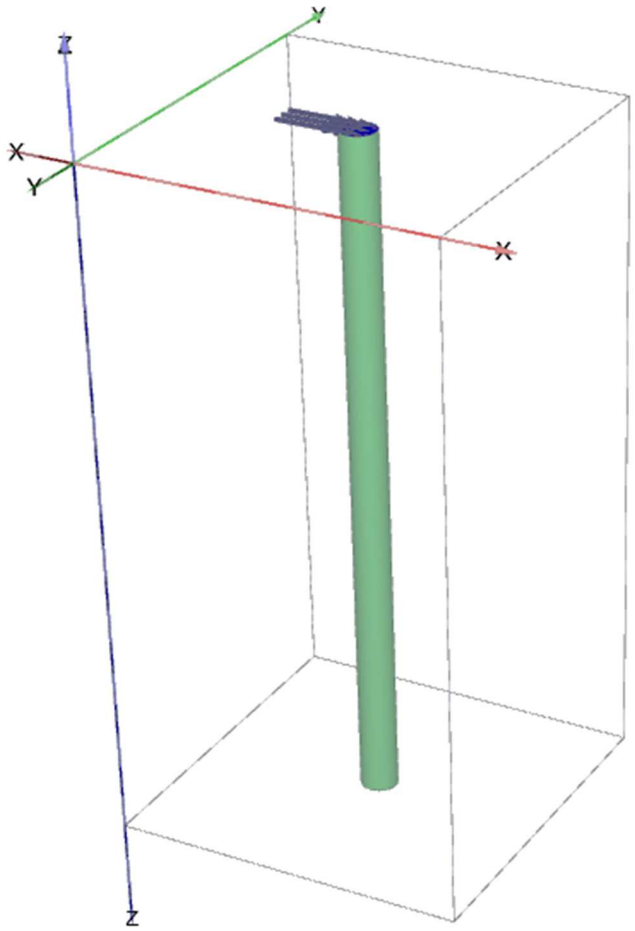

Figure 4.1.1. Geometry of the model

4.2 Detailed Mohr-Coulomb based model

In this first modeling approach concrete material is described by Mohr-Coulomb failure criterion and it is combined with elastoplastic structural elements. A 3D view of the layout of reinforcement bars and a detailed cross-section, considering longitudinal reinforcement ratio As=2%, are displayed in Figure 4.2.2 below. The Mohr-Coulomb model with tension cut off was proposed by Chen & Han (1988), and in order to describe the behavior of concrete material, only 5 input parameters are required. It is defined in terms of c and φ, directly derived from f_c and f_t (concrete compressive and tensile strength) as follows :

$$\varphi = \sin^{-1}\left(\frac{f_c - f_t}{f_c + f_t}\right) \tag{4.2.1}$$

$$c = \frac{1 - \sin\varphi}{2\cos\varphi} f_c \tag{4.2.2}$$

By replacing with f_c = 30 MPa and f_t =2 MPa, the values for c and φ are extracted :

$c = 3879\ kPa, \varphi = 61°$

In addition it requires two elastic parameters: modulus of elasticity E and Poisson's ratio v. Assuming concrete of class C30/37 modulus of elasticity is taken equal to 30 GPa and Poisson's ratio equal to 0.2 . For this case, tension cutoff is considered zero.

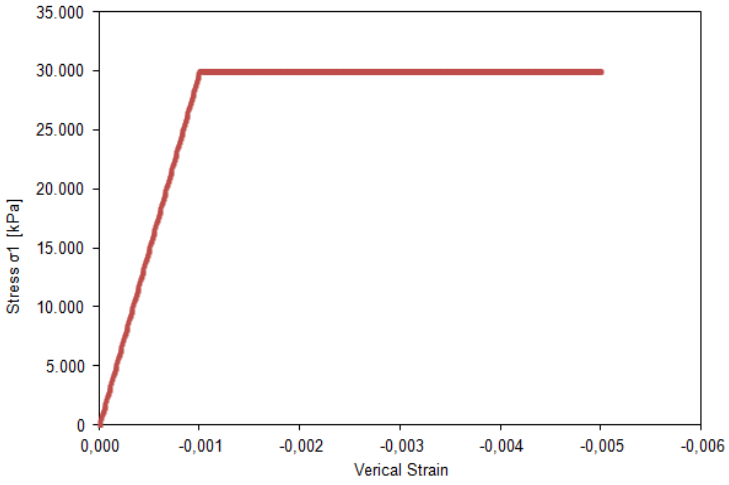

Figure 4.2.1. Stress-strain response of the Mohr-Coulomb model from Plaxis element test module

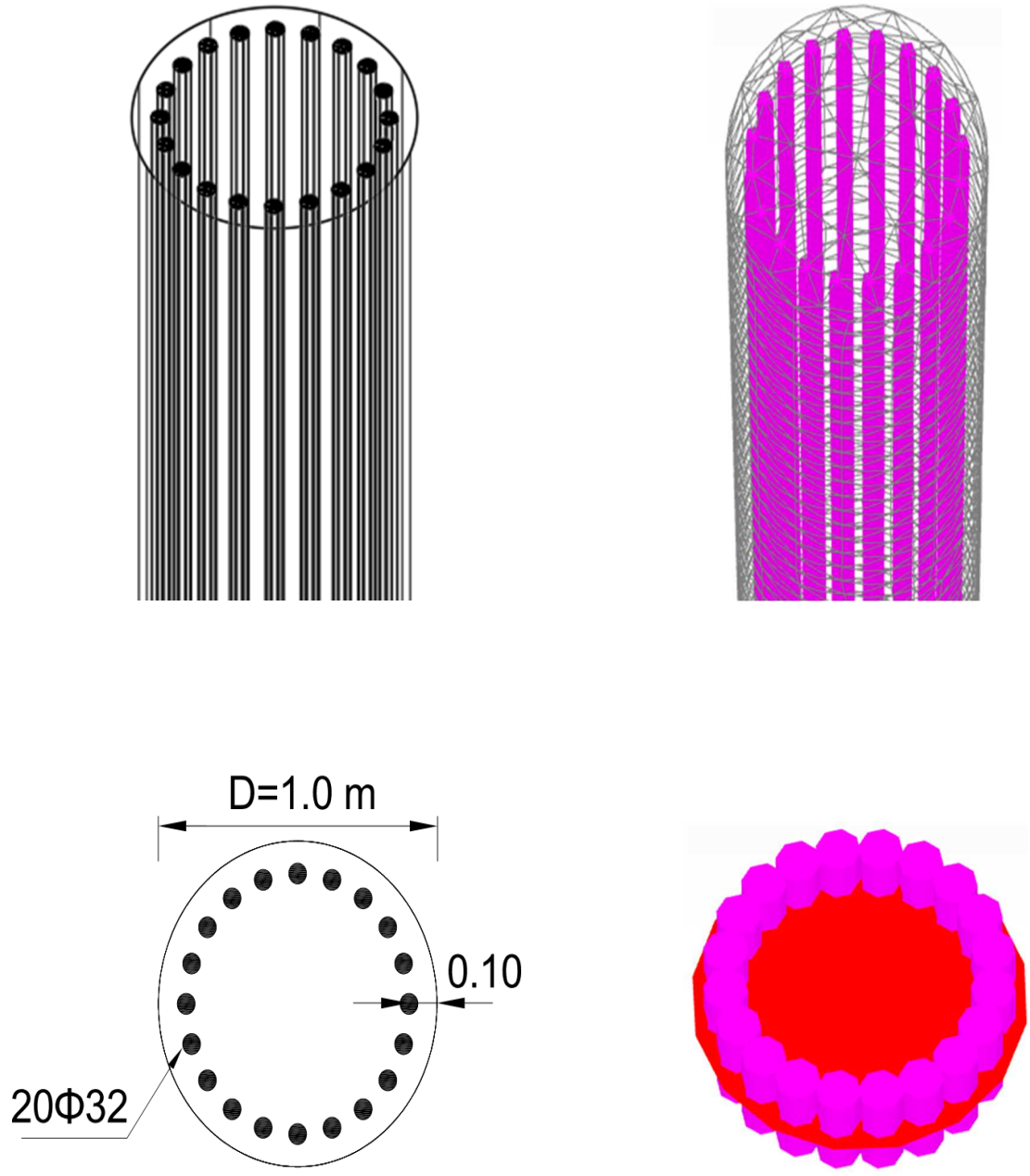

(a) *(b)*

Figure 4.2.2 (a) 3D visualization and 2D cross-section detail of reinforcement bars (b) Numerical simulation of reinforcement with structural elements in Plaxis 3D

4.2.1 Modeling of reinforcement

In this model detailed reinforcement, as shown in Figure 4.4.2 needs to be incorporated. In the present study, two options for modeling reinforcement are investigated. The first option is the incorporation of embedded beam elements. Embedded beams are structural elements commonly used to model axially loaded piles. They include interface elements in order to be able to describe pile-soil interaction. As a result, theoretically, they could be used to simulate more accurately reinforcement of a concrete element, as bond stress between concrete and steel can be quantified, with the skin resistance t_{skin} (kN/m). For our case t_{skin} is calculated as follows :

$$t_{skin} = \pi \, \emptyset \, 2{,}25 \, f_{td} \qquad (4.2.1.1)$$

In the analyses first elastoplastic embedded beams with a diameter of 32 mm are modeled. From Eq. (4.2.1.1) above, tskin is calculated equal to 452 kN/m. Initial input parameters of elastoplastic embedded beams are listed in Table 4.1 below:

Table 4.1: Initial input for elastoplastic embedded beams

E	ν	γ	D	σy	t_{skin}
[GPa]	[-]	[kN/m^3]	[m]	[MPa]	[kN/m]
200	0.2	0.001	0.032	500	452

Results with embedded beam elements

Firstly 20 elastoplastic embedded beams are used, for longitudinal reinforcement ratio As=2% . Pushover analysis is force controlled and the load is applied as a uniform lateral distributed stress. The computed results are initially compared with those extracted from the reference models USC_RC and Response-2000, which are implemented for the analysis of strength and ductility of reinforced concrete structures. At first, for modulus of elasticity of concrete material E = 30 GPa, results from numerical analysis showed a much stiffer response in load-deformation terms. By trial and error, with reducing each time the modulus of elasticity, arised that approximately a 30% reduction of the modulus of elasticity was necessary in order the results to be at least comparable to the proposed fit. Moreover reduction of skin resistance did not seem to affect the results, as for a reduction of tskin to

50% and consequently to 5% of its initial calculated value, the response was quite similar (Figure 4.2.3). Due to these setbacks, the solution of 3D beams is adopted. Nevertheless, the performance of embedded beams under lateral loading conditions should be further investigated, something that could not be done thoroughly in the present study, due to the limited time available.

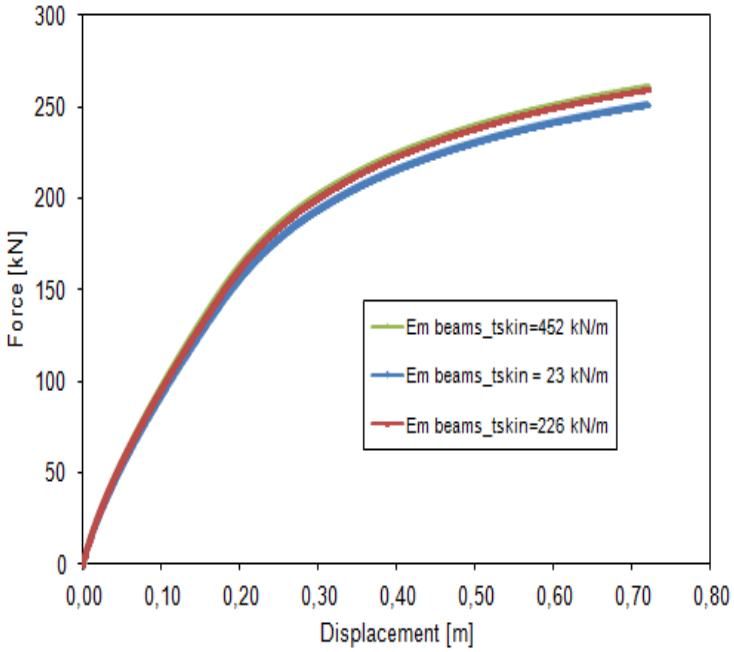

Figure 4.2.3. Comparison of pushover analyses results with different skin resistance (tskin) values

Results with beam elements

In this setup, at first 20 elastic beams with a diameter of 32 mm are used, for longitudinal reinforcement ratio As=2%. Again, force controlled type of analysis is chosen and the load is applied as a uniform lateral distributed stress. Then the procedure is repeated with the use of elastoplastic beams of yield stress f_y = 500 MPa. Results of the load - displacement response showed that 3D beam elements are functional, as for a prescribed displacement of 1.0 meter the use of elastic beams leads to a linear response, while the use of elastoplastic beams leads to yielding (Figure 4.2.4a). Moreover overall response, with the use of elastoplastic beams, is comparable with our reference models (Figure 4.2.4b). By evaluating the above results 3D elastoplastic beams seem to realistically simulate the behavior of structural reinforcement and therefore are used in all the following analyses.

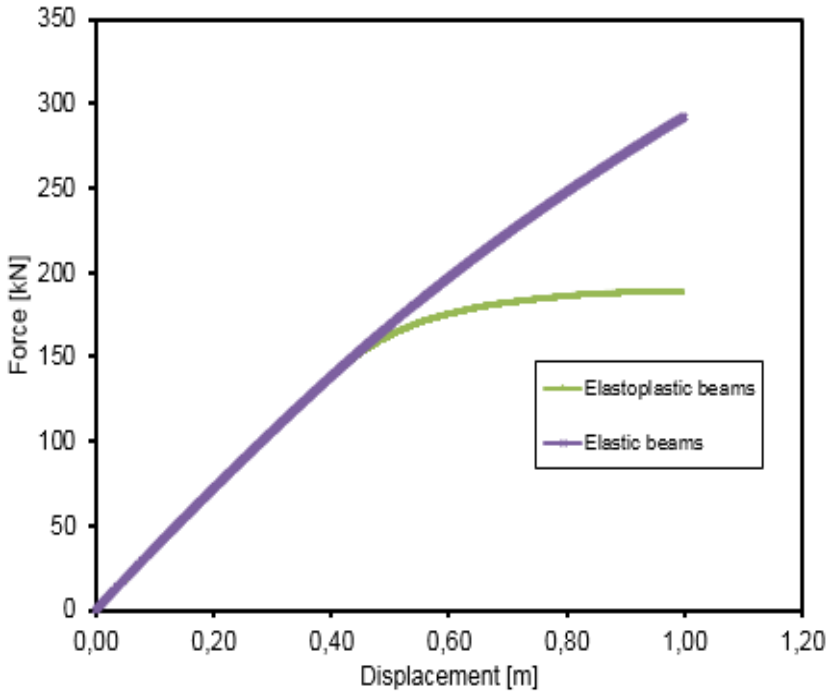

(a)

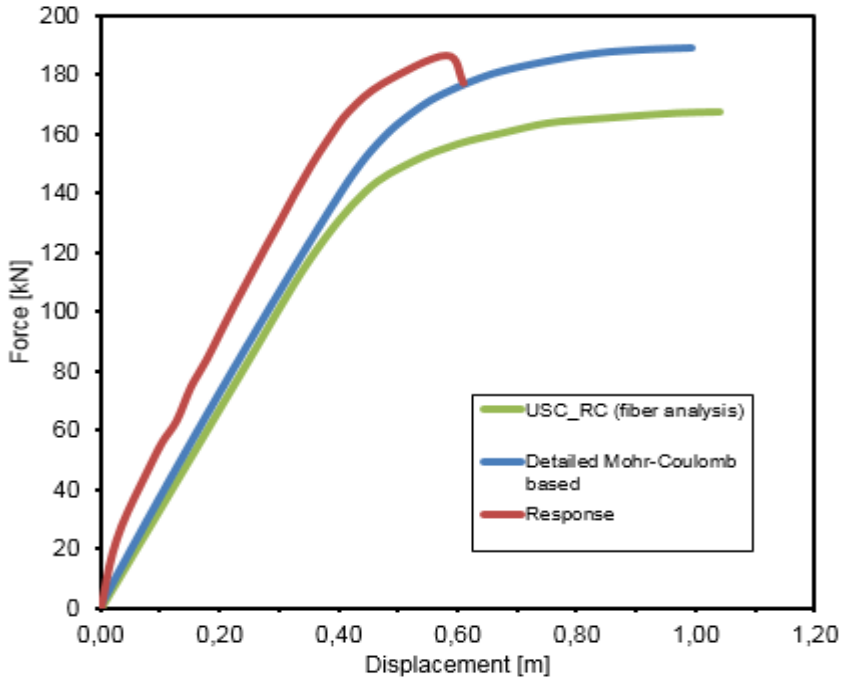

(b)

Figure 4.2.4. (a) Comparison of load-deflection response from Plaxis code with elastic and elastoplastic 3D beam elements, (b) Comparison of load-deflection response from Plaxis code and reference models

4.3 Detailed Concrete based model

For this modeling Plaxis Concrete constitutive model is combined with detailed reinforcement. As for Mohr-Coulomb based model elastoplastic beam elements are used to simulate reinforcement bars, and Concrete model is applied to the volume pile. The geometry of the model and the layout of reinforcement is as illustrated in Figures 4.1.1 and 4.2.2. For this approach, displacement controlled analysis is chosen, to capture the post-yielding behavior until rupture. Time independent input parameters required, to describe nonlinear behavior of concrete material, are described in detail in chapter 3. All strength and strain parameters required can be directly defined from literature according to laboratory results, verified expressions based on experimental data or codes. These parameters, together with their values used in the following analyses are listed in Table 4.2, below. On the contrary parameters related to fracture energy cannot be directly defined, as according to what was proven in chapter 3, they are sensitive to mesh coarseness. Analyses without calibration of these parameters could lead to false estimation of ductility of concrete material and consequently result in a nonrealistic overall response of the member. It seems that in order to succeed accuracy of results, for each mesh created, optimum values for fracture energy parameters should be found. In the present case, a calibration procedure for compressive fracture energy G_c is performed. As reinforced concrete elements are modeled, reinforcement is used to take up the tensile stresses after concrete cracks. Tensile strength of concrete, in RC structures provides a small increase in the initial stiffness of a force-displacement curve, without vitally affecting the total strength. Therefore tensile fracture energy G_t is taken equal to 0.1 kN/m as Plaxis proposes. However for problems that tensile strength of concrete is an important factor, tensile fracture energy should be calibrated.

Table 4.2: Concrete parameters used for the analyses

E_{28}	ν	$f_{c,28}$	f_{c0n}	f_{cfn}	f_{cun}	φ_{max}	ψ	$f_{t,28}$	f_{tun}	$G_{t,28}$	ε_{cp}^{p}
[GPa]	[-]	[MPa]	[-]	[-]	[-]	[°]	[°]	[MPa]	[-]	[kN/m]	[-]
30	0.2	30	0.3	0.84	0.1	40	5	2	0	0.1	-1‰

4.3.1 Model calibration

Calibration of compressive fracture energy G_c is succeeded by fitting the stress-strain response of the model with curves from literature. As it determines the strain occurring between the peak and the failure strength, only the post peak response requires to be fitted. Tests by Van Mier (1984), proposed values from EN-1992 and equations proposed by Hognestad, as mentioned above, are utilized. The main objective is to achieve failure strength at strain equal to 3.5 ‰.

Procedure and results

As in Chapter 3, uniaxial compression tests are performed, but for the full scale model. The objective is to find the relation between number of elements and compressive fracture energy in order the aforementioned failure criterion to be satisfied. A cylinder with slenderness ratio of h/d = 16:1 with 3D beams is modeled, as existence of beams affects discretization, and then beams are deactivated for the analysis. A fine mesh, consisting of 43479 elements is created and then, prescribed displacement is applied stepwise until failure. Initially, a value of G_c equal to 46 kN/m is considered (as calculated from the area under peak and failure strength of the idealized stress-strain response (see Figure 3.4.5). The 'specimen' failed at a strain equal to 2.67 ‰ indicating that a higher value of G_c is required for this specific mesh. Analyses with different G_c resulted in an optimum value, equal to 100 kN/m. This value is adopted for the pushover analyses of the reinforced concrete column that follows. Results are shown in Figure 4.3.2.

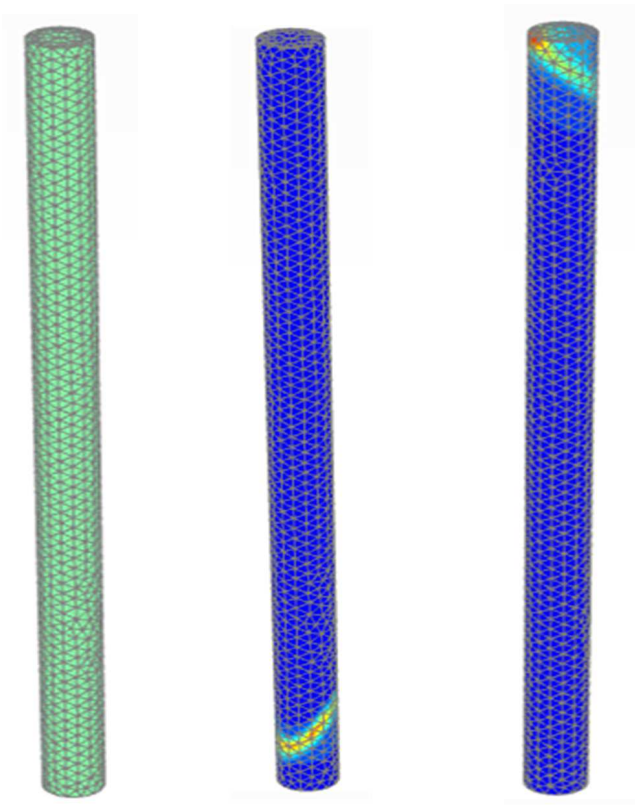

Figure 4.3.1. Discretization of the column element and deviatoric strain γs at failure for two different values of G_c

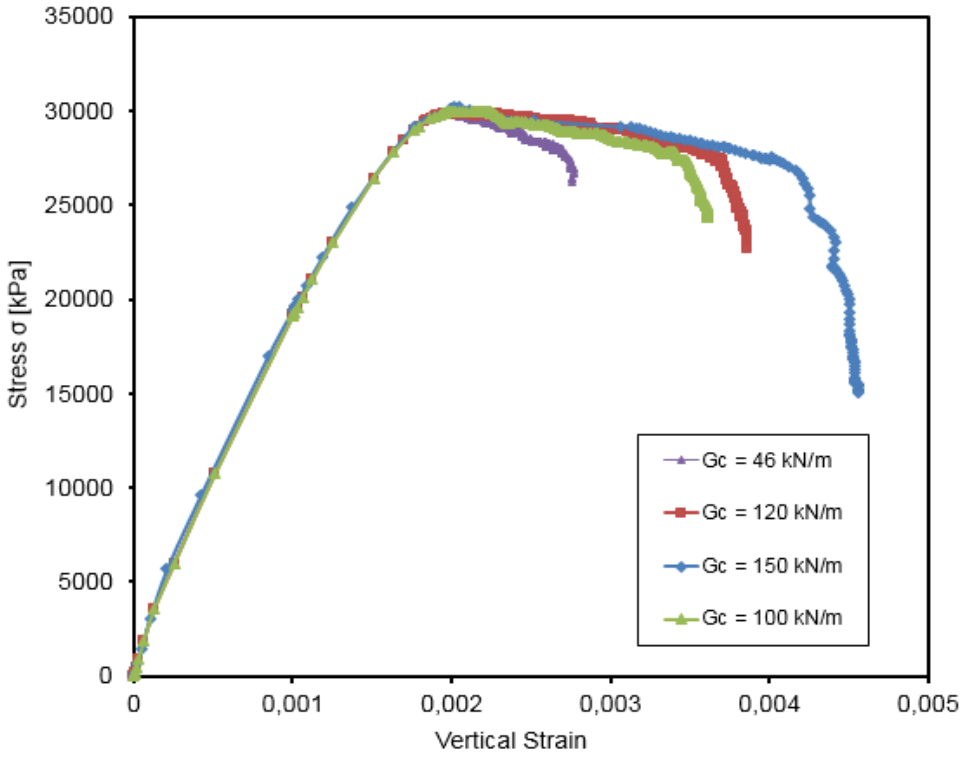

Figure 4.3.2. Stress-strain curves obtained for different values of compressive fracture energy

4.3.2 Pushover analyses results

At first two analyses are carried out. For the first analysis, concrete material is defined by the parameters as described in the previous paragraph, in order to approach its real behavior. For the second analysis tensile strength, and tensile fracture energy of concrete are set equal to zero and parameters affecting strain hardening and softening in compression are set equal unity. Values of input parameters for the two analyses are given in Tables 4.4 & 4.5.

Table 4.3: Input parameters for numerical simulation of real behavior of concrete

E_{28}	ν	$f_{c,28}$	f_{c0n}	f_{cfn}	f_{cun}	$G_{c,28}$	φ_{max}	ψ	$f_{t,28}$	f_{tun}	$G_{t,28}$	ε_{cp}^{p}
[GPa]	[-]	[MPa]	[-]	[-]	[-]	[kN/m]	[°]	[°]	[MPa]	[-]	[kN/m]	[-]
30	0.2	30	0.3	0.84	0.1	100	40	5	2	0	0.1	-1‰

Table 4.4: Input parameters considering linear elastic - perfectly plastic behavior, without tensile strength

E_{28}	ν	$f_{c,28}$	f_{c0n}	f_{cfn}	f_{cun}	$G_{c,28}$	φ_{max}	ψ	$f_{t,28}$	f_{tun}	$G_{t,28}$	ε_{cp}^{p}
[GPa]	[-]	[MPa]	[-]	[-]	[-]	[kN/m]	[°]	[°]	[MPa]	[-]	[kN/m]	[-]
30	0.2	30	1	1	1	100	40	5	0	0	0	-1‰

The second analysis has a double aim. The first is to compare results with the previous linear elastic-perfectly plastic Mohr-Coulomb based approach, and the second to investigate how tensile strength affects overall response. Plaxis element test facility is used to get an insight in the behavior of the models. Comparison of stress-strain curves extracted from Plaxis element test facility, for Detailed Mohr-Coulomb based approach and Detailed Concrete based model considering perfect elastoplasticity and zero tensile strength, is illustrated in Figure 4.3.3 below. It is observed that stress-strain response is exactly the same. Because of this compliance the results of the pushover analysis are expected to be similar. Full member's response results are illustrated in Figures 4.3.4 and 4.3.5.

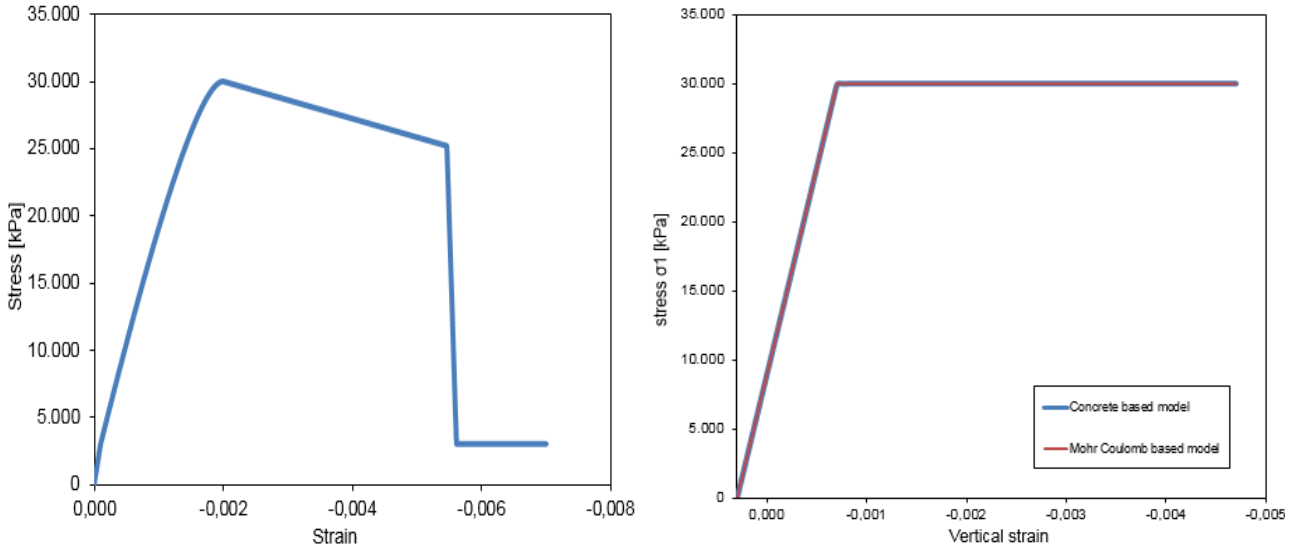

(a) (b)

Figure 4.3.3. (a) Stress-strain response of Detailed Concrete based model with proposed parameters (b) Comparison of stress-strain response from Detailed Mohr-Coulomb and Concrete based models considering linear elastic-perfectly plastic behavior and zero tensile strength

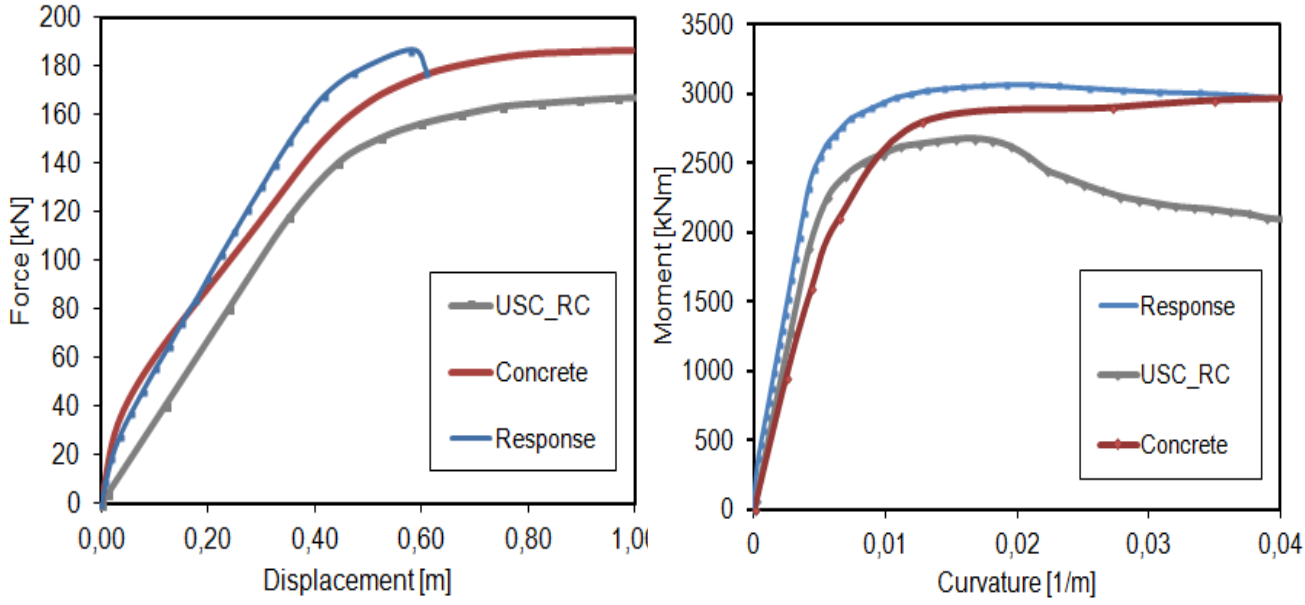

(a) (b)

Figure 4.3.4. Comparison of results from Plaxis 3D code with Detailed Concrete based model and reference models (a) load-deflection response (b) moment-curvature response

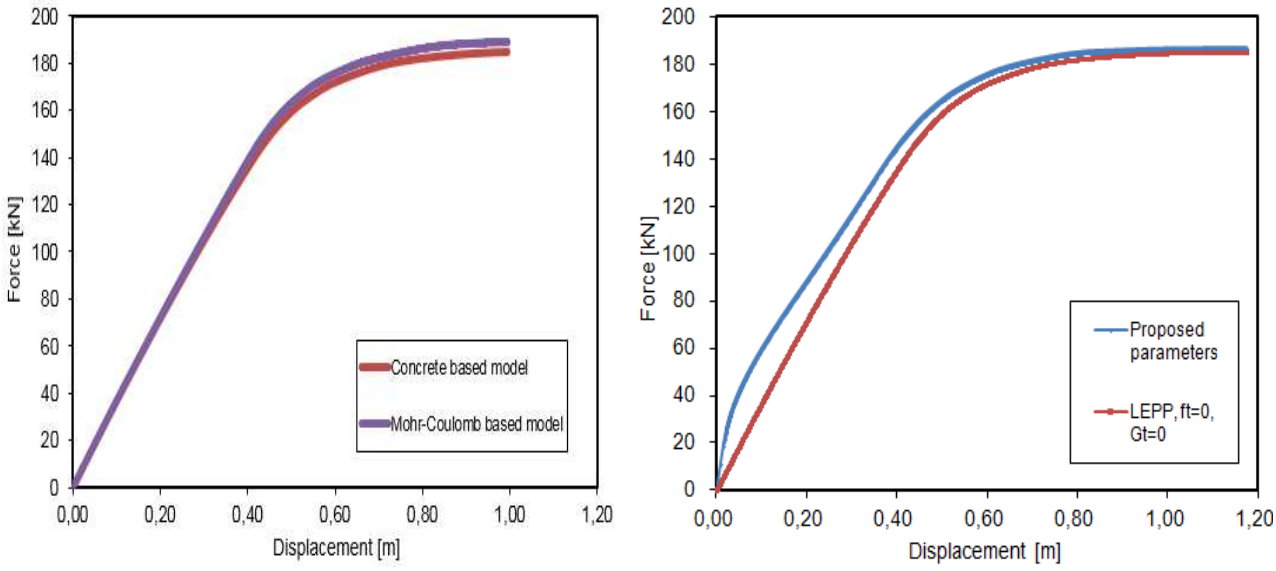

(a) (b)

Figure 4.3.5. Comparison of load-deflection response from (a) Detailed Mohr-Coulomb and Concrete based models considering perfect elastoplasticity and zero tensile strength, (b) Comparison of Concrete based models response considering proposed parameters and parameters assuming perfect elastoplasticity and zero tensile strength

Figure 4.3.4 (a) illustrates the results of force-deflection responses from the pushover analysis in Plaxis and from reference models, Response and USC_RC. Concrete based model and Response present similar results until a load of 80 kN and they reach almost exactly the same maximum load with insignificant deviation, equal to 0.05%. However Response presents a more brittle failure. Compared to fiber analysis Concrete based model has a stiffer response, and a difference in shape is observed in the initial 'uncracked' part due to the tensile strength of Concrete model. The deviation between the maximum loads is higher and equal to 11%. In Figure 4.3.5 (a), results from the analysis of the Detailed Mohr-Coulomb based model are plotted together with results from the second analysis using Plaxis Concrete model, with the assumption of perfect elastoplasticity, without tensile strength. The response is almost the same, with a slight deviation in the last part of the diagrams, in the region where plastic deformations are generated. Deviation of the maximum loads is equal to 2.05%. In order to understand this change, given that the two models have the same single stress point response, as it is indicated in Figure 4.3.3 (b), a closer look on failure mode should be taken.

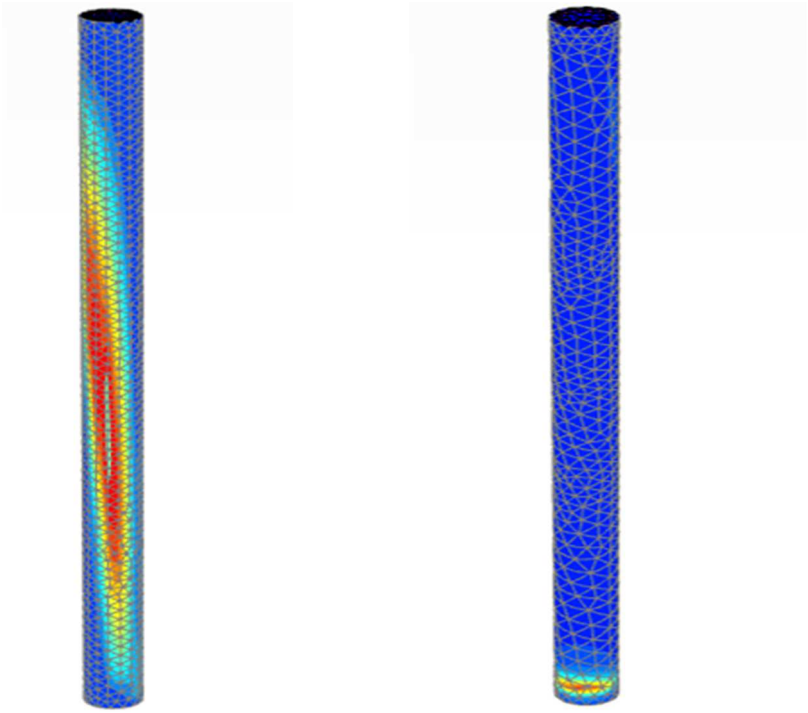

(a) (b)

Figure 4.3.6. Comparison of failure modes: (a) from analysis with Concrete based model (b) from analysis with Mohr-Coulomb based model

Figure 4.3.6 above depicts the different failure mechanism for each analysis. In analysis with detailed Concrete based model shear failure due to zero tensile strength is observed, while in the analysis with detailed Mohr-Coulomb based model, a plastic hinge is developed at the bottom of the pile. Therefore, it seems that Concrete model captures the behavior of concrete material at failure state more realistically.

Figure 4.3.5 (b) illustrates the effect of tensile strength properties in the total response of the column. Tensile strength increases stiffness before yielding, with no significant contribution to the total strength. However as it is shown in Figure 4.3.7 below, it plays a major role for the failure mode of the column. For concrete with tensile strength flexural cracks can be visualized (at the side of tension), whether for concrete without tensile strength the failure mode has changed from flexure to shear.

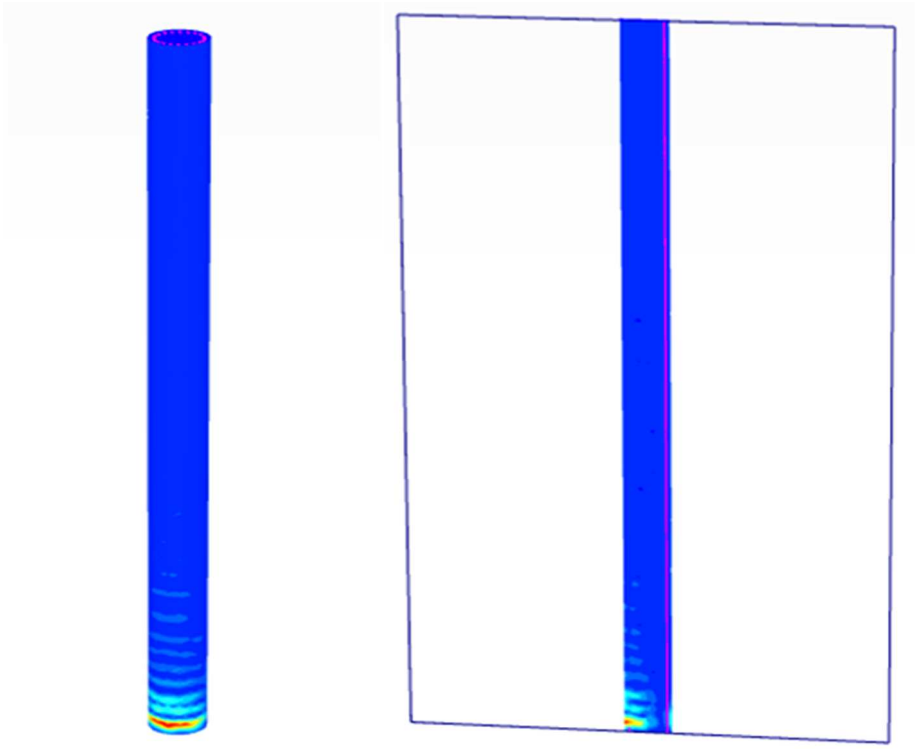

Figure 4.3.7. Flexural cracks at failure for Detailed Concrete based model with tensile strength, 3D visualization and vertical cross - section

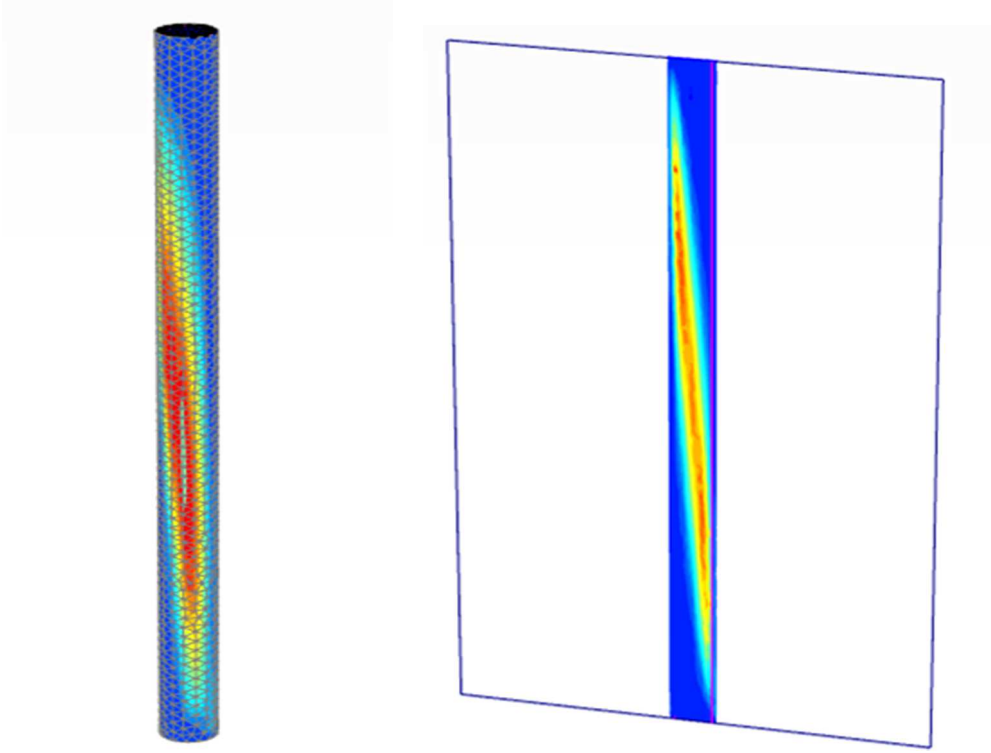

Figure 4.3.8. Shear failure for Detailed Concrete based model with zero tensile strength, 3D visualization and vertical cross - section

A last observation, concerns the form of the load-deflection behavior of Concrete based model, considering tensile strength properties. As it illustrated in Figure 4.3.9 below, three parts can be distinguished. The first is a linear elastic part of high stiffness until cracking. The second is an almost linear domain with reduced stiffness and the third is the part after yielding with even more reduced stiffness, where plastic deformations increase until failure. Similar form of the response is obtained also from analyses for longitudinal reinforcement ratio equal to As = 1%. The same observations were noted by Maatkamp (2016), regarding results from Plaxis Shotcrete model in 2D analyses.

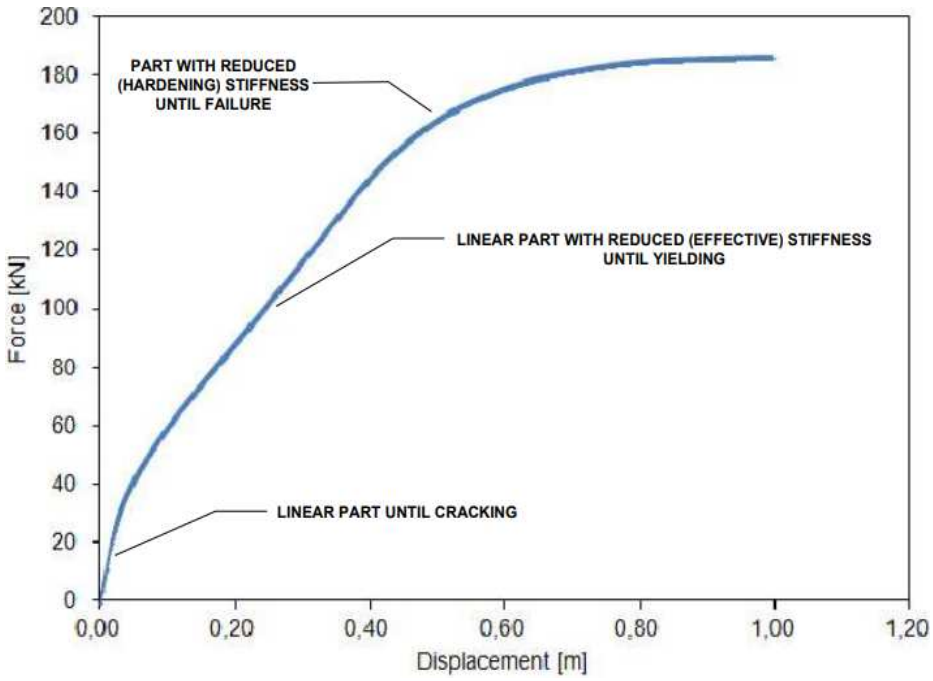

Figure 4.3.9. Detailed Concrete based model: Parts of load-deformation response

Figure 4.3.10 illustrates the distribution of plastic and tension cut-off points as well as normal stresses for the Detailed Mohr-Coulomb and Concrete based models, with proposed parameters for Concrete material model. Indicatively, a cross-section at the critical zone is chosen at the base of the column (-16m). More tension cut-off points are observed for detailed Mohr-Coulomb based model compared to Concrete based, as it is expected due to the zero tensile strength assumption.

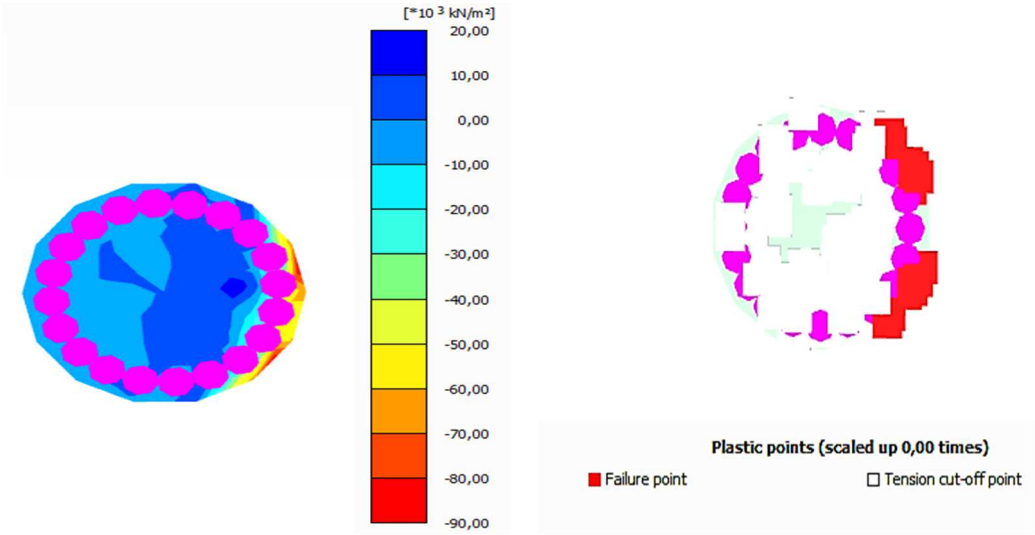

(a)

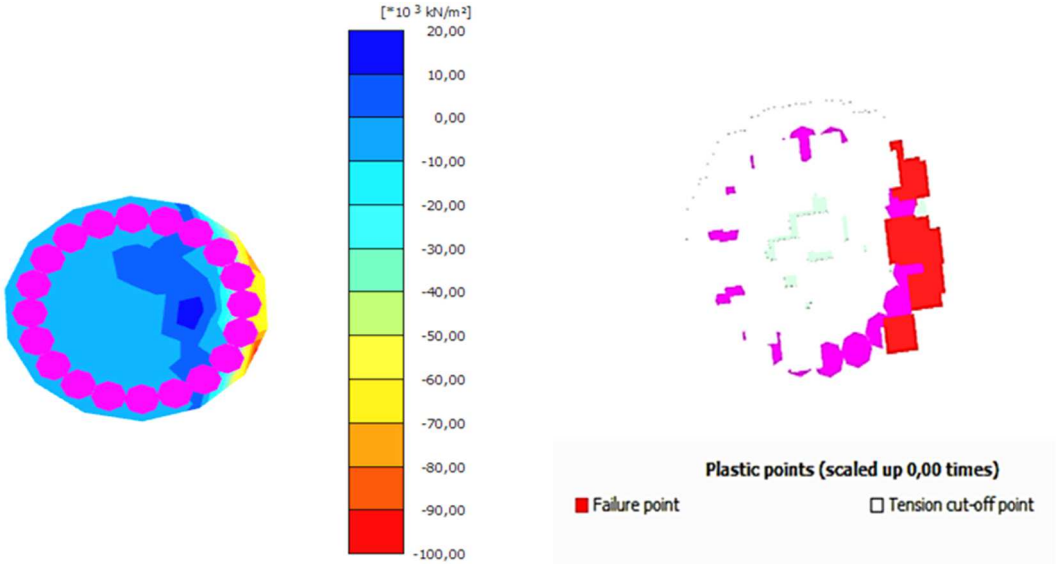

(b)

Figure 4.3.10 Normal stresses and plastic point distribution for: (a) Detailed Concrete based model (b) Detailed Mohr-Coulomb based model

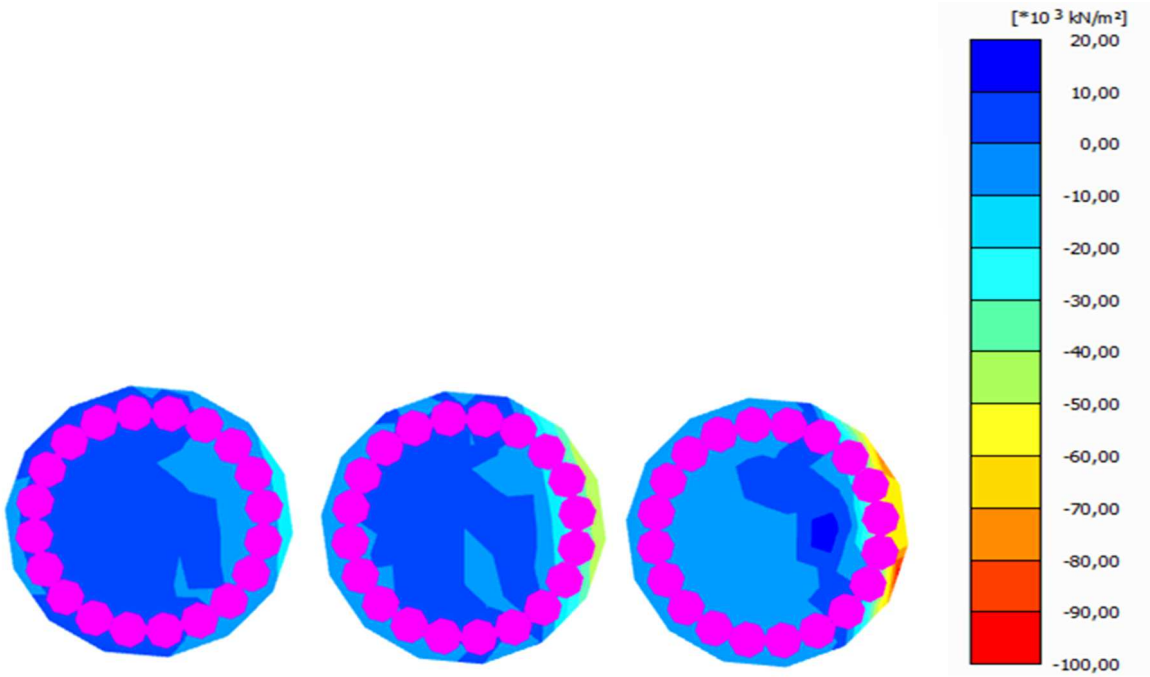

(a) *(b)* *(c)*

Figure 4.3.11 Normal stress shadings at different loading steps of the pushover analysis, for Detailed Mohr-Coulomb based model. Applied loads: (a) 42 kN, (b) 150 kN, (c) 180 kN

For analyses with reinforcement ratio equal to As=1%, when a number of beam elements was less than 20, e.g. 10Φ32, unexpected failure occurred at a low load stage and extensive cracking in the tensile zone was observed. Reinforcement bars seem not to function, as failure occurred before any beam had reached its yield strength. This is obviously a numerical error, probably due to the fact that stiffness matrix cannot be reversed easily in large areas of plain concrete as a very large number of equations needs to be solved. This fact leads in failure in load advancement procedure. In order to overcome this threshold a number of at least 20 beams was used with smaller diameters, e.g. 20Φ22 for As = 1%. However, detailed Mohr-Coulomb based model seems to be functional for smaller diameters of beam elements, as illustrated in Figure 4.2.10 (a), below, where the load-deformation response is plotted considering 10 beams of 32 mm diameter.

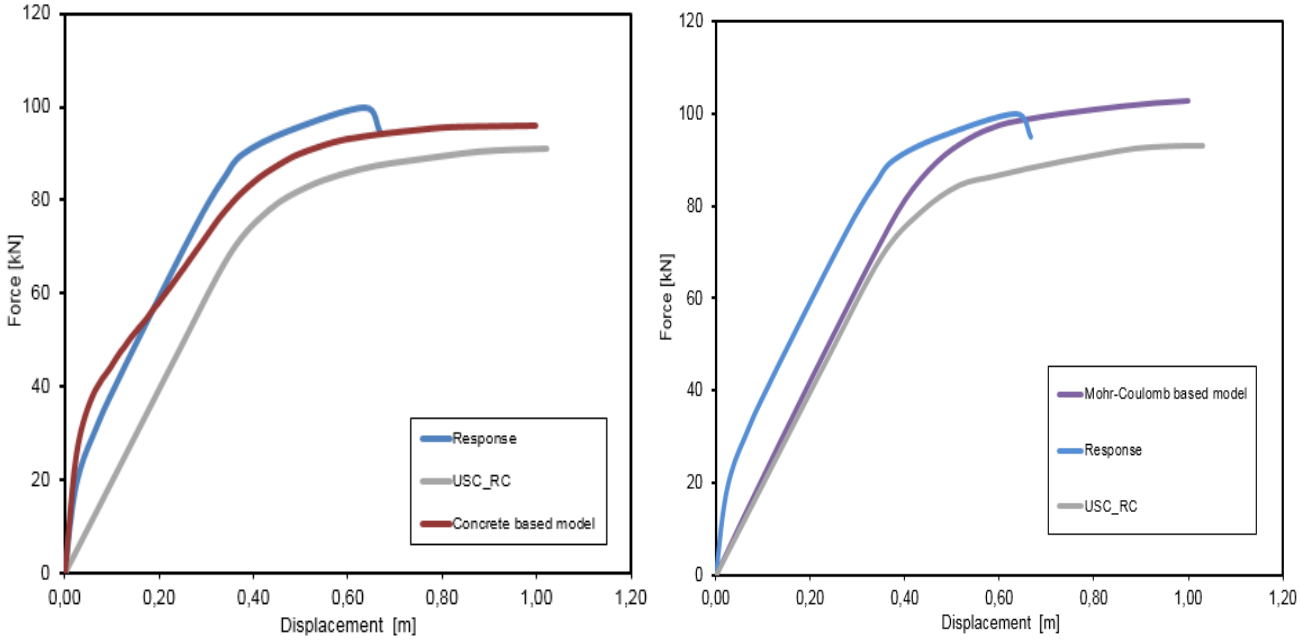

(a) (b)

Figure 4.3.12. Comparison of load-deflection responses from analyses with Detailed (a) Concrete based and (b) Mohr-Coulomb based models and from reference models , with As=1%

The following tables present the comparison between the ultimate calculated moments from Detailed models used in analyses and reference models, as well as the deviations between Concrete based model and the other approximate models.

Tables 4.5 a-b: Comparison of ultimate bending Moments for: a- As=2% , b- As=1%

a. Ultimate Bending Moment [kNm] As=2%			
Concrete based	Mohr-Coulomb based	USC_RC	Response
2989.6	3022.1	2678.5	3069.2

b. Ultimate Bending Moment [kNm] As=1%			
Concrete based	Mohr-Coulomb based	USC_RC	Response
1534.4	1646.4	1457.6	1681.3

Tables 4.6 a-b: Deviations of ultimate bending moments between Detailed Concrete based model and reference models for:

a- As= 2%, b - As=1%

a. Deviations (%)_As=2%	
Detailed M-C based	-1.088 %
USC_RC	10.41%
Response	-2.66 %

b. Deviations (%)_As=1%	
Detailed M-C based	-7.29 %
USC_RC	5.01 %
Response	-9.57 %

4.3.3 Interaction analysis

Until now, pushover analysis was performed considering only lateral loads applied to the reinforced concrete column, without imposing any axial load. By evaluating the results arises the conclusion that Concrete model, is calibrated correctly and therefore it captures realistically the exact behavior of the reinforced concrete element, in pure bending conditions, as it is expected from its advanced formulation. In this chapter the RC column is subjected to combined axial and lateral force, aiming to construct a reproduction of the M-N failure envelope for the calibration of Macroscopic model.

Procedure

The same model as in the previous analysis is used with longitudinal reinforcement ratio equal to As=2%.In the first stage of the analysis, the column is subjected to distributed stress simulating the axial force. From the previous analyses arises the conclusion that, for reinforcement ratio As=2%, Response approaches better the behavior of concrete model in pure bending conditions (see Table 4.7a), than USC_RC. Therefore, the interaction curve extracted from Response is used as a guide for the vertical loading pattern, from the ultimate axial compression capacity to the ultimate axial tension capacity. In the second stage, through force or displacement controlled analysis, depending on the magnitude of the axial force, the maximum load is calculated and multiplied by the length of the column. For small axial forces displacement controlled analysis gives better results, whether for larger axial loads (compressive or tensile), force controlled type of analysis is chosen, based on the criterion of minimizing the deviation compared to Response. The failure envelope is determined by 11 points in total, extracted through the numerical analyses. In Figure 4.3.11 the results from finite element analysis are plotted together with the interaction diagram from Response.

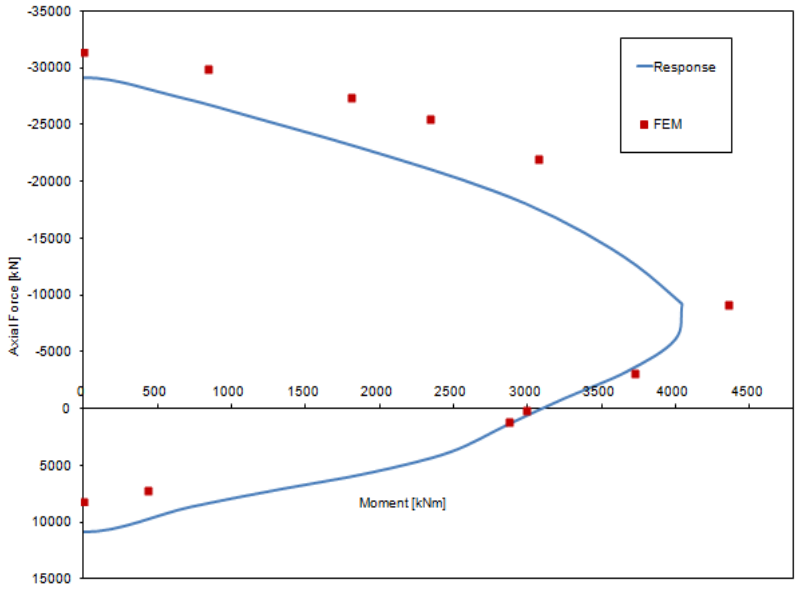

Figure 4.3.13. Comparison of results from numerical analyses and failure envelope from Response

Results from numerical analyses indicate an overestimation of ultimate bending moment capacity as compressive axial force increases (compression controlled region), and an underestimation as tensile axial force increases (tension controlled region). In the vicinity of pure bending conditions almost a perfect fit is observed. In order to have a second basis for comparison, results obtained from Plaxis are compared with a hand calculated interaction diagram, according to EC-2.

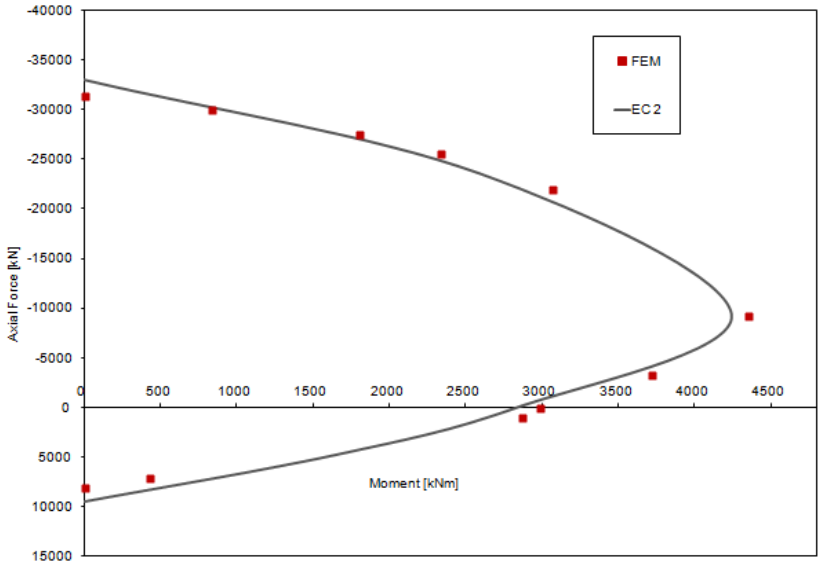

Figure 4.3.14. Comparison of results from numerical analyses and interaction curve according to EC-2

A better fit is observed for most points. This fact indicates the problem defined in the present thesis, namely the deviations between different methods and models, in calculating ultimate capacity of a RC member. Results from Plaxis at failure state, for 4 indicative points of the interaction curve, are displayed in Figure 4.3.14. Observation of the failure mechanisms, confirm what is expected from theory. More specifically:

- brittle failure without yielding of reinforcement for points above balance point
- ductile failure and yielding of the beam elements for points below balance point
- sever cracking of the concrete under pure tension with reinforcement undertaking all tensile forces

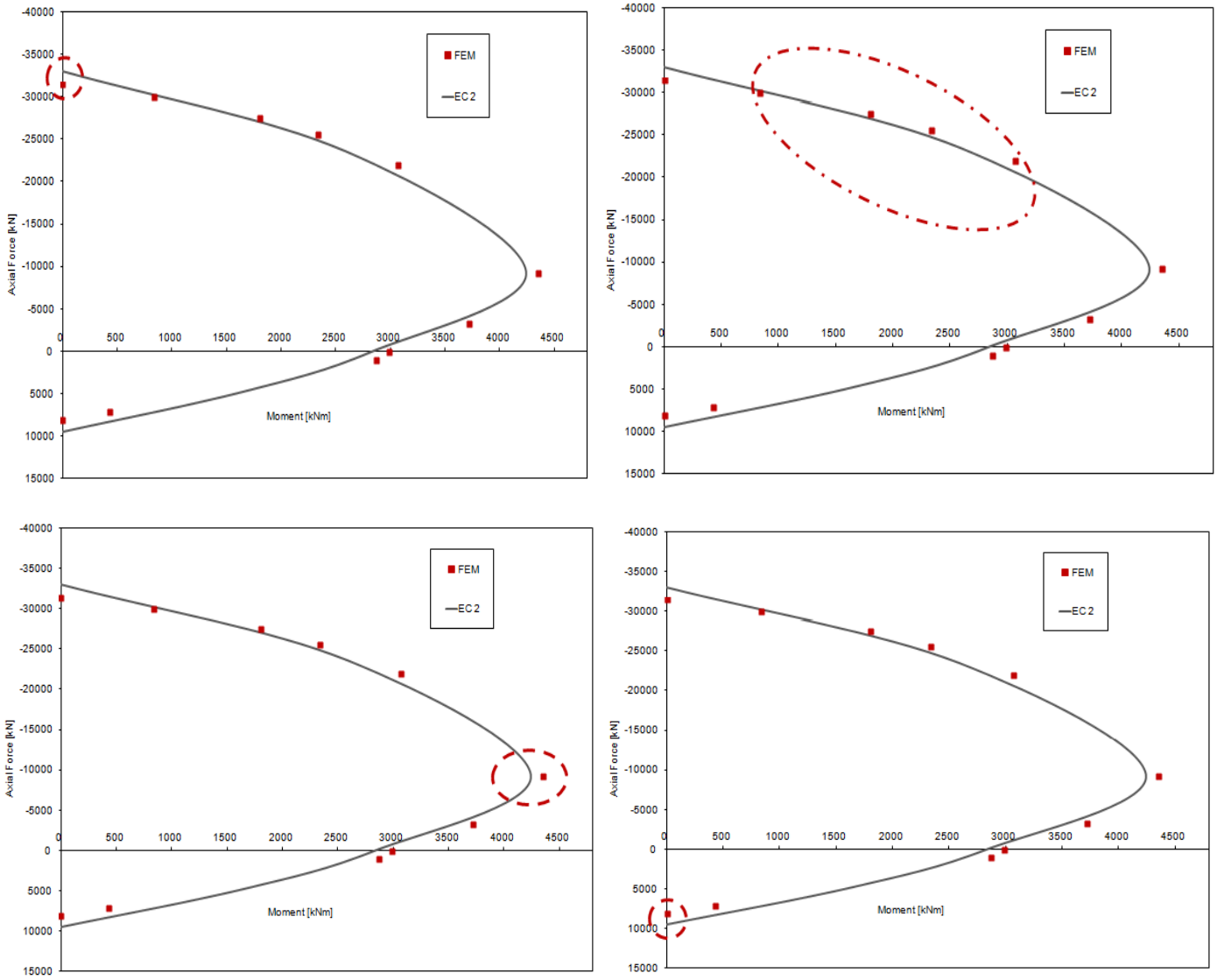

Figure 4.3.15 Illustration of 4 regions from pure compression to pure tension

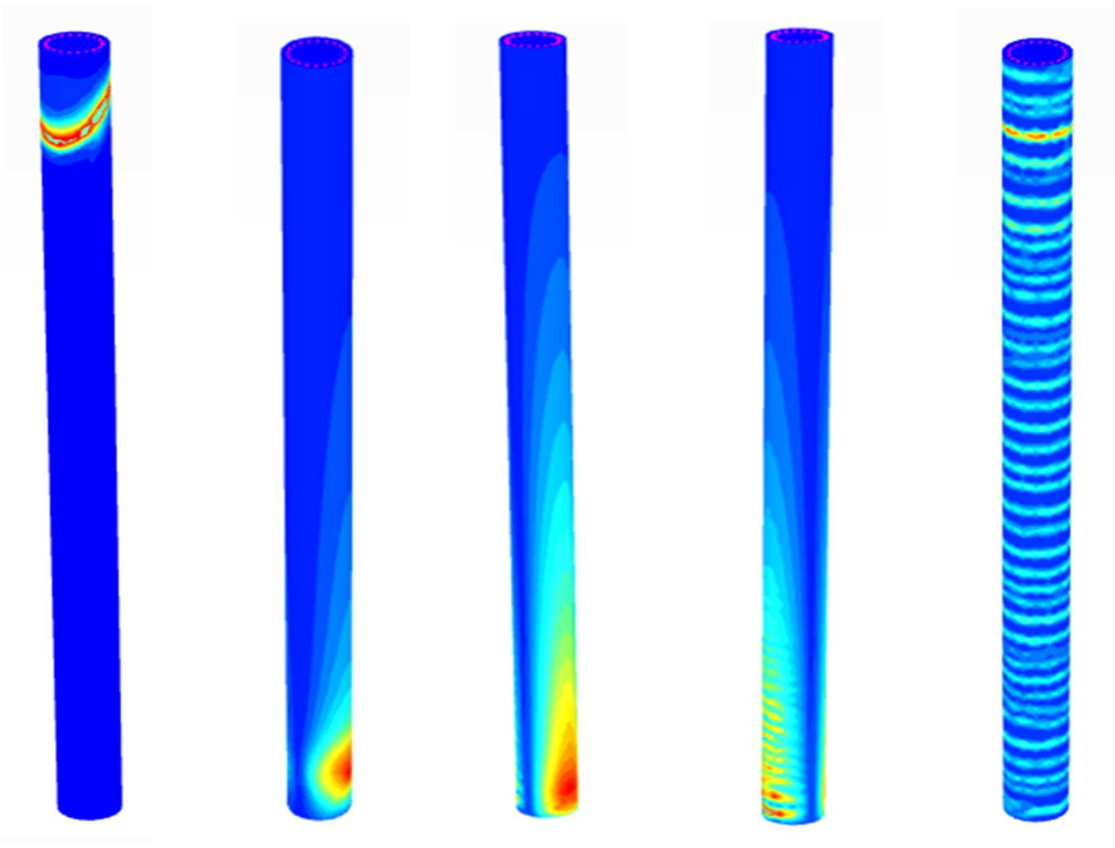

(a) (b) (c) (d)

Figure 4.3.16. Failure mechanisms for the 4 indicative combinations: (a) pure compression, (b) compression controlled region, (c) balance point, flexure crack pattern in tensile zone, crushing in compression (d) pure tension, severe cracking

4.4 Macroscopic Mohr - Coulomb based model

In this modeling approach the column is represented as a soil volume with Mohr-Coulomb model ruling its response. As described in chapter 3, for the simulation of the reinforced circular concrete element no detailed reinforcement is required. With this simple constitutive law the behavior of a circular reinforced concrete pile can be simulated by defining only 4 parameters. These are: 2 elastic parameters, modulus of elasticity E, and Poisson's ratio v, and two plastic parameters, cohesion c and tension cut-off, σ_t. Gerolymos et al, (2014) calibrated the model according to interaction analysis results extracted from the computer code USC_RC and proposed values for c and σ_t, for different diameters of piles and longitudinal reinforcement ratios. In the present study, a case of a circular column-pile is examined with a diameter of 1 m and longitudinal reinforcement ratio As = 2%. Therefore the proposed values can be directly applied in the FE model. These values are 16676 kPa for cohesion and 10067 for tension cut-off. Again, for this setup a total displacement fixity is placed at the bottom and a stress distribution is applied on top. A mesh consisting of 21940 elements is generated.

First results

In analyses modulus of elasticity is set equal to 10 or 15 GPa. The reason for this is that it represents the effective modulus of elasticity and not the tangent, as Macroscopic model simulates the uniform behavior of the reinforced concrete element. Analysis with E=15 GPa leads to a stiffer response and provides only a slight increase of the total capacity of the pile (1.87 %). Comparative results are presented Figures 4.4.1 (a)-(d), below.

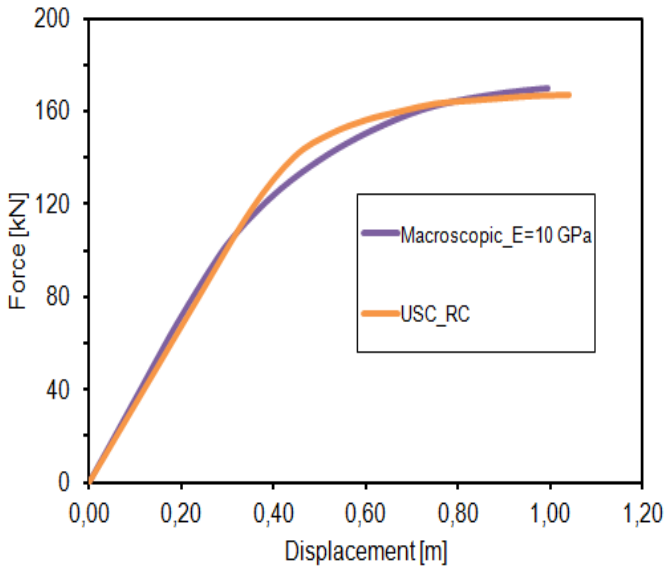

(a)

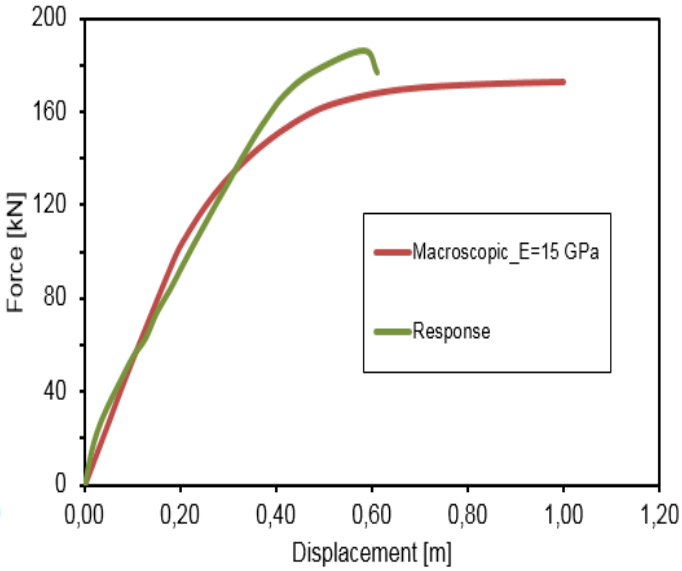

(b)

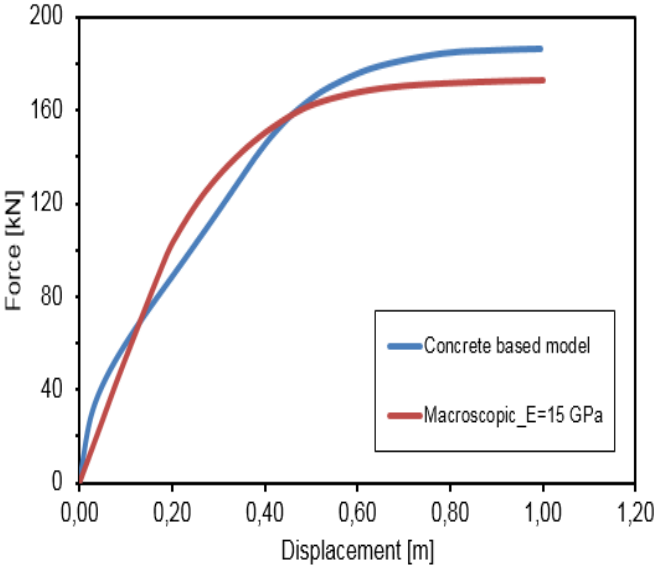

(c)

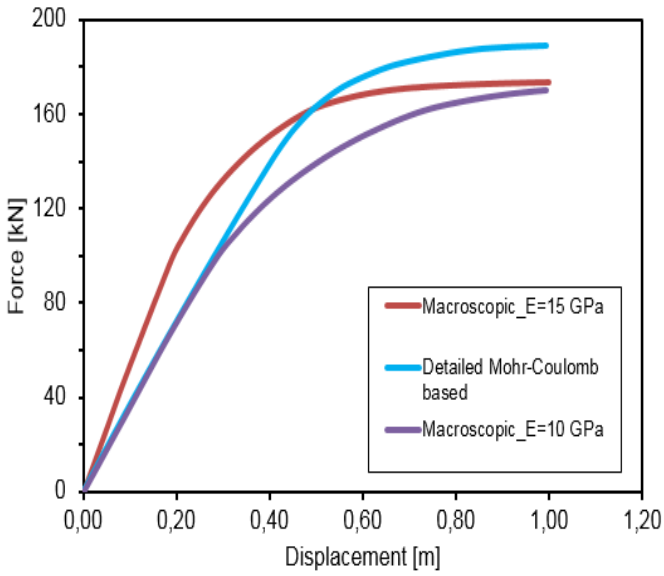

(d)

Figure 4.4.1. Comparison of results from pushover analyses

In Figure 4.4.1 (a) results from numerical and fiber analysis are presented. The two diagrams almost coincide.

Figure 4.4.1 (b) presents the comparison between analysis with E=15 GPa and results from Response. Similar behavior is observed at the initial part of the diagrams, until 140 kN approximately. From that point macroscopic model presents a more ductile behavior and produces higher plastic deformations. The deviation between the two responses is 7.8%.

In figure 4.4.1 (c), results from the analysis with E=15 GPa are exhibited together with results from Detailed Concrete based model considering tensile strength equal to 2 MPa. Again, a considerable deviation of ultimate strength capacity between the 2 models, is observed (7.76%).

Lastly, in Figure 4.4.1 (d), results from both numerical analyses compared to those from detailed Mohr-Coulomb based model, are displayed. For analysis with E=10 GPa a complete convergence is observed until a load of 90 kN. After that point macroscopic model gives higher plastic deformations (11.15% deviation). For analysis with E=15 GPa a smaller deviation in ultimate capacity is observed (9.10%). However macroscopic model presents a stiffer overall response.

A general conclusion that can be derived by observing the results, is that for constitutive models in which tensile strength is taken into account, higher modulus of elasticity should be used in the numerical simulation with Macroscopic model. The reason for that, is the fact that tensile strength of concrete provides an increase of the initial stiffness of the response.

Recalibration of the model - Results

In order to reduce the aforementioned deviations the model is recalibrated, utilizing moment-axial force combinations extracted from numerical analysis with detailed Concrete based model, as described in the previous chapter. The nonlinear algebraic system formulated by Eqs (4.3.3.1) and (4.3.3.4) is solved through the optimization procedure described in chapter 3. The values derived are cohesion, c and angle of friction φ, which are computed equal to 10700 kPa and 35° respectively. The updated values are inserted in the numerical simulation of the RC pile and new results are obtained. Comparative results from analysis with E=10 GPa, are displayed in Figure 4.4.2.

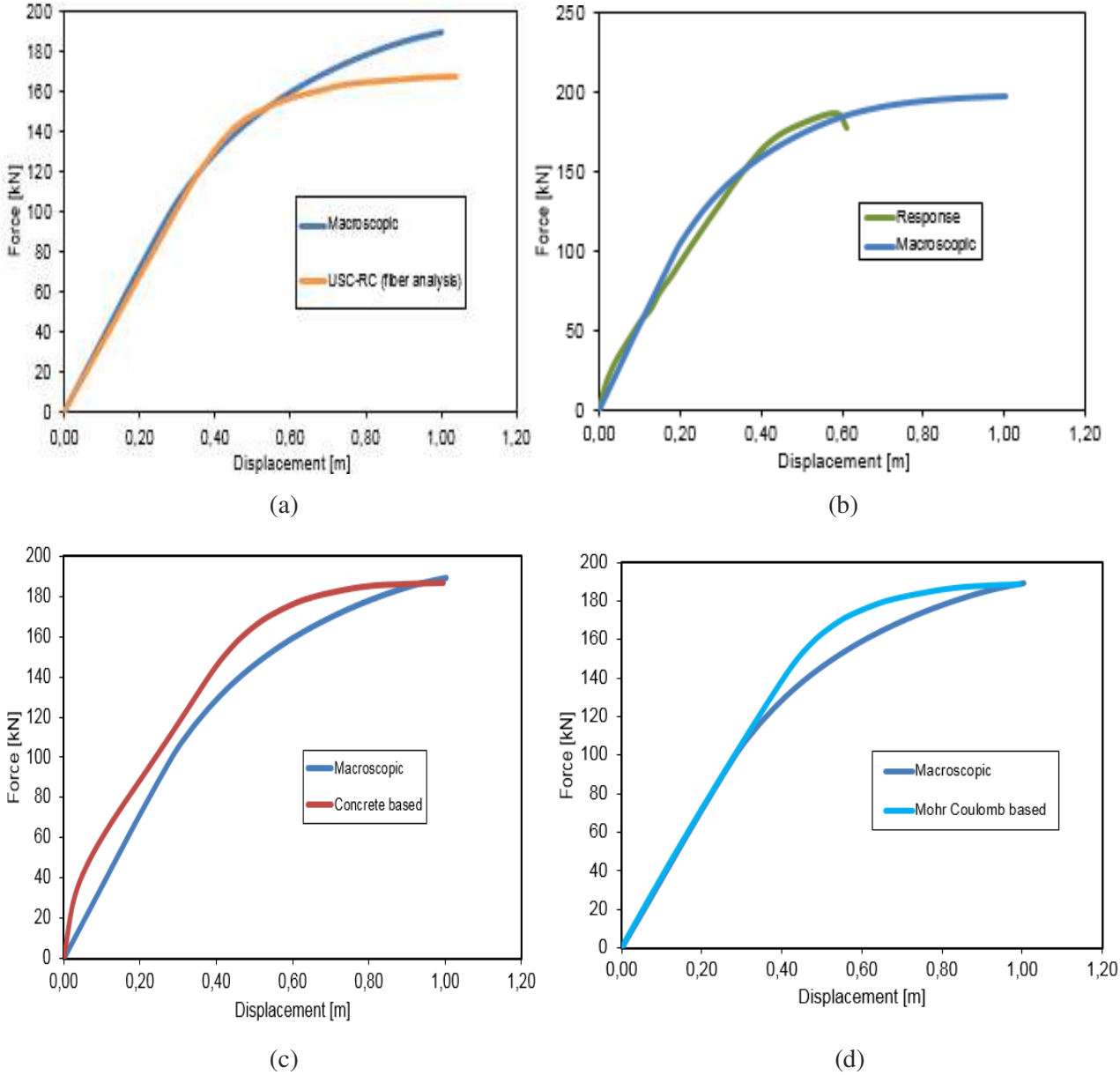

Figure 4.4.2. Comparison of results from pushover analyses

In Figure 4.4.2 (a) results from numerical and fiber analysis are presented. The two diagrams coincide at the initial part, while higher deviation is observed after yielding, as USC_RC presents a smaller hardening stiffness, compared to macroscopic (11.6% deviation).

In figure 4.4.2 (b) the two graphs are similar unless failure state, where Response gives a more brittle failure.

In Figure 4.4.2 (c), a stiffer response for Concrete based model is observed. However much better convergence is succeeded as the deviation is reduced to 1.0% compared to 7.76% obtained from the previous analysis.

Lastly, in Figure 4.4.2 (d) the two models present the same response until 110 kN. After that point results from detailed Mohr-Coulomb based model indicate generation of plastic deformations at higher loading rates. However convergence is succeeded at failure state. It is remarkable that a 0.26% deviation between the 2 models is succeeded compared to 9.10% obtained from previous analysis.

By evaluating the results, it seems that, recalibration of Macroscopic model results in satisfactory convergence between the three proposed phenomenological models.

4.5 Discussion of results

The response of the three proposed models used in the previous described numerical simulations is portrayed together with results from reference models, in terms of force-displacement and moment-curvature (Figure 4.5.1 (a) and (b)). It is observed that the three developed phenomenological models coincide in terms of moment-curvature and remarkable convergence is succeeded for member responses at failure state. Computer code Response presents a more brittle behavior, however insignificant deviations are indicated between Response and proposed models. Deviations from USC_RC are quite higher. By evaluating the results the proposed models seem to be capable to describe accurately the nonlinear behavior of reinforced concrete elements. Table 4.7 presents bending moment capacities derived from all analyses for As=2% for a more detailed comparison. It has to be pointed out, that curvature is not a direct output of Plaxis 3D code. Therefore curvature was calculated utilizing the finite difference method for the area where maximum curvature occurs, which is the bottom of the cantilever.

Table 4.7: Comparison of ultimate bending Moments for As=2%

Ultimate Bending Moment [kNm] As=2%				
Detailed Concrete based	Detailed Mohr-Coulomb based	Macroscopic	USC_RC (fiber analysis)	Response
2990	3022	3030	2678	3069

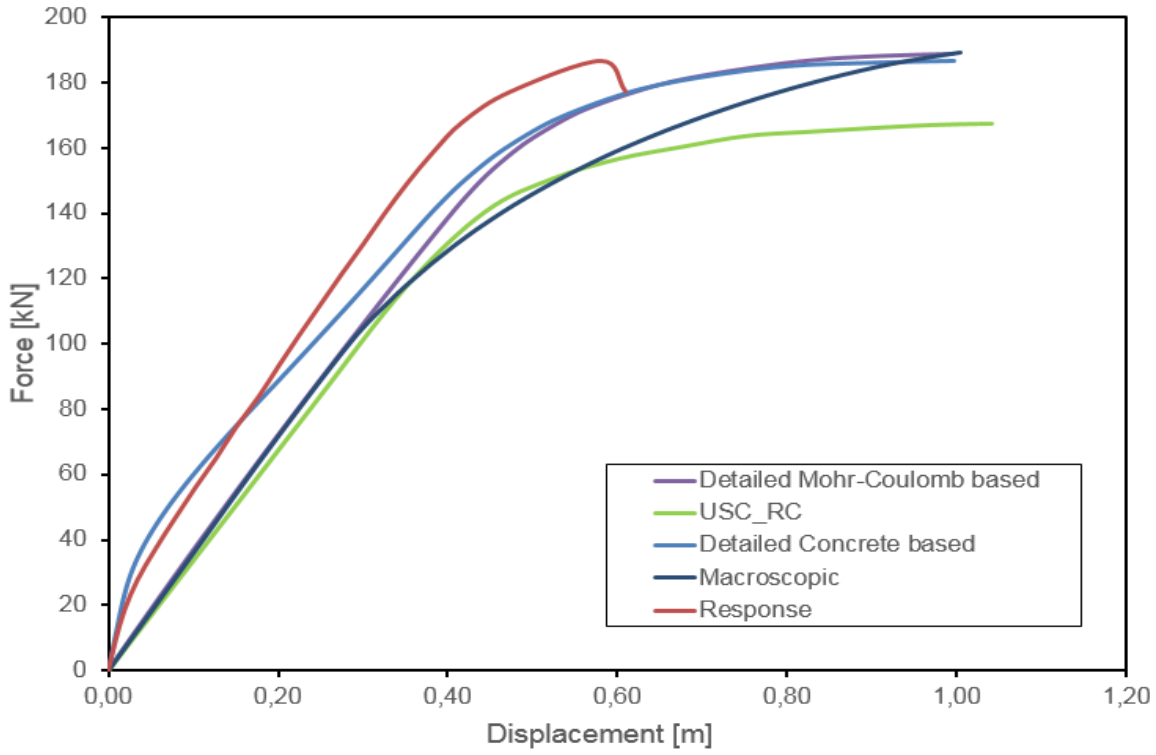

(a)

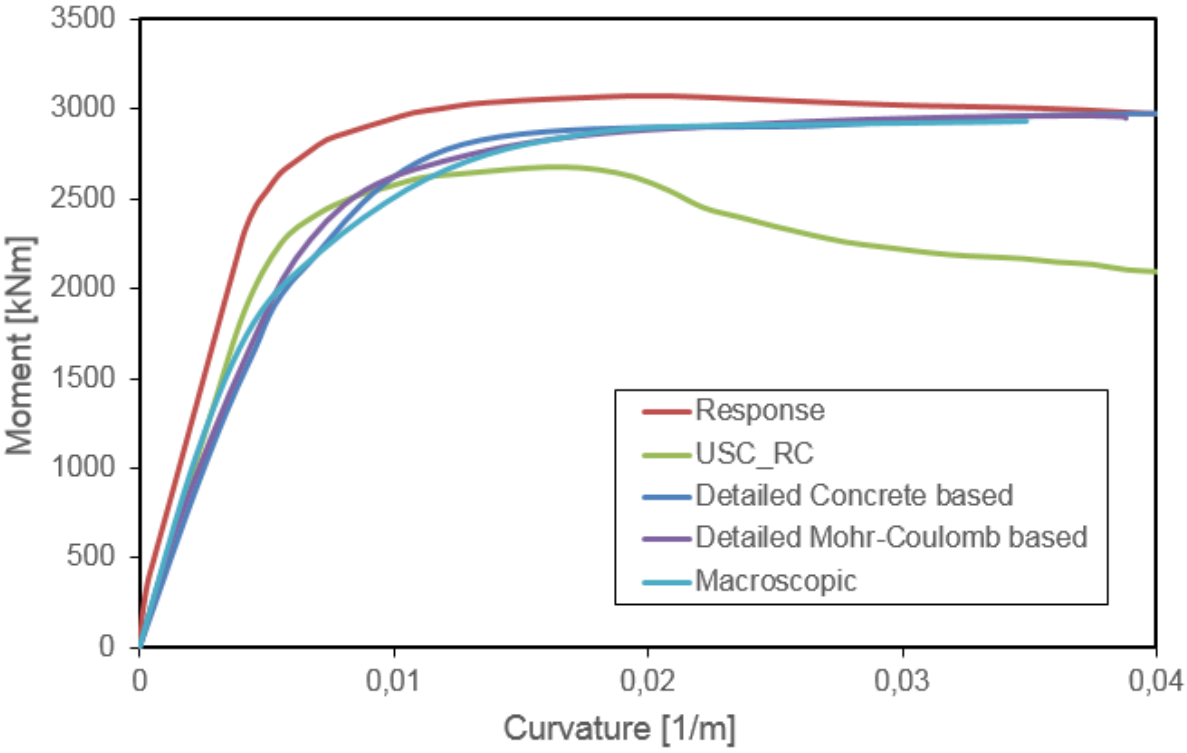

(b)

Figure 4.5.1 Total results from numerical analyses and reference models (a) Force-displacement response (b) Moment-curvature response

At this point, computational time required for analyses with the three suggested phenomenological models should be evaluated. For all model setups fine meshes were created. For Detailed Mohr-Coulomb based and Concrete based models, as they have the same geometrical properties the total number of elements created is almost the same. Therefore, any deviations in computational time between the two models are not associated with mesh coarseness. For Macroscopic approach, fine meshing led to a slightly smaller number of elements due to the different geometry of the model.

A remarkable fact is that Macroscopic model require more than 20 times less computational time than the other two models. It seems that its formulation and geometric simplicity result in effortless calculations. Moreover from analyses arised that Detailed Mohr-Coulomb based model requires almost 1.3 times larger computational time than Concrete based model for the case examined. This is unexpected if we consider that Concrete material is a more advanced, complex model compared to Mohr-Coulomb which is based on the assumption of perfect elastoplasticity.

5 Numerical analysis of pile - soil interaction

5.1 Introduction

In this chapter the behavior of a single pile subjected to monotonic lateral and combined lateral and vertical load, is investigated utilizing Plaxis 3D code. The three constitutive models defined and verified previously are applied to a reinforced concrete pile and pile-soil interaction is studied. As mentioned in the problem definition usually in numerical simulations pile material is considered linear elastic and therefore response up to failure is not investigated. Therefore the performance of the models to represent the nonlinear pile behavior is investigated considering two aspects. The first is the influence of vertical loading on lateral response of piles embedded in clayey soil. The second aspect has to do with the influence of sliding and gapping of the pile from the surrounding soil, by examining cases assuming full bond conditions, as well as separation. Gapping, combined with inelastic structural response of the pile enhances difficulty of the problem. In numerical simulations interface properties define whether separation and sliding of the pile from the soil will be taken into account. Results of a series of numerical analyses, in terms of horizontal force - pile head displacement, moment distribution along the pile, as well as deflection profiles, are finally compared and discussed.

5.2 Geometry

Figure 5.2.1 illustrates the basic geometry of the model. A volume pile of 1 m diameter and 16 m length is created in the middle of the geometry. The distance from the pile tip to the bottom of the model is considered 5 times of the pile diameter. The lateral boundaries are placed at a distance of 0.6L m, taking into account the effect of boundaries on the pile's response and computational time. For each case a fine mesh is created to ensure objective results.

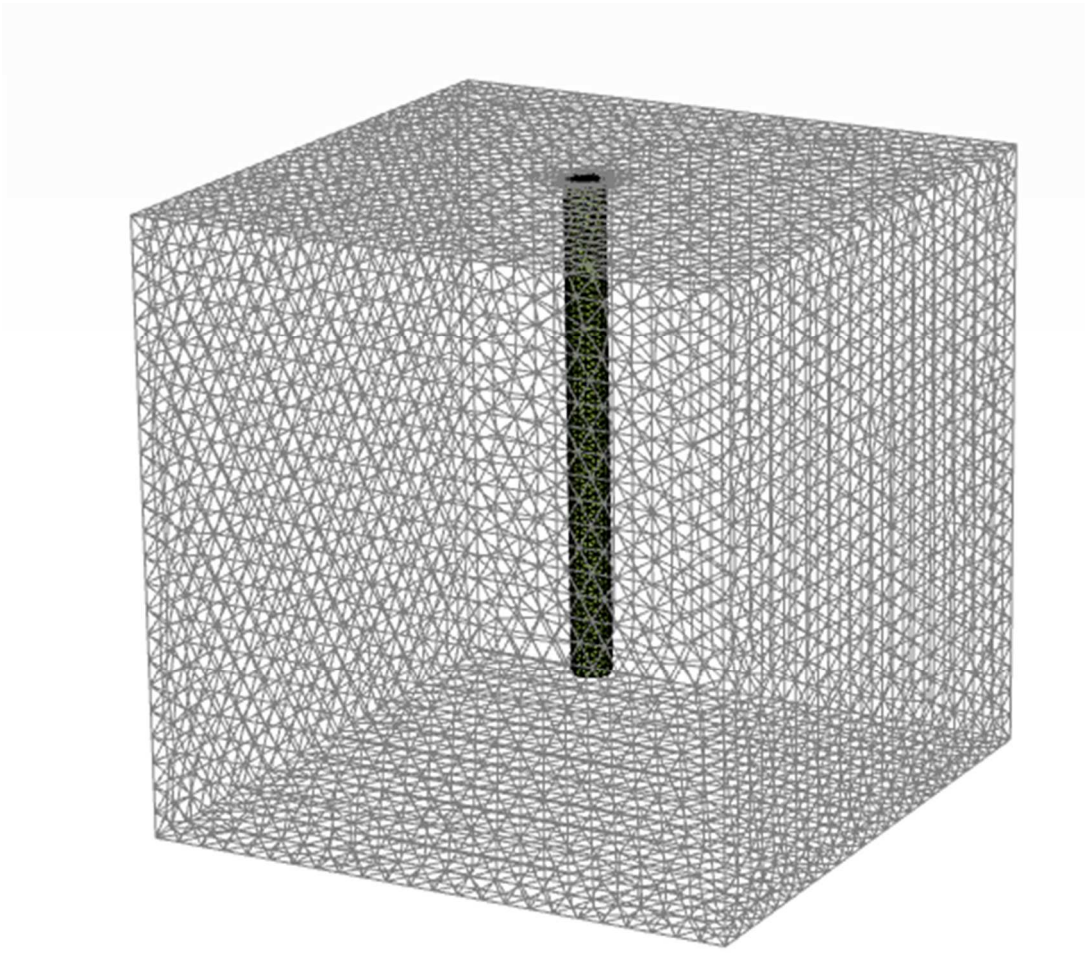

Figure 5.2.1 Geometry of the model

5.3 Materials

Soil

The selected soil is one layered consisted of stiff clay under undrained conditions, with constant modulus of elasticity. The Mohr-Coulomb yield criterion is chosen to describe its behavior. Parameters for the soil material are listed in Table 5.1 below.

Table 5.1: Soil material parameters

Soil Type	Undrained shear strength, s_u [kPa]	Modulusof Elasticity, Es [MPa]	Unit Weight, γ [kN/m^3]	Poisson's ratio,v [-]
Clay	60	85	20	0.4

Pile

The reinforced concrete pile is simulated as a 3D cylindrical soil volume element. As for the pushover analysis, for the pile-soil interaction the three developed phenomenological constitutive relations, are assigned to the pile volume. At first the behavior of the pile is modeled via Mohr-Coulomb based models, namely Detailed and Macroscopic. Subsequently Concrete model is assigned to the pile material, which again needs to be calibrated due to the alteration of mesh properties. A pile of 1m diameter is considered, with longitudinal reinforcement ratio As=2%. For Concrete and Detailed models the reinforcement is simulated with 20 elastoplastic 3D beam elements of 32 mm diameter and yield strength f_y = 500 MPa . The pile is 16 m long, free headed and full embedded in the clayey soil layer. A rigid plate is modeled at the top to avoid local stress concentration.

Interfaces

In order to capture pile-soil interaction, interface elements are placed between the pile and the surrounding soil. Interfaces are double noded elements and provide the stresses due to applied horizontal loads in three components:

- effective normal stress ($\sigma_{N'}$)
- horizontal shear stress (τ_2)
- vertical shear stress (τ_1)

The lateral resistance of the soil due to horizontal forces can be described by the normal stress ($\sigma_{N'}$) and the horizontal shear stress (τ_2) as shown in Figure 5.3.1.below.

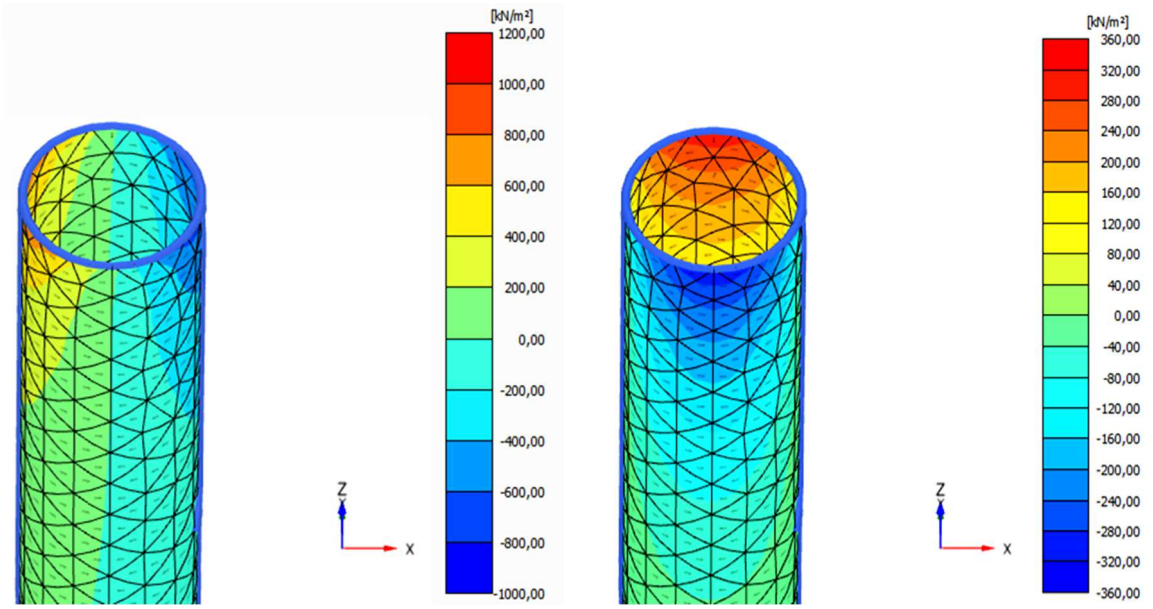

(a) *(b)*

Figure 5.3.1. Stress distrubition at interface elements (a) normal stresses (b) shear stresses

Interface properties are basically defined with the parameter R_{inter}. This parameter relates the strength of the interfaces with the strength of the soil, according to the following relations:

$$\tan \varphi_{inter} = R_{inter} \tan \varphi_{soil} \quad (5.3.1)$$

$$c_{inter} = R_{inter}\, c_{soil} \quad (5.3.2)$$

When the interface is set as Rigid, R_{inter} =1 and it has the same properties as the surrounding soil. Therefore full bonding conditions are considered.
However, in general strength decreases at the interaction zone between the pile and the soil and using a smaller value may give more realistic results, taking separation and slipping effects into account. In this study both cases are investigated.

5.4 Procedure

As it was mentioned above, cases with only lateral loading as well as combined axial and horizontal force are studied. For each model 4 cases are studied, as presented in Table 5.2.
The stages of the finite element modeling are:

1. Soil undergoes geostatic loading
2. A cylindrical volume is replaced by the pile, which is either reinforced with 20 solid beam elements, or when applying Macroscopic model equivalent properties simulate the reinforced concrete material. Depending on the case examined, vertical load N is applied gradually until a specific value. This value is chosen to be around the ultimate compressive axial capacity of the pile divided by 1.5.
3. The vertical load is kept constant and the lateral load is applied, in the form of horizontal uniform distributed stress until failure of the system.

Table 5.2: Analysed cases

Case	Interface properties		Axial Load	
	Rinter=1	Rinter=0.85	None	N_u/1.5
A1	✓		✓	
A2	✓			✓
B1		✓	✓	
B2		✓		✓

In order to validate the performance of the models applied, two different approaches are adopted.

- For the first approach ultimate soil reaction per unit length is considered constant with depth equal to:

$$P_y = \lambda_1 s_u d, \tag{5.4.1}$$

which is a well known expression for cohesive soils. Coefficient λ_1 varies from 2 to 12 and usually a value of λ_1 = 9 is used for soft clay, while λ_1 = 11 is more appropriate for stiff clay.

The expected ultimate lateral capacity, calculated from static equilibrium is equal to :

$$Q_y = \sqrt{2P_y M_{pl}}, \tag{5.4.2}$$

where P_y is the soil resistance and M_{pl} the ultimate bending moment capacity of the pile member. By replacing in Eq (5.4.2) resulting ultimate lateral loads from numerical analyses λ_1 is calculated and each time it is checked whether is within the aforementioned range ($2 \leq \lambda_1 \leq 12$).Values of M_{pl} are obtained from the pushover analysis described in chapter 4 and are listed in Table 4.8.

- For the second approach the assumption of a trapezoidal distribution of soil resistance is adopted, as shown in Figure 5.4.1. Soil resistance is calculated according to the following formulation proposed by Matlock (1970) :

$$p_y = \left(\lambda_2 + \frac{\sigma'_v}{s_u} + J\frac{z}{d}\right) s_u\, d, \qquad z < \frac{(\lambda_1 - \lambda_2)d}{\frac{\gamma_s' d}{s_u} + J} \tag{5.4.3}$$

Where σ'_v is the vertical effective stress, γ'_s the effective specific weight of the soil and λ_1, λ_2 , J are dimensionless quantities. Broms (1964) proposed a value of λ_2=2 whereas Matlock (1970) used λ_2=3. For J, Reese (1975) suggested a value of 2.83 for all types of clay, whereas Matlock (1970) stated that J was determined experimentally to be 0.5 for soft clay and 0.25 for medium clay. Here, a value of J equal to 0.25 is considered. Eq (5.4.3) can be written as p_y= A + Bz and from static equilibrium one obtains:

$$Q = Af + \frac{B}{2}f^2 \tag{5.4.4}$$

$$Qf - M_{pl} - \frac{Af}{2} - \frac{Bf^3}{6} = 0 \tag{5.4.5}$$

And by replacing (5.4.4) to (5.4.5)

$$Af^2 + \frac{B}{2}f^3 - M_{pl} - \frac{A}{2}f^2 - \frac{Bf^3}{6} = 0 \tag{5.4.6}$$

Therefore by solving the trinomial plastic hinge length f is equal to:

$$f = \left(\sqrt{\frac{9.Mpl^2}{4.B^2} - \frac{3.A^3.Mpl}{8.B^4}} - \frac{A^3}{8.B^3} + \frac{3.Mpl}{2.B}\right)^{\frac{1}{3}} - \frac{A}{2.B} + \frac{A^2}{4.B^2\left(\sqrt{\frac{9.Mpl^2}{4.B^2} - \frac{3.A^3.Mpl}{8.B^4}} - \frac{A^3}{8.B^3} + \frac{3.Mpl}{2.B}\right)^{\frac{1}{3}}} \tag{5.4.7}$$

Values M_{pl} and B are known, therefore by replacing f in Eq (5.4.4) and setting Q equal to the ultimate lateral resistance from numerical analysis, λ_2 can be obtained and check whether $p_y \leq 12S_u$ D.

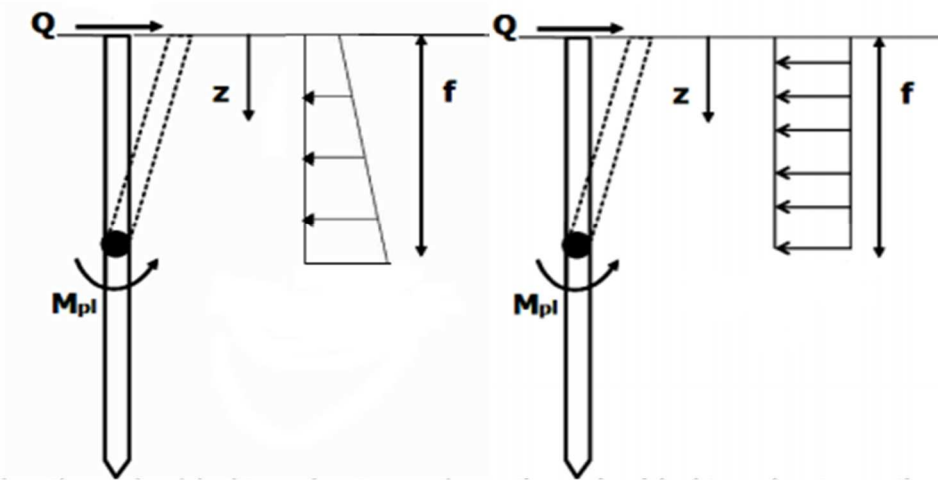

Figure 5.4.1. Constant and trapezoidal distrubition of ultimate soil resistance with depth

5.5 Mohr-Coulomb based model

5.5.1 Detailed model

For the first modeling approach of the nonlinear behavior of the pile material, perfect elastoplasticity is assumed. Therefore, the response of the pile volume is characterized by the Mohr-Coulomb failure criterion. A mesh consisted of 83810 elements is created and same elastic and plastic parameters as in chapter 4 are considered with the addition of tension cut-off. Tension cut-off is added for numerical reasons, in order to enable load advancement procedure. Parameters for the RC pile volume are listed in Table 5.3 below.

Table 5.3 Parameters for pile material

E	ν	γ	c	φ	σt
[GPa]	[-]	[kN/m^3]	[kPa]	[°]	[kPa]
30	0.2	0.001	3879	61	200

Results

Results from numerical analyses for the four examined cases are presented in Figures 5.5.1 and 5.5.2. The first observation has to do with ultimate lateral capacities obtained from analyses. For cases A1 and A2 lateral capacity reaches 1993 kN and 2070 kN respectively. Taking separation and gapping into account results in lower values for ultimate lateral capacity and larger deflections along the pile's length, therefore in an increased active length where the pile undertakes the applied load and deforms. This is portrayed in Figure 5.5.2. For cases B1 and B2 the lateral capacity of the pile reaches 1565 kN and 1638 kN, respectively. For cases A1, A2 values of lateral capacity are quite high, yet within the limits derived from static equilibrium as described above for the assumption of constant distribution of lateral soil resistance. For cases B1 and B2 ultimate soil reaction is within the admissible range ($p_y \leq 12S_u$ D) for both assumptions.

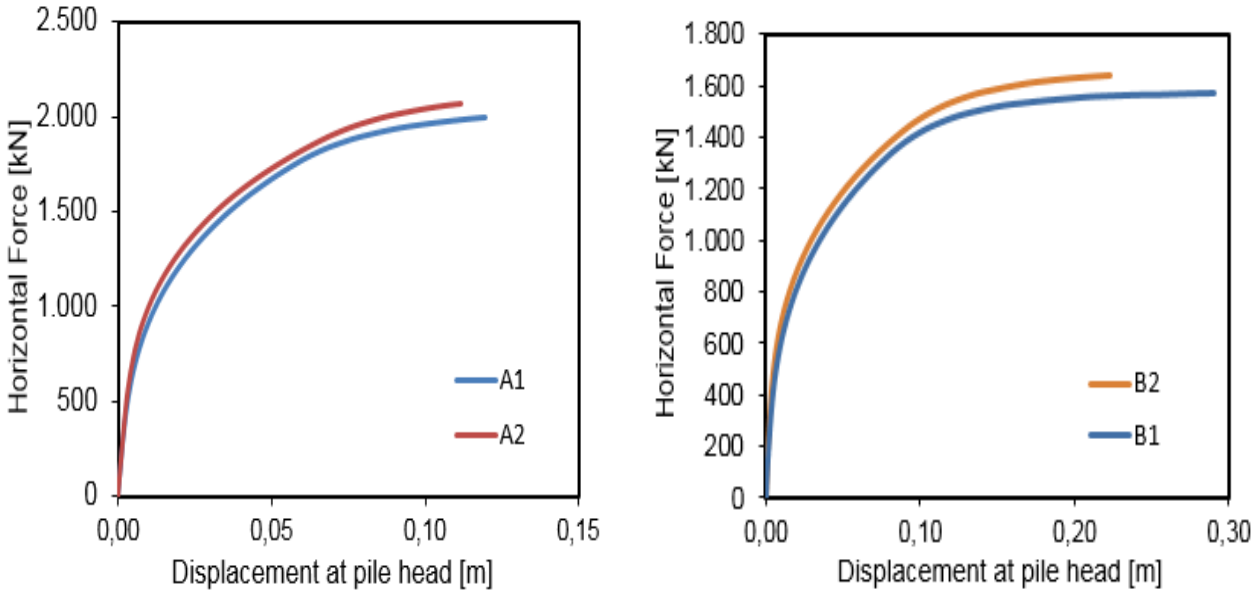

(a) (b)

Figure 5.5.1. Calculated pile head force-displacement curves for cases: (a) A1 –A2: full bonding conditions between pile and soil with and without axial force, (b) B1-B2: sliding and gapping enabled with and without axial force

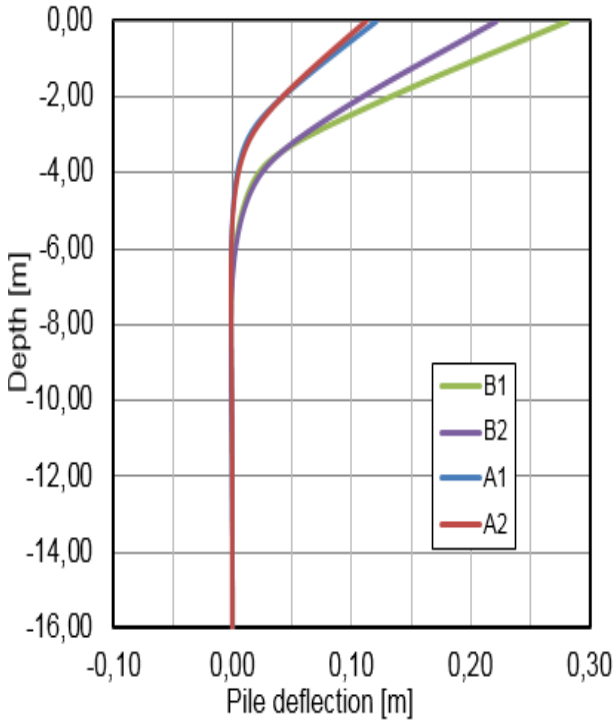

Figure 5.5.2. Pile deflection results for all cases

5.5.2 Macroscopic model

In the second modeling approach the pile is represented as a 3D soil volume with Mohr-Coulomb model describing its response. No detailed reinforcement is required, and parameters as obtained from the calibration procedure described in chapter 4 are assigned to the pile material. A mesh consisting of 70702 elements is generated.

The performance of the model for the examined cases is shown in Figures 5.5.3 and 5.5.4 below. The same pattern as with Detailed model is observed. For cases A1 and A2 lateral capacity reaches 1935 kN and 2033 kN respectively. Gapping again results in lower values for ultimate lateral capacity and larger deflections along the pile's length, as well as in increased active length (Figure 5.5.4). For cases B1 and B2 the lateral capacity of the pile reaches 1433 kN and 1549 kN respectively. For all cases ultimate soil reaction is within the admissible range ($p_y \leq 12S_u$ D) for both assumptions. Implementation of Eqs (5.4.2), (5.4.4) and (5.4.7) with replacement of ultimate lateral capacities derived from analyses, result in acceptable values.

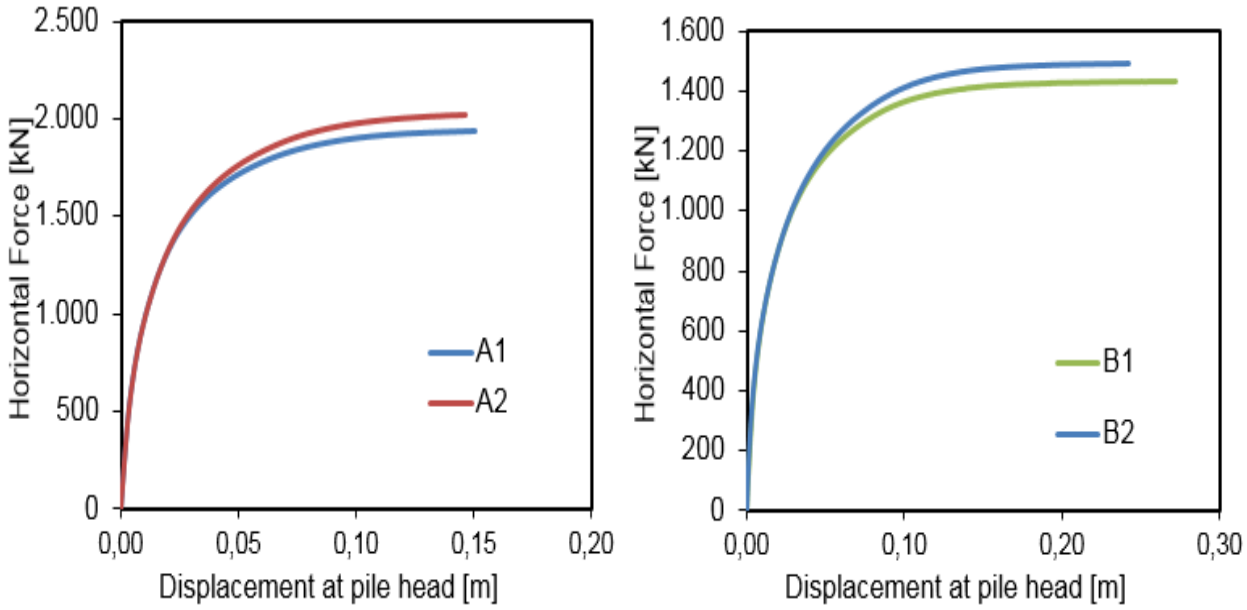

(a) (b)

Figure 5.5.3. Calculated pile head force-displacement curves for cases: (a) A1 –A2: full bond conditions between pile and soil with and without axial force, (b) B1-B2: sliding and gapping enabled with and without axial force

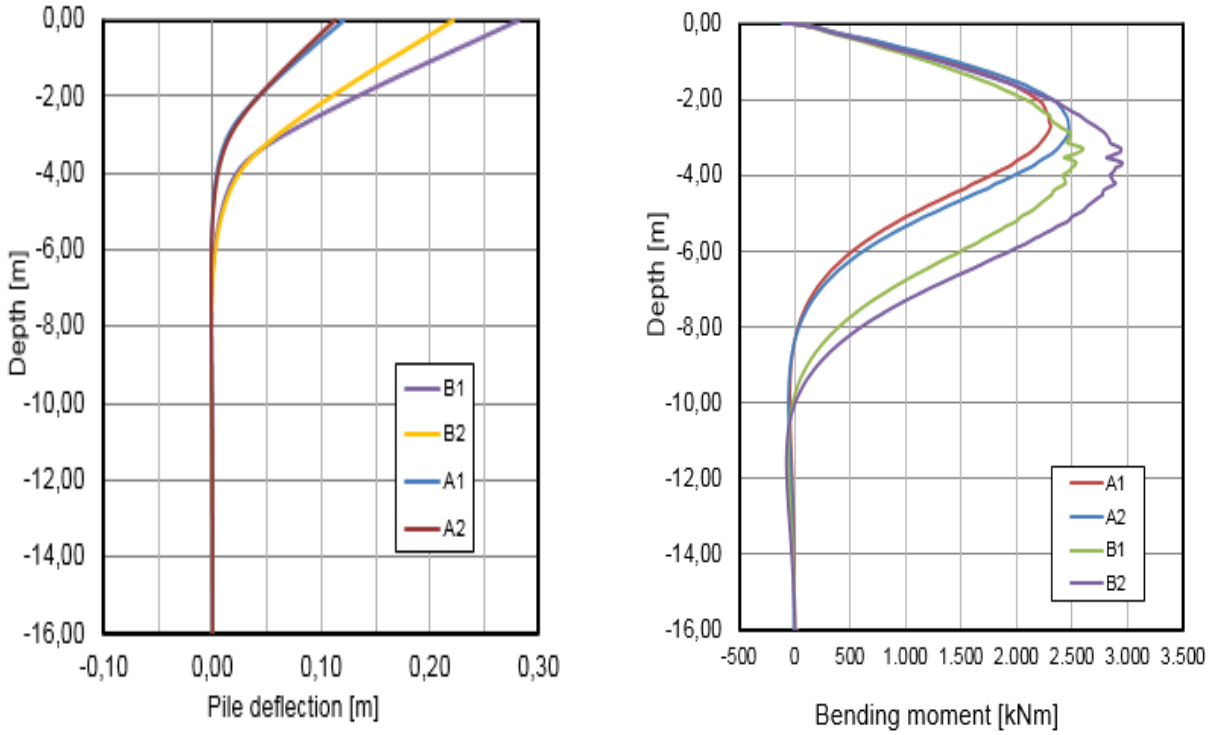

(a) (b)

Figure 5.5.4. (a) Pile deflection profile results, (b) Bending Moment envelopes for the examined cases

By evaluating the results for both models some first conclusions can be derived:

(a) Axial force seems to increase lateral capacity. This is observed for both full bond and gapping and sliding conditions. This observation agrees with results from numerical experiments conducted by Papakyriakopoulos (2013), considering a free headed flexible pile embedded in medium clay (Es=25 MPa, $s_u = 50\ kPa$). Papakyriakopoulos applied to the pile combinations of horizontal force and moment under constant axial load. He repeated the procedure for many factors of safety against vertical loading and extracted ultimate capacities Hu and Mu. According to his results failure of the pile-soil system depends on the allocation of external loads. This is illustrated in Figure 5.5.5 below, where variation of plastic hinge length is shown in respect to the combination M-Q. In our case the pile is subjected only in lateral loading, therefore angle θ is zero and plastic hinge length is expected as marked.

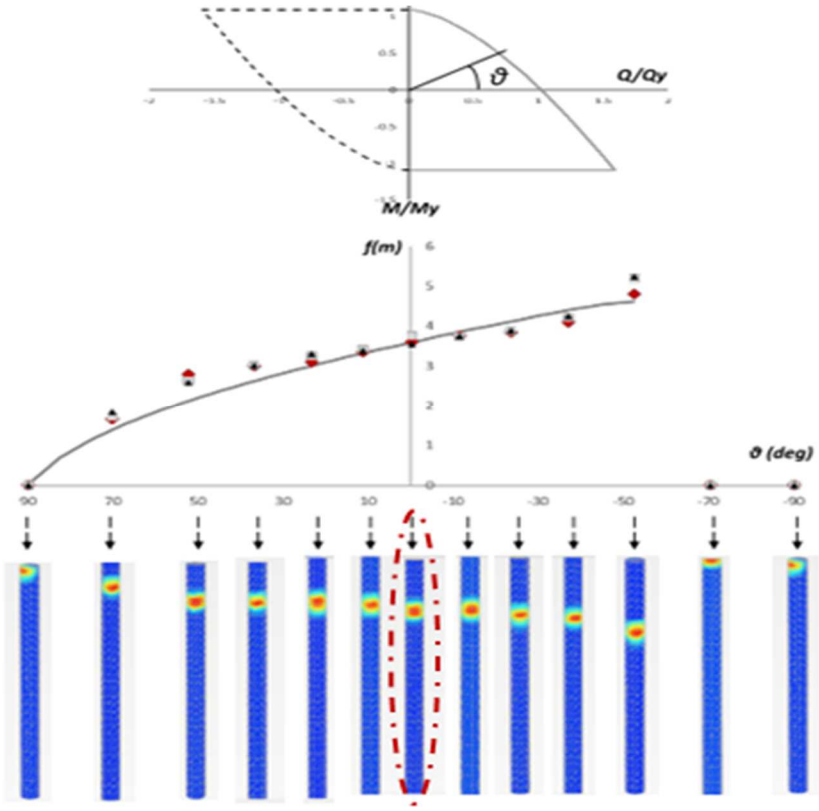

Figure 5.5.5. Variation of plastic hinge depth in respect to load combination angle θ (Papakyriakopoulos 2013)

(b) In Figure 5.5.4 (b) the bending moment profiles are depicted for the four examined cases. It is observed that gapping results in the full mobilization of bending moment capacity as well as in the increase of plastic hinge length. This is clearly depicted in Figure 5.5.6 below.

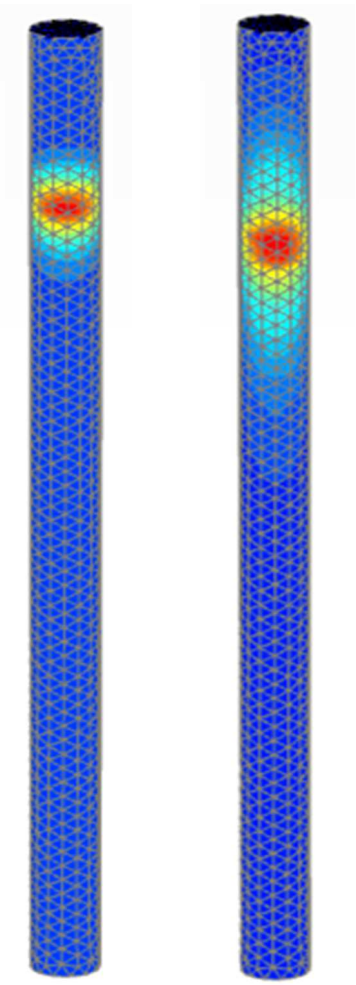

(a) *(b)*

Figure 5.5.6. Comparison of the plastic hinge depth f between cases considering (a) full bonding between pile and soil and (b) gap formation between the pile and the surrounding soil

(c) For all analyzed cases with the two models, the failure mechanism of the pile is the same with the difference that separation and sliding causes the generation of more plastic points distributed along the pile. Plastic hinge formation and length are in accordance with results from Papakyriakopoulos, as described above. Moreover it seems that for all cases large deformation leads to yielding of main reinforcement for Detailed model. The evolution of the plastic hinge is illustrated in Figure 5.5.7

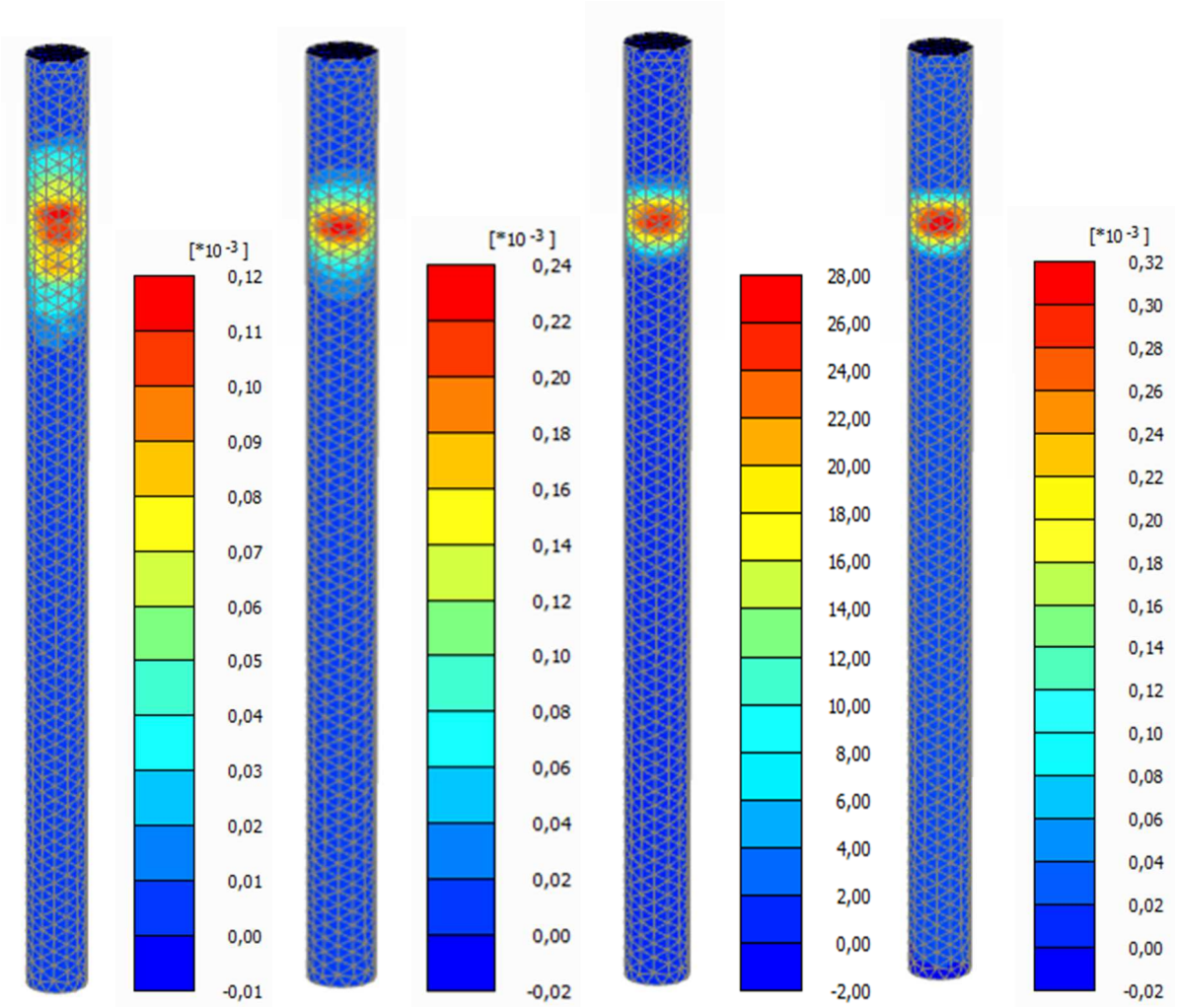

Figure 5.5.7. Evolution of failure mechanism in terms of incremental deviatoric strain Δγs

5.6 Detailed Concrete based model

5.6.1 Model calibration procedure

As it was extensively discussed in chapter 3, fracture energy parameters of Concrete model are sensitive to mesh properties. For the pushover analysis of the RC column, in order to succeed accuracy of results a calibration procedure for the compressive fracture energy G_c has been performed. The mesh created consisted of 43479 elements and the geometry as well as the properties of the surrounding volume were different from the present case. For the pile-soil interaction examined in this chapter, a completely different mesh is created. Due to the expansion of the boundaries of the model, as well as the increased coarseness of the soil volume surrounding the pile, in total 81212 elements are generated. At first emphasis was placed on calibrating compressive fracture energy. As described in chapter 3, and can be visualized in Figure 5.6.1 (a), decreased values for G_c are required for fine meshes compared to coarser meshes. Analyses with the same parameters as before, with G_c =100 kN/m, indicated failure at unexpected, low values without yielding of beam elements. However, results seemed to be insignificantly affected by the alteration of G_c, leading to the conclusion that compressive fracture energy is not the governing parameter for the soil structure interaction problem. The next step was to investigate the effect of tensile fracture energy G_t. At first the same value as in the pushover analysis was considered (0.1 kN/m), keeping G_c constant, equal to 100 kN/m. Cases A1, A2, B1, B2 were examined. Failure occurred at lower values for all of the examined cases without yielding of reinforcement. Considering mesh dependency of tensile fracture energy, according to the diagram shown in Figure 5.6.1 (b), for fine meshes higher values of G_t are required in order to have equivalent results. As a consequence G_t needed to be increased. For case A1, G_t was gradually increased until the criteria described in the previous paragraph, considering ultimate lateral resistance of the pile, to be satisfied and deviations of results from Detailed and Macroscopic models to be minimized. This was succeeded for G_t equal to 0.6 kN/m, resulting in ultimate horizontal capacity equal to 1916 kN.

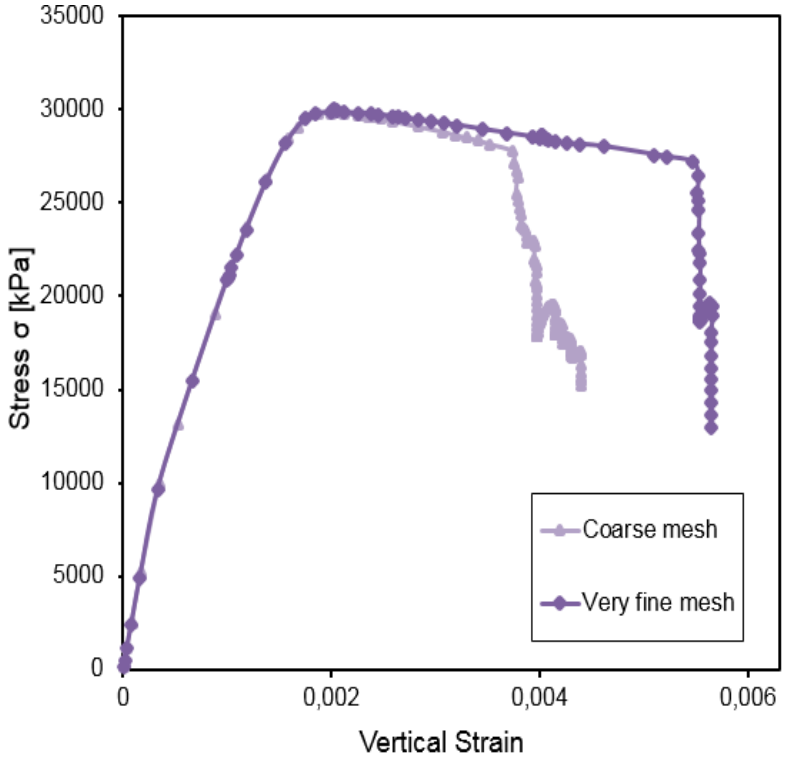

(a)

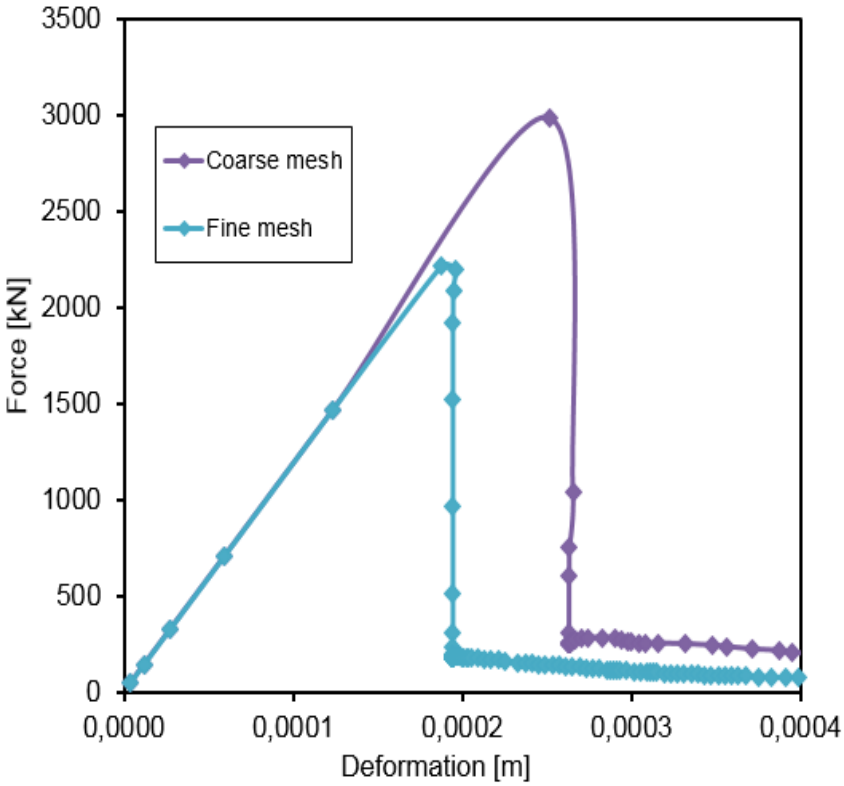

(b)

Figure 5.6.1 Mesh dependency of fracture energy parameters

5.6.2 Analyses and results

After finding the appropriate value of tensile fracture energy, that seems to control the problem, cases A2, B1, B2 are also analyzed. Results are presented in Figures 5.6.2 and 5.6.3 below.

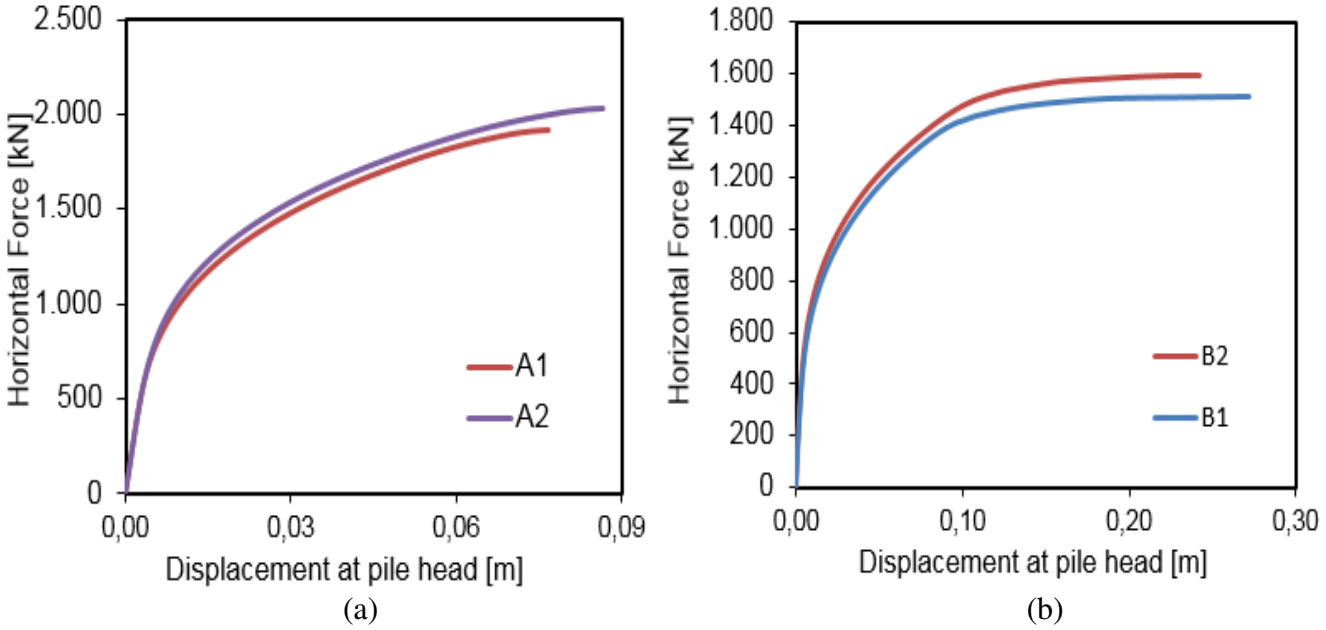

Figure 5.6.2. Calculated pile head force-displacement curves for cases: (a) A1 –A2: full bond conditions between pile and soil with and without axial force, (b) B1-B2: sliding and gapping enabled with and without axial force

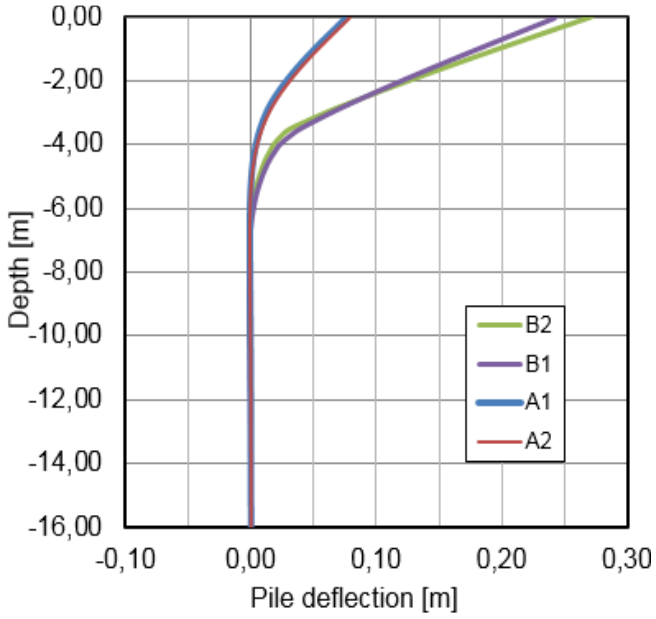

Figure 5.6.3. (a) Pile deflection results for all cases

By evaluating the results the following can be noted:

(a) In accordance to results from previous analyses, axial force seems to increase lateral capacity. This is observed for both full bond and gapping-sliding conditions.

(b) For all analyzed cases with detailed Concrete based model, the failure mechanism of the pile is the same, as shown in Figure 5.6.4 below, and again separation and sliding causes the generation of more plastic points distributed along the pile. Moreover it seems that for all cases large deformation leads to yielding of main reinforcement accompanying with flexural crack opening.

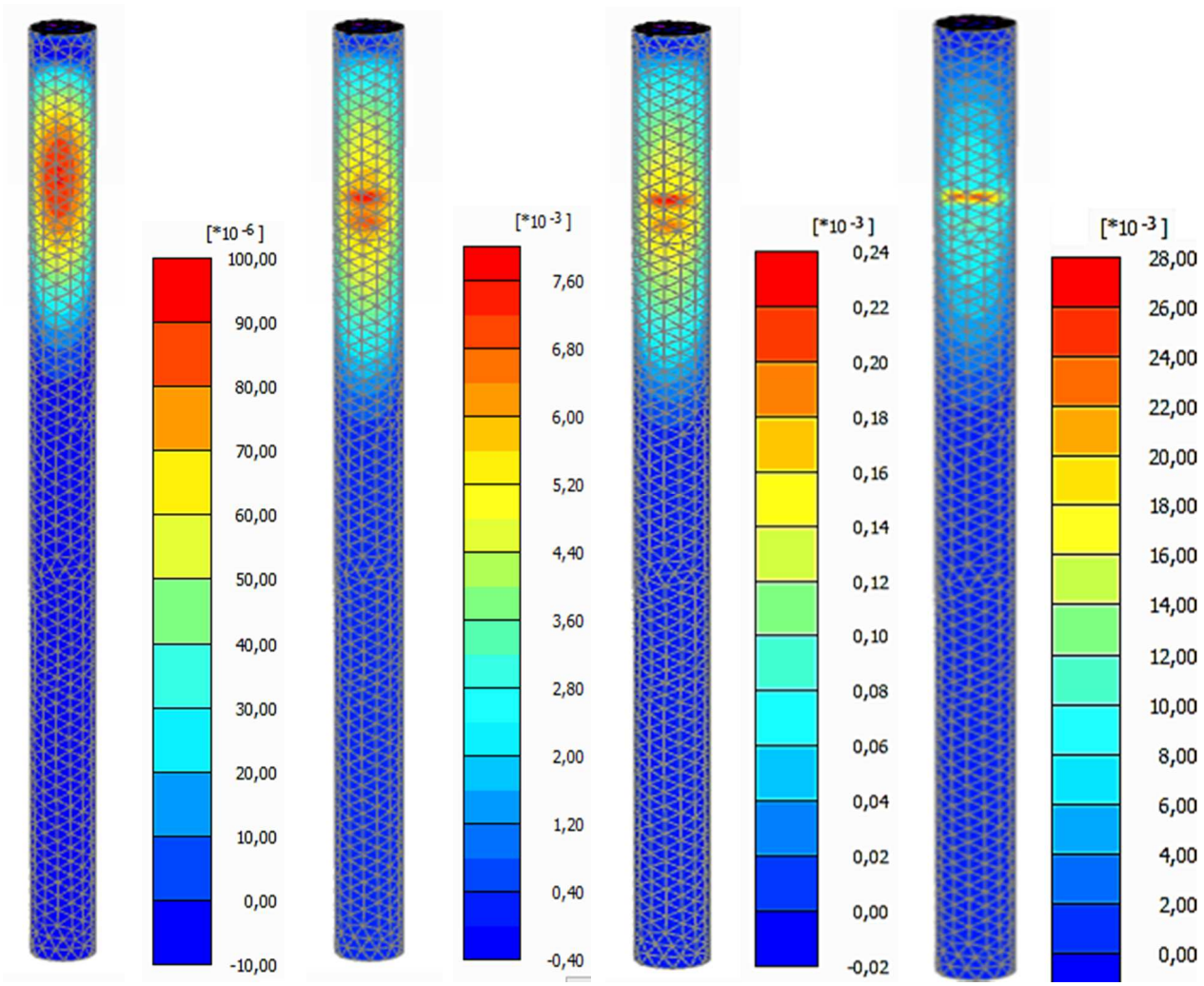

Figure 5.6.4. Evolution of failure mechanism in terms of incremental deviatoric strain Δγs

5.7 Results and Discussion

Results from analyses with the three proposed models are demonstrated in Figures 5.7.1, 5.7.2.

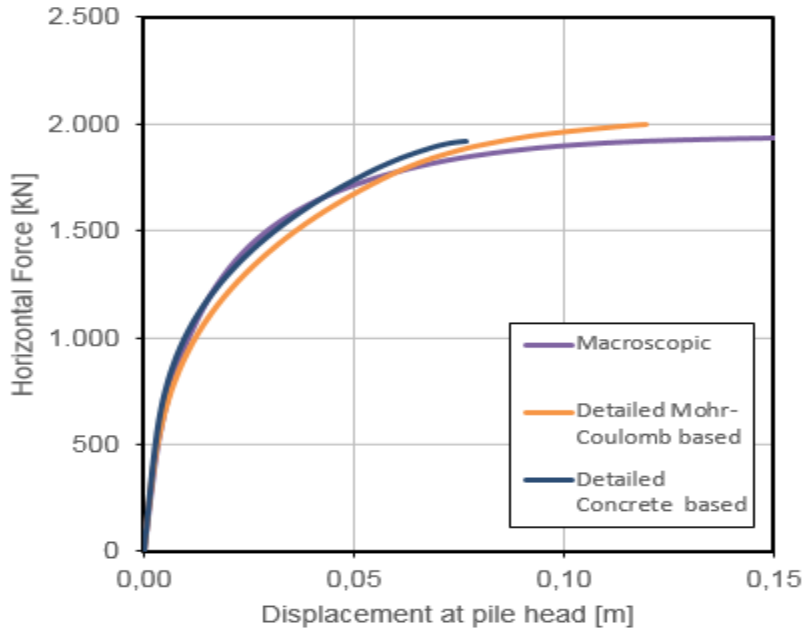

(a)

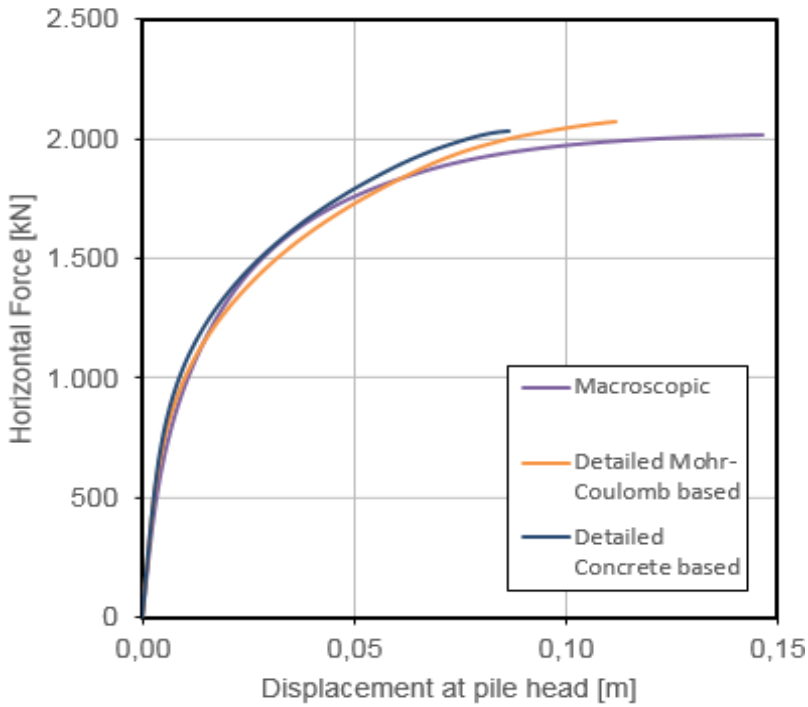

(b)

Figure 5.7.1. Comparison of computed head force displacement curves between the three proposed models, considering full bonding conditions (a) only lateral loading (b) combined axial and horizontal loading

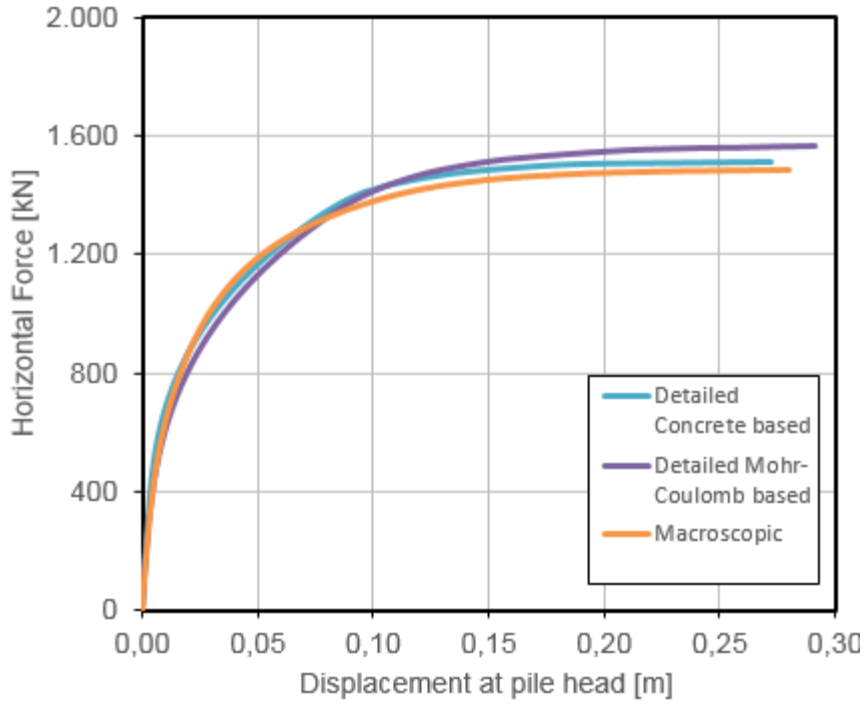

(a)

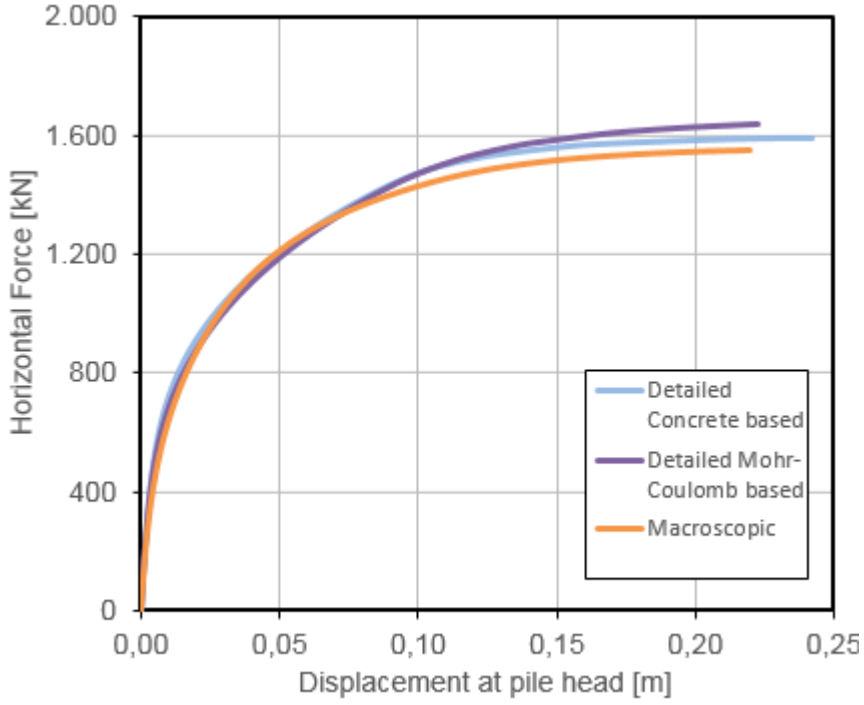

(b)

Figure 5.7.2. Comparison of computed head force displacement curves between the three proposed models, considering gapping effect (a) only lateral loading (b) combined axial and horizontal loading

By evaluating the results the following conclusions can be derived:

- The three proposed models used to simulate the nonlinear pile material present almost the same response for all examined cases and the results are in accord with Broms theory of ultimate pile lateral capacity. The implementation of Broms limit equilibrium theory assuming both constant and trapezoidal distribution of lateral soil resistance per depth, as proposed by Matlock (1970), validates the results of ultimate lateral capacities extracted from analyses. Only exception is case A2 (full bonding pile-soil conditions) for analysis with detailed Mohr-Coulomb based model, considering trapezoidal distribution of p_y. Therefore, the models seem to be capable of reproducing the response of reinforced concrete piles in pile-soil interaction problems considering double non linearity. For all examined cases Detailed Mohr-Coulomb based model gives increased ultimate lateral capacities, resulting though in insignificant deviations. Perhaps this is caused by the tension cut-off added to the pile material, in order to enable load advancement procedure. Deviations between the models are less than 5% in all cases. It has to be mentioned that deviations between Concrete based and Macroscopic models are less than 2.5%. The highest deviation is observed between responses from Macroscopic and Detailed considering gapping, however, still less than 5%. Lateral ultimate capacities derived from analyses are presented in Table 5.4 below.

Table 5.4 Ultimate lateral capacities derived from analyses with the three proposed models

Case	**Ultimate Lateral Resistance [kN]**		
	Detailed Concrete based	Detailed Mohr-Coulomb based	Macroscopic
A1	1915	1993	1935
A2	2028	2070	2033
B1	1512	1565	1487
B2	1592	1638	1549

Assuming constant ultimate lateral soil resistance with depth, as shown in Figure 5.4.1, derived values of λ_1 coefficient for each model and each examined case are listed in Table 5.5, below. These values are obtained by replacing in Eq (5.4.2) ultimate lateral loads from numerical analyses and ultimate bending moments extracted from pushover analyses as

presented in Table 4.7. In all examined cases the condition $2 \leq \lambda_1 \leq 12$ is satisfied. For the second assumption of trapezoidal distribution with depth of ultimate lateral soil resistance, values of λ_2 obtained by implementing static equilibrium, are presented in Table 5.6. The resulting ultimate soil resistance for all cases except case A2 for detailed Mohr-Coulomb based model, satisfies the aforementioned criteria. ($p_y \leq 12 S_u$ D = 720 kN/m). Analysis of case A2 of detailed Mohr-Coulomb based model gives an increased p_y of approximately 40 kN

Table 5.5: λ_1 values for ultimate soil lateral resistance, considering constant distribution with depth

Case	$\boldsymbol{\lambda_1}$ ($P_y = \lambda_1 s_u d$)		
	Detailed Concrete based	Detailed Mohr-Coulomb based	Macroscopic
A1	11	10	10
A2	12	11	11
B1	7	6	6
B2	7	7	7

Table 5.6: λ_2 Values for ultimate lateral soil resistance, considering trapezoidal distribution with depth

Case	$\boldsymbol{\lambda_2}$ $p_y = \left(\lambda_2 + \frac{\sigma'_v}{s_u} + J\frac{z}{d}\right) s_u\, d$		
	Detailed Concrete based	Detailed Mohr-Coulomb based	Macroscopic
A1	10	10	10
A2	11	10	10
B1	6	6	6
B2	7	7	6

- Axial force contributes to the increase of lateral capacity. The contribution is similar considering both full bond and gapping-sliding between the pile and the surrounding soil. Moreover axial force causes the plastificication of the interface at the tip of the pile, as illustrated in Figure 5.7.4 below.

- For all examined cases plastic hinge formation and length is in accordance with results from Papakyriakopoulos (2013). Additionally, it seems that plastic hinge depth increases when gapping is taken into account, as it is clearly depicted in Figure 5.5.6. For Mohr-Coulomb based models the failure mechanism is exactly the same, whether for Concrete a developing cracking pattern leads to a discrete flexural crack at failure state. The depth of this discrete crack is the same with the plastic hinge formation for the other two models. The failure mechanisms for Concrete and Mohr-Coulomb based models are compared in Figure 5.7.3 below.

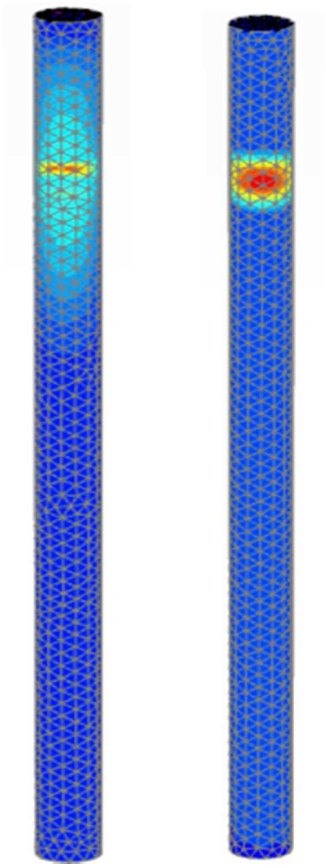

Figure 5.7.3 Comparison of the failure mechanism between Concrete and Mohr-Coulomb based models

- Gapping and sliding between the pile and the surrounding soil, and soil degradation have a significant impact on lateral capacity of piles. The stiffness of the pile is reduced and there is a loss of lateral capacity more than 400 kN, compared to full bonding cases. It seems that the loss of confinement from the soil due to the gap produced between the near-surface soil and the pile, leads to the reduction overall horizontal stiffness of the pile-soil system and larger deformations.

- For cases considering full bonding between the pile and the surrounding soil Concrete based model presents a more brittle failure at lower displacement rates, followed by Detailed Mohr-Coulomb based model, while for Macroscopic model a yield plateau can be visualized. For cases considering gapping and sliding all models present a more ductile behavior, as yield plateaus are observed before failure *

- In Figure 5.7.4 soil failure around the pile is illustrated. It is observed that in cases considering gapping effect soil plastification is extended beyond the proximal vicinity of the pile at shallow depths.

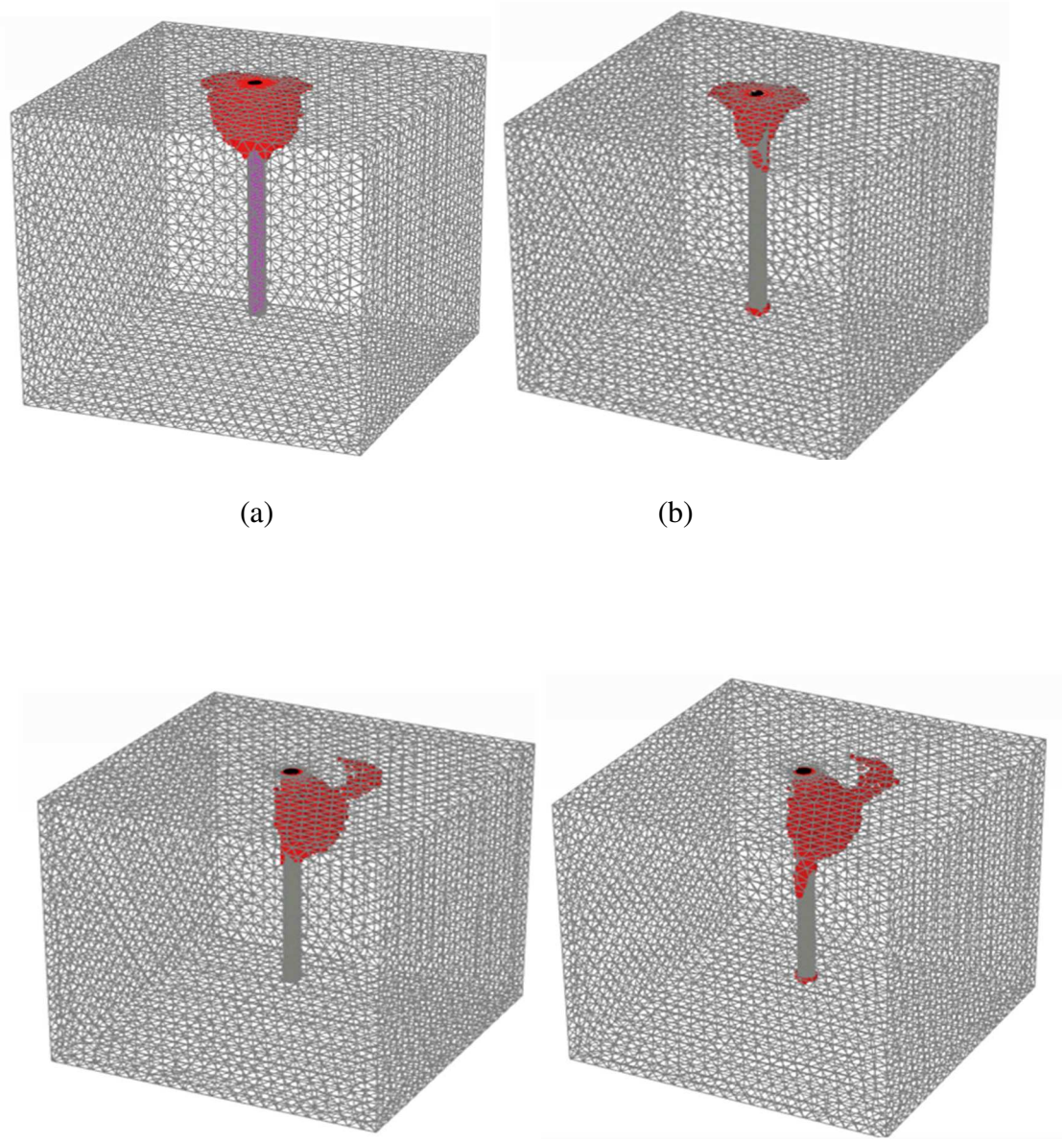

Figure 5.7.4. Plastic points distribution: (a) full bonding between pile and soil, (b) full bonding between pile and soil with the addition of axial load, (c) separation between the pile ad the soil, (d) separation between the pile and the soil with the addition of axial load

6 Conclusions and recommendations

Conclusions

In this thesis, three phenomenological constitutive models are presented, capable to describe the nonlinear behavior of reinforced concrete elements. First, key parameters are calibrated and then the proposed models are implemented in the pushover analysis of a reinforced concrete column. Their response is verified by cross validation, as well as by comparing their performance with computer codes used for the sectional and full-member analysis of reinforced concrete members. The comparison is made basically in terms of force-displacement and moment-curvature responses and satisfactory convergence is succeeded between the three proposed, as well as reference models. Subsequently, the suggested phenomenological models are implemented in a soil-structure interaction application and their capability to reproduce the behavior of reinforced concrete piles is evaluated. The results of the three proposed models extracted through FE analyses are in accordance with Broms (1964) limit equilibrium theory of ultimate pile lateral capacity.

The important conclusions drawn for each proposed model are presented below:

- Detailed Concrete based model, combined with elastoplastic 3D beam elements succeeds to capture the actual behavior of reinforced concrete elements. This is achieved due to its advanced stress-strain formulation that can describe strain hardening and softening of the concrete material. With Concrete model the exact failure modes and crack pattern of the members can be observed. This fact could be extremely useful for the investigation of failure mechanisms and the correct design of reinforced concrete structures utilizing Finite Element codes, avoiding catastrophic brittle failure types. Concrete material model, due to its aforementioned complex formulation requires the input of 25 parameters that are reduced to 14 when only strain hardening and softening are considered, ignoring time dependency, as in the present thesis. Most of these parameters can be derived from standard uniaxial tensile and compression tests. However parameters related to fracture energy are sensitive to mesh coarseness and require special handling to avoid unrealistic results. For each problem under investigation these parameters should be carefully calibrated.

- Detailed Mohr-Coulomb based model manages to satisfactory approach the nonlinear response of reinforced concrete elements. It is a combination of a simple linear elastic-perfectly plastic stress-strain relation for concrete material and elastoplastic 3D beam elements used as reinforcement. Although strain hardening and softening behavior are not incorporated and therefore crack pattern cannot be visualized, the model provides a good representation of ultimate capacity of the member. Therefore, it can provide accurate results and be used as a first order approximation. Additionally Mohr-Coulomb model for concrete material requires only 5 input parameters that are effortless derived from compressive and tensile strength of structural concrete. As a result it can be adopted by any user without the need of deep knowledge of concrete theory. Lastly this model can be implemented in any case and by any user, as Mohr Coulomb material model exists in all Finite Element Software packages.

- Macroscopic model, as proposed by Gerolymos and Papakyriakopoulos (2014) succeeds to simulate the behavior of circular reinforced concrete elements uniformly combining ease of use and accuracy. The small number of parameters and short computational time required render the model easily implementable and flexible in effectively describe the overall behavior of a reinforced concrete element. This model is developed utilizing simple well known failure criteria, namely Mohr-Coulomb and Tresca. The calibration of the model can easily be conducted as described by Papakyriakopoulos (2013) by the following steps:

  (a) Extraction of the failure envelope of the studied circular reinforced concrete section

  (b) Using the derived mathematical expressions and an optimization tool to calibrate the parameters of the model

  (c) Insertion of the calibrated parameters in the FE model and extraction of either the failure envelope ,or as in our case force-displacement response

  (d) Verification by comparing the extracted through FEM results with those of the reference models

  Due to its simplicity and remarkably small computational time required, Macroscopic model can be used as a first order prediction of the behavior of

reinforced concrete members when results need to be extracted rapidly. Lastly it can be implemented in all Finite Element codes without the need of exact and mathematically complex constitutive material models for concrete behavior.

Recommendations for future research

In this section some suggestions for future work are provided, considering the implementation of the three proposed constitutive models.

- In the present thesis the influence of confinement of concrete material was not studied, as only longitudinal detailed reinforcement was modeled. However in almost all cases transverse reinforcement is necessary to confine the concrete core and increase strength and ductility of the member. Plaxis Concrete model quantifies the increased ductility with confining pressure with parameter a. Due to limited time available, for Detailed Mohr-Coulomb based approach only longitudinal reinforcement was modeled, with the use of 3D elastoplastic beam elements. Therefore in order to have a common basis of comparison, parameter a of Concrete model was set equal to 0. In future research, the detailed modeling of transverse reinforcement in Plaxis 3D FE code is proposed, for approaching the actual behavior of structural reinforced concrete members.
- A possible improvement for a more realistic modeling of reinforcement can be succeeded by using elements able to take into account bonding between reinforcement bars and concrete. On account of this, the performance of 3D embedded beam elements should be investigated in more detail.
- Lastly, the use of the proposed constitutive models could be extended in dynamic problems. In this thesis only monotonic loading was considered. Moreover in most soil-structure interaction applications pile material is considered to be linear elastic. However, dynamic pile-soil interaction involves complicated material nonlinearities and the response of the piles up to failure is essential to be predicted. As a result the implementation of these phenomenological models to the pile material could be very useful to capture strength and stiffness reduction due to cycling loading.

7 References

Agioutantis, Z. (2002). Principles of Soil Mechanics. ION, Athens

Ardiaca, D. H. (2009). Mohr-Coulomb parameters for modelling of concrete structures. *Plaxis Bulletin*, *Spring*, 12–15.

ASCE Task Committee on Finite Element Analysis of Reinforced Concrete Structures. (1982). State-of-the-Art Report on Finite Element Analysis of Reinforced Concrete, ASCE Special Publications.

Attard M, Setunge S. (1996).Stress-strain relationship of confined and unconfined concrete. *ACI Mater. J*. 93(5), p.p 432-442

Barros, J. A. O., & Figueiras, J. A. (1999). Flexural behavior of SFRC: Testing and modeling. *Journal of Materials in Civil Engineering*, *11*(4), 331–339.

Bazant, Z. (1992). Fracture mechanics of concrete. Part I: State-of-Art Report. In *ASCE J Struct Div* (Vol. 140).

Bazant, Z. & Planas, J. (1998), Fracture and size effect in concrete and other quasibrittle materials, CRC Press.

Bentz, E.C. ; Collins, M. P. (2011). *Response-2000.*

Bentz, E. C. (2000). Appendix A : Program Manuals Sectional Analysis of Reinforced Concrete Members. 1–86.

Brinkgreve, R. B. (2011). Scientific Manual. *Plaxis*.

Broms, B. (1965). Design of laterally loaded piles. *Journal of Soil Mechanics and Foundation Division*, *91(3)*, 77–99.

Candappa, D., Sanjayan, J., & Setunge, S. (2001). Complete Triaxial Stress-Strain Curves of High-Strength Concrete. *Journal of Materials in Civil Engineering*, 13(3), 209-215.

Chen, W. F., & Han, D. J. (1982) Plasticity in Reinforced Concrete. J.Ross Pub.

Chen, W. F., & Han, D. J. (1988). Plasticity for Structural Engineers. In *Plasticity for Structural Engineers*. J.Ross Pub.

Cornelissen, H. A. W., Hordijk, D. A., & Reinhardt, H. W. (1962). Two-Dimensional Theories of Anchorage Zone Stresses in Post-Tensioned Prestressed Beams. *ACI Journal Proceedings*, *59*(10)

Committee, A. C. I. (2019). 318-19 Building Code Requirements for Structural Concrete and Commentary. In *318-19 Building Code Requirements for Structural Concrete and Commentary*.

Desai, C. S. (1979). Elementary Finite Element Method. Prentice-Hall.

EN 1992-1-1. (2004). Eurocode 2: Design of concrete structures. European Committee for Standardization.

Esmaeily A. 2001. USC-RC. Software for analyzing behavior of a single reinforced concrete member. Version 1.0.2, USC Civil Engineering Department.

Filippou, F. C. (2015). Mechanics and Materials Finite Element Analysis of Reinforced Concrete Structures. *January 1990*.

Gerolymos, N., Gazetas G., (2005). "Phenomenological Model Applied to Inelastic Response of Soil-Pile Interaction Systems", Soils & Foundations, Japanese Geotechnical Society, Vol. 45(4), p.p. 119-132

Gerolymos, N., (2012), "A macro-element model for nonlinear static and dynamic response of piles", research program final report, PEVE 2008

Gerolymos, N., Papakyriakopoulos, O., & Brinkgreve, R. B. J. (2014). Macroelement modeling of piles in cohesive soil subjected to combined lateral and axial loading. *Numerical Methods in Geotechnical Engineering - Proceedings of the 8th European Conference on Numerical Methods in Geotechnical Engineering, NUMGE 2014*, *1*(June 2019), p.p 373–378.

Hazzar, L., Hussien, M. N., & Karray, M. (2017). Influence of vertical loads on lateral response of pile foundations in sands and clays. *Journal of Rock Mechanics and Geotechnical Engineering*, *9*(2), p.p 291–304.

Hibbit, K., Karlsson, B., & Sorensen, P. (2014). ABAQUS Theory manual. Providence : Dassault Systèmes.

Hillerborg, A. (1985). The theoretical basis of a method to determine the fracture energy GF of concrete. *Materials and Structures*, *18*(4), p.p 291–296.

Hognestad, E. (1951). A Study of Combined Bending and Axial Load in Reinforced Concrete Members. *Bulletin Series No. 399.*

Kim, J. J., & Reda Taha, M. (2014). Experimental and numerical evaluation of direct tension test for cylindrical concrete specimens. *Advances in Civil Engineering*

Kotsovos, M. D., and Newman, J. B., 1977. "Behavior of concrete under multiaxial stress". ACI, 74(9), 443-444.

Maatkamp, T. W. P. (2016). The capabilities of the Plaxis Shotcrete material model for designing laterally loaded reinforced concrete structures in the subsurface

Maekawa, K., & An, X. (2000). Shear failure and ductility of RC columns after yielding of main reinforcement. *Engineering Fracture Mechanics*, *65*(2–3), p.p 335–368.

Matlock, H. (1970). Correlations for Design of Laterally Loaded Piles in Soft Clay. Proceedings of the 2nd Offshore Technology Conference, Houston, 22-24 April 1970, p.p 577-594

Nakamura, H., & Higai, T. (2001). Compressive fracture energy and fracture zone length of concrete. *Modeling of Inelastic Behavior of RC Structures under Seismic Loads*, *January 2001*, p.p471–487.

Papakyriakopoulos, O. (2013). Macroelement modeling of the nonlinear response of piles and pile groups subjected to combined lateral and axial loading

POPOVICS S. (1970). Review of Stress-Strain Relationships for Concrete. *ACI Journa*l,

67(3), p.p 243–248

Plaxis 3D. (2018). PLAXIS Material Models.

Plaxis 3D. (2018). PLAXIS Reference.

Randolph, M. F. (1981): The response of flexible piles to lateral loading, Geotechnique, 31(2), p.p 247-259

Reese, L.C., Van Impe W.F., 2001, Single Piles and Pile Groups under Lateral Loading, A.A.Balkema. Rotterdam

Schädlich, B., & Schweiger, H. F. (2014). A new constitutive model for shotcrete. *Numerical Methods in Geotechnical Engineering - Proceedings of the 8th European Conference on Numerical Methods in Geotechnical Engineering, NUMGE 2014*, *1*(2), p.p 103–108.

Schädlich, B., Schweiger, H. F., Marcher, T., & Saurer, E. (2014a). Application of a novel constitutive shotcrete model to tunnelling. *Rock Engineering and Rock Mechanics: Structures in and on Rock Masses - Proceedings of EUROCK 2014, ISRM European Regional Symposium*, *May*, 799–804.

Schütz, R., Potts, D. M., & Zdravkovic, L. (2011). Advanced constitutive modelling of shotcrete: Model formulation and calibration. *Computers and Geotechnics*, *38*(6), p.p 834–845.

Rohleder, S. (2017). Perforfmance analysis software for reinforced concrete beam columns under various load and displacement patterns. Kansas State Univeristy

Smith I.M., Griffith D.V. 1982. Programming the Finite Element Method, Second Edition. John Wiley & Sons, Chisester, U.K.

Sung, Y. C., Liu, K. Y., Su, C. K., Tsai, I. C., & Chang, K. C. (2005). A study on pushover analyses of reinforced concrete columns. *Structural Engineering and Mechanics*, *21*(1), p.p 35–52.

Ter-Martirosyan, A., Sidorov, V., & Ermoshina, L. (2018). Features of optimization of model parameters for solving geotechnical problems. *MATEC Web of Conferences*, *251*.

Tomlinson, M. J. (1994). *Pile Design and Construction Practice* (4th ed.). Taylor & Francis.

V.Chaudhari, S., & A. Chakrabarti, M. (2012). Modeling of Concrete for Nonlinear Analysis using Finite Element Code ABAQUS. *International Journal of Computer Applications*, *44*(7), p.p 14–18.

Van Mier, J. (1998). Failure of concrete under uniaxial compression: An overview. In H. Mihashi, & K. Rokugo, Fracture Mechanics of Concrete Structures: Proceedings FraMCoS-3, pp. 1169-1182.

Van Mier, J., Shah, S. P., Arnaud, M., Balayssac, J., Bascoul, A., Choi, S., Dasenbrock, D., Ferrara, G., French, C., Gobbi, M., Karihaloo, B., König, G., Labuz, J., Lange-Kornbak, D., Markeset, G., Pavlovic, M., Simsch, G., Thienel, K., Turatsinze, A., … Zissopoulos, D. (1997). RILEM TC 148-SSC: TEST METHODS FOR THE STRAIN-SOFTENING RESPONSE OF CONCRETE Strain-softening of concrete in uniaxial compression. *Materials and Structures/Materiaux et Constructions*, *30*(30), 195–209.

Valalas, D. (1981). Soil Mechanics

Watanabe, K., Niwa, J., Yokota, H., & Iwanami, M. (2004). Experimental study on stress-strain curve of concrete considering localized failure in compression. *Journal of Advanced Concrete Technology*, *2*(3), p.p 395–407.

Willam, K. J. (2003). Constitutive Models for Engineering Materials. *Encyclopedia of Physical Science and Technology*, 603–633

Xu, S., Reinhardt, H.W. Determination of double-K criterion for crack propagation in quasi-brittle fracture, Part III: Compact tension specimens and wedge splitting specimens. *International Journal of Fracture* 98, p.p 179–193 (1999).

Zhao, X., Wu, Y. F., Leung, A. Y., & Lam, H. F. (2011). Plastic hinge length in reinforced concrete flexural members. *Procedia Engineering*, *14*, p.p 1266–1274.